AVIATAR - AN AUGMENTED REALITY SYSTEM TO IMPROVE PILOT PERFORMANCE FOR UNMANNED AERIAL SYSTEMS

by

Robert Louis Abbott

A dissertation submitted to the faculty of
The University of North Carolina at Charlotte
in partial fulfillment of the requirements
for the degree of Doctor of Philosophy in
Computing and Information Systems

Charlotte

2021

Approved by:

_____
Dr. Mirsad Hadzikadic

_____
Dr. Minwoo Lee

_____
Dr. Zbigniew Ras

_____
Dr. Samira Shaikh

ABSTRACT

ROBERT LOUIS ABBOTT. Aviatar - an augmented reality system to improve pilot performance for unmanned aerial systems. (Under the direction of DR. MIRSAD HADZIKADIC)

In the modern airspace, small unmanned aircraft systems (sUAS) such as drones are becoming increasingly popular with both amateur enthusiasts as well as professional pilots. In the three years following the initiation of the small drone registration rule in 2015, over one million drones were registered in the U.S. alone. By 2022, the United States Federal Aviation Administration (FAA) estimates that the number of registrations could exceed 3.8 million UAS [1]. In recognition of the necessity to integrate sUAS traffic into the national airspace system, Congress passed the FAA Modernization and Reform Act of 2012, which created the mandate for the FAA to regulate sUAS operation in United States national airspace (NAS) [2]. This also created a number of obligations for drone pilots, including avoidance of restricted airspace, maximum flight levels, safe separation from aircraft - including other UAS - as well as avoiding flight over civilian human population and contact with personal property such as buildings or cars. These new obligations associated with safety coupled with the goals of recreational or commercial flight act to degrade pilot situational awareness.

Because of the nature of flying a drone either for pleasure or commercial purpose, it is very easy for operators to lose their situational awareness (SA) of the environment around them. A study published by the NASA Langley Research Center (LaRC) in 2017 found that the majority of commercial aviation accidents not attributable to aircraft systems failure involved the crew's loss of SA of the aircraft or the environment, and that crew distraction from operation was associated with all of these accidents [3]. If this is the case with commercial aircraft pilots inside of an enclosed aircraft cockpit in relative isolation, it is easy to imagine that the potential for distraction

in the UAS environment is at least great. This demonstrates the potential for a decreased SA state to create an unsafe environment for other pilots and bystanders and lead to fines and penalties for the drone pilot if damage, injury, or disruption to the airspace occurs. While many times a pilot or flight crew can be distracted by agents not directly associated with the operation of an aircraft, there are many flight phenomena that can require a pilot's focus to manage. This focused attention can also degrade a pilot's SA.

One mode of pathological flight phenomena in fixed-wing aircraft is that of pilot-induced oscillation (PIO). These PIO can occur either as a result of pilot-airframe coupling as in the case of *biodynamic feedthrough* (BDFT) [4], or as a result of the lag between pilot observation and action and the propagation of the pilot's actions and the control response of the aircraft under the influence of structural or environmental stimulus on the aircraft system [5]. Under either scenario, the actions necessary to identify and resolve of these PIO can quickly distract the pilot and cause a degradation of pilot SA level. This pilot distraction can lead to *mission task element* (MTE) failure, loss of aircraft control, and damage or destruction of the aircraft and surrounding persons and property [6].

In this study, we make an effort to identify the state of the art in pilot situational awareness research and to understand the critical pilot-aircraft interactions that are at the forefront of research in this field. Pilot induced oscillations, especially of the Type III nonlinear family, are one such topic that researchers have worked on heavily for over 40 years and have made minimal progress in solving. In fact, the addition of autonomous control functions to modern avionics systems, such as control surface rate limiting features, have increased the severity associated with these Type III PIO when they occur. To broaden the context of our work, similar issues are faced in a variety of other vehicle control situations including ships, cars, farm equipment, and large trucks [7, 8, 9, 10, 11].

To support our goal of improving the experience, productivity, and safety of remote UAS pilots, we implemented a see-through augmented reality headset system, AviatAR, to provide information to the pilot with minimal detrimental effects. We also created a method, the Flight-Space Volume Model (FSVM), to enable accurate placement of an augmented reality cue that we refer to as a Gizmo in the pilot's visual field. This cue serves to aid in pilot accuracy and notification of predicted pilot-induced oscillations to enable a pilot to actively react this phenomena in the early stages of formation.

During our research, one issue that we noticed was a dearth of research on pilot SA and PIO phenomena associated with multirotor UAS systems. Because of the increase in the number of UAS systems available for both personal and commercial use, we felt that there were many contributions that could be made to this several fields of study. Thus, our research is a multidisciplinary work that supports three fields of research: computer science, cognitive science, and aeronautics.

In our experiments, we evaluated the performance of a pilot flying a low-autonomy unaugmented quadcopter in an outdoor, uncontrolled setting for both an unaided pilot as well as one equipped with three different evolutions of the AviatAR head-mounted display. In each of these evolutions, we included both the Gizmo component alone as well as two variations of the PIO cue, both in the superior and inferior peripheral visual fields and evaluated pilot performance in terms of positional accuracy. Our analysis demonstrates that a pilot equipped with the AviatAR display outperformed the unaided pilot, and that the addition of the PIO cue further enhanced pilot performance with respect to accuracy. Further, we demonstrated that placing a persistent low-complexity informational cue in the inferior peripheral visual field of the pilot significantly improved pilot accuracy over the superior field cue, which leads to future work to better understand how low-complexity inferior peripheral field cues can be used to enhance the performance and improve situational awareness of

equipment operators in a broad range of applications.

DEDICATION

Pursuing (and achieving!) a doctoral degree later in life is a hard thing, especially while fully-employed outside of academic life. Every moment of time is precious, and you miss out on a lot of things that matter during the research and writing process. One cannot achieve a milestone such as this without the love and support of some very special people in your life.

First, I want to dedicate this work to my wife, Sherri, for her support throughout my lifelong educational pursuits, and especially over the last six years of this process. With all of the life events in our families during this time, I would not have been able to accomplish this goal without her love, encouragement, and willingness to give me the time to devote to this endeavor.

Secondly, I want to devote this work to the memory of my parents, both of whom I lost in 2019. When I started this journey, I had a vision of them watching one day as I walked across a stage to receive my terminal degree in this field of study to which I have devoted a good portion of my life. Unfortunately, that didn't work out quite the way it was planned, and I acknowledge that I missed out on spending time with them in this pursuit. Our education was always important to them, since they did not have the opportunity to pursue it. Accomplishing this goal while missing out on time with them makes this a bittersweet occasion.

Finally, I want to thank my fellow members of the UNC Charlotte Complex Systems Institute: Malak Abdullah, Gizem Bacaksizlar, Elizabeth von Briesen, Louai Mohammed, Riyi Qui, and Maryam Tavakoli. They were my university family throughout this journey and I certainly would not have ever completed this achievement without their camaraderie throughout this journey. I wish you all the best in your careers and future lives.

ACKNOWLEDGEMENTS

I want to thank my research advisor, Mirsad Hadzikadic, for all of his support and direction throughout my doctoral pursuit. Without his encouragement to apply to the graduate program at UNC Charlotte and his support of my nonlinear approach throughout this program, it is most likely that I would have never started this journey and definitely would have never completed it.

I also want to thank my research committee: Minwoo Lee, Zbigniew Ras, and Samira Shaikh. Your support, advice, and encouragement throughout this journey have been invaluable to my success. Only at the end of this have I fully appreciated the true meaning of the advice that you have given me over the years. I hope that I am one day able to help students with the things that you have all taught me over this journey.

TABLE OF CONTENTS

LIST OF TABLES

LIST OF FIGURES

LIST OF ABBREVIATIONS

$e(t)$	error function w.r.t. time
AR	augmented reality; the use of computer-generated percepts projected into an actual reality to augment and improve the perceptibility of the current situation
CE	controlled element
deg	degree (unit of measure)
DF	describing function
DOF	degrees of freedom
FC	flight controller
FOV	field of vision
HC	human controller
HMD	head-mounted display
IMU	inertial measurement unit
kt	knot, a nautical or aeronautical unit of speed; 1 nautical mile per hour = 1.852 km/h or 1.15078 mph
LaRC	NASA Langley Research Center
MTE	mission task element
NASA	US National Aeronautics and Space Administration
NMS	neuromuscular system

nm	nautical mile, a unit of measure equal to 1.15 statute miles or 1852 m.
OODA	observe-orient-decide-act loop
PID	proportional-integral-derivative; a type of feedback-control algorithm
PIO	pilot-induced oscillation
quadcopter	a type of multirotor aircraft with four rotary wings; also referred to as a *quadrotor* aircraft
SA	situational awareness
sUAS	small UAS; a UAS >0.55 pounds but ≤50 pounds fully-equipped
UAS	unmanned aircraft system
UAV	unmanned or uncrewed aerial vehicle
VR	an artificial representation of an environment and with real and generated percepts projected into it for presentation to a human viewer

CHAPTER 1: INTRODUCTION

In the modern airspace, small unmanned aircraft systems (sUAS) such as drones are becoming increasingly popular with both amateur enthusiasts as well as professional pilots. In the three years following the initiation of the small drone registration rule in 2015, over one million drones were registered in the U.S. alone. By 2022, the United States Federal Aviation Administration (FAA) estimates that the number of registrations could exceed 3.8 million UAS [1]. In recognition of the necessity to integrate sUAS traffic into the national airspace system, Congress passed the FAA Modernization and Reform Act of 2012, which created the mandate for the FAA to regulate sUAS operation in United States national airspace (NAS) [2]. This also created a number of obligations for drone pilots, including avoidance of restricted airspace, maximum flight levels, safe separation from aircraft - including other UAS - as well as avoiding flight over civilian human population and contact with personal property such as buildings or cars. These new obligations associated with safety coupled with the goals of recreational or commercial flight act to degrade pilot situational awareness.

Because of the nature of flying a drone either for pleasure or commercial purpose, it is very easy for operators to lose their situational awareness (SA) of the environment around them. A study published by the NASA Langley Research Center (LaRC) in 2017 found that the majority of commercial aviation accidents not attributable to aircraft systems failure involved the crew's loss of SA of the aircraft or the environment, and that crew distraction from operation was associated with all of these accidents [3]. If this is the case with commercial aircraft pilots inside of an enclosed aircraft cockpit in relative isolation, it is easy to imagine that the potential for distraction

in the UAS environment is at least great. This demonstrates the potential for a decreased SA state to create an unsafe environment for other pilots and bystanders and lead to fines and penalties for the drone pilot if damage, injury, or disruption to the airspace occurs. While many times a pilot or flight crew can be distracted by agents not directly associated with the operation of an aircraft, there are many flight phenomena that can require a pilot's focus to manage. This focused attention can also degrade a pilot's SA.

One mode of pathological flight phenomena in fixed-wing aircraft is that of pilot-induced oscillation (PIO). Ever since Orville and Wilbur Wright took their first flights in the Wright Flyer over the dunes of Kitty Hawk, North Carolina in 1903, the phenomena of pilot-aircraft coupling that produces undesirable oscillations have been identified during flight operations [14]. The label attached to this phenomena is *pilot-induced oscillations* (PIO). These PIO can occur either as a result of pilot-airframe coupling as in the case of *biodynamic feedthrough* (BDFT) [4], or as a result of the lag between pilot observation and action and the propagation of the pilot's actions and the control response of the aircraft under the influence of structural or environmental stimulus on the aircraft system [5]. Under either scenario, the actions necessary to identify and resolve of these PIO can quickly distract the pilot and cause a degradation of pilot SA level. This pilot distraction can lead to *mission task element* (MTE) failure, loss of aircraft control, and damage or destruction of the aircraft and surrounding persons and property [6].

The PIO phenomena has also been identified in rotorcraft, particularly in helicopters [15, 16, 17, 18]. In our literature review, we have found very little mention of PIO as related to multirotor UAS, although there are specific mentions of vehicle oscillations during MTE executions in the NASA document *Defining Handling Qualities of Unmanned Aerial Systems: Phase II Final Report* [13]. Because of this lack of documented understanding of how PIO relate to the flight dynamics of multirotor

UAS, we first include a brief analysis of winged vs. multirotor aircraft flight dynamics in our research to motivate our discussion.

1.1 Background

As aircraft have increased in capability, performance, and complexity, pilots have been required to perform increasingly difficult physical and mental operations to fly their aircraft. When this additional complexity of operation is coupled with complex or difficult mission tasking, it is not surprising that every component and control must be designed to maximize a pilot's capabilities while also requiring a minimal share of their cognitive and and physical budgets [19]. When this is extended to the teleoperation, or remote control from a distance, of an UAS, the increase in pilot focus and requirements for a high degree of pilot SA is even greater [20].

While operating a UAS, a pilot has a broad range of responsibilities across which to allocate their attention. Many of these responsibilities have been codified into law. The United States Code of Federal Regulations (CFR) is a document that codifies the rules and regulations associated with laws of the United States of America. Title 14 of the CFR (14 CFR), covers the regulations associated with aeronautics and space. 14 CFR Chapter I addresses the mandate of the Federal Aviation Administration and the rules and regulations associated with all aircraft flight operations within the U.S. Two sections of 14 CFR specifically address the operation of UAS: 14 CFR Part 91 addresses the operating and flight rules of all aircraft operating in the US NAS, and 14 CFR Part 107 addresses the additional constraints on small UAS operating within the US NAS. Furthermore, 14 CFR §91.113 states that pilots are required to exercise proper right-of-way rules and to abide by the "see and avoid" doctrine to ensure that they do not interfere with the flight of other aeronautical traffic. The remote pilot-in-command (RPIC) or operator of a UAS is also bound by these same regulations. The complexities of flying a UAS from a third-person perspective, however, is more challenging than the first-person perspective enjoyed by the pilot of a manned aircraft

system. In addition, many commercial UAS missions flown under 14 CFR Part 107 include multiple mission objectives such as photography, video, surveying, or performance of other operator-intensive activities. In some cases, an additional UAS flight crew member is utilized to perform the details of the primary mission while the RPIC controls the aircraft; however, the coordination between the pilot and crew can serve as a distracting element to the safe operation of the UAS in conflict with the above mandates.

In addition to the flight control of the UAS, the pilot is usually tasked with performing some type of mission objectives, such as taking pictures or video of a specified target or area, surveying power lines for damage, or directing a rescue operation from an overhead perspective. These activities alone are usually enough to consume or saturate the pilot's capacity during a mission, but they are not the only activities that the pilot must perform. In addition, the pilot must ensure that the UAS does not fly overhead of any civilian (i.e., non-participant) personnel, as this is forbidden during normal operation under 14 CFR Part 107. Also, the pilot must remain vigilant of any aircraft traffic or structures in the area, including other UAS traffic, and avoid any close contact with or generate adverse affects on close aircraft. In a close, crowded venue, such as a construction site or a concert amphitheater, it is possible that multiple UAS are operating on multiple missions concurrently along with other obstacles such as cranes, concrete pumps, and other equipment that create a dynamically-changing aerial hazard. In such an environment, crewed aircraft traffic could be warned away from the area as a whole to prevent hazardous interactions with high-altitude equipment. However, since the primary mission of these UAS are the business of the venue, the pilots and operators must maintain situational awareness of the activities of the entire site during the mission. Lacking the sophisticated radars and collision avoidance systems of much larger aircraft, UAS pilots and operators have a much more difficult time maintaining a high level of situational awareness in

this environment.

During a UAS mission, a pilot has multiple opportunities for flight phenomena such as PIO to degrade their SA to unsafe levels. The first is when the pilot becomes task-locked and pays less attention to the flight condition of the aircraft. Under this condition, a PIO may begin to develop while the pilot is focused on a mission task element and doesn't recognize that a PIO has developed until it is too late to recover; at this point, the recovery attempts further degrade the pilot SA so that even a safe scuttling of the aircraft is not possible. Alternatively, the pilot may recognize that a PIO is developing and become task-locked on controlling the PIO in such a way that the mission task element is not sacrificed. Under this condition, the pilot's attempts to accomplish both the continuation of the mission task element while recovering from a PIO cause the pilot to lose SA to the point where some other incident (e.g., a crash into a nearby obstacle that the pilot didn't identify) results in mission failure.

1.2 Problem Statement

In the case of UAS, some PIOs can be induced into the flight as a result of a lack of direct tactile feedback and neurosensory coupling between the remote pilot and the aircraft [21, 18, 22]. Some of these effects can be mitigated with the addition of haptics in the control actuators [23, 24, 25] or through the use of first-person view (FPV) monitor goggles [26, 27]. Also, increased distance between the remote pilot and the UAS reduces the ability for the remote pilot to judge the effects of fine control inputs on UAS attitude [20]. This can lead to the development of PIOs as the remote pilot attempts to control the UAS from a distance.

Long-range, beyond line-of-sight (LOS) missions rely upon autonomous flight control system to guide the UAS using global navigational satellite systems (GNSS) (e.g., United States' GPS, Russia's GLONASS, China's BeiDou-3, etc.), or more complex navigational methods such as inertial guidance, celestial navigation, or terrain-matching in communications-denied environments [28, 29]. The autonomous methods

involved in these missions provide for no direct human pilot intervention over vehicle control and do not work well for applications such as wind bridge inspection or communications tower inspection. These operations rely upon primarily human remote pilot operations with some computer augmented systems control where the UAS must be guided from a distance by a human pilot while focusing on specific tasks identified during the mission [27].

In the case of complex missions, a team is sometimes required to perform the various tasks of the mission. These teams may consist of a remote pilot, observers, and equipment operators. In this situation, the integrated communications of all team members is critical to success. In many cases, such critical missions are prohibitively expensive or are impractical to execute. Also, the effort to communicate critical information across a large team may degrade SA by a level greater than the benefit provided by increased information flow. To this end, research has been done to determine how to reduce team size to a single pilot without overwhelming their capabilities [30, 31, 32].

To better enable an individual UAS operator tasked as both pilot and mission operator, we sought to develop a head-mounted display (HMD) equipped with see-through augmented reality (AR) capabilities. The objective of this HMD is to provide information to the pilot using low-complexity visual cues with sufficient information capacity to help improve mission performance and maintain pilot SA while minimally increasing or even decreasing pilot cognitive processing workload. We refer to this system as AviatAR.

1.3 Research Areas

To guide our research, we developed a set of research questions derived from our literature review as well as from our experience in outdoor UAS flight. These questions are centered around two research areas.

1.3.1 Area 1: Performance Comparison of Unassisted vs Augmented Control on Task Performance

Is it possible to improve pilot performance through integration of an augmented reality visor with a UAS flight control system to improve pilot capability level during mission execution?

Sub-questions:

- Can the use of an augmented reality visor user interface improve the accuracy of control for mission task elements?
- Can the effects of pilot-aircraft distance be countered through the use of an AR-enabled user interface?

1.3.2 Area 2: An Improved Augmented Reality User Interface

Can we use our understanding of the human visual system to construct an optimal user interface for remote pilots?

Sub-questions:

- How does the placement of visual cues in the inferior and superior visual field affect pilot performance?
- Does the placement of visual cues in the peripheral visual field improve pilot performance over placement of cues in other parts of the visual field?
- Does the cognitive budget consumed by processing images to interpret the attitude and motion of the UAS at a distance affect the ability for the pilot to perform mission task elements?

1.4 Key Findings

The key findings of this work are as follows:

- Performance of the pilot using the AviatAR augmented reality display with only the Gizmo component was significantly improved over baseline pilot performance.

- Performance of the pilot using the AviatAR augmented reality display with both the Gizmo and the PIO cue was significantly improved over the HMD with the Gizmo alone in terms of PIO mitigation as well as in terms of the performance metrics for each maneuver.

- Pilot performance showed significant improvement for placement of the PIO cue in the inferior peripheral visual field vs. placement in the superior visual field (collocated with the Gizmo).

1.5 Summary of Contributions

This dissertation is a multidisciplinary research endeavor and contributes to multiple fields.

1.5.1 Computer Science

Our research makes three principal contributions to the field of Computer Science.

- A method of a human-computer interface (HCI), *AviatAR*, that uses a see-through augmented reality headset to assist the pilot in UAS navigation through the display of a virtual construct known as a "Gizmo" in the pilot's field of vision. This Gizmo enhances the pilot's SA state by providing active visual cues for the UAS position and attitude in real-time.

- A method of creating a graphical model to represent the pilot-model airspace interaction that we refer to as the *flight-space volume model* (FSVM), which uses a multi-source information fusion (MSIF) [33, 34] approach to construct a representation of the UAS position relative to the pilot in 3D model space.

- A method to coordinate the display of a moving dynamic object in an augmented reality world using a method we call *at-distance gaze correction* (ADGC). This method takes into account both the kinematics of the object as well as the gaze information of the pilot to compute the position of a virtual object overlay in the pilot's field of view relative to the real object it is linked to, enabling accurate presentation of a moving augmented object in the visual space. While there are other recent examples of using gaze information to correct AR-generated objects in the display [35] as well as to improve the accuracy of object selection in see-through AR applications [36, 37], to our knowledge we have not identified any gaze correction models that can function in uncontrolled random environments. Because the distances between the pilot and the UAS exceed the capabilities of the HMD platform (>15 ft), the fusion of information from a variety of sensors and sources is required to construct this model.

1.5.2 Cognitive Science

In the field of Cognitive Science, our study makes a contribution that provides a better understanding of how persistent informational cues in the superior and inferior peripheral fields affect task performance in pilots. During our literature review, we were unable to find studies that compare the use of visual cues in the superior vs inferior peripheral peripheral fields to communicate quantitative or qualitative information to users during task performance. Our study indicates that not only can persistent inferior peripheral cues enhance task performance, but that they can also enhance task performance with less effects on the user than with superior field cue placement.

1.5.3 Aerospace Engineering / Aeronautics

As part of our literature review, we were unable to identify any research on the effects of or detection of pilot-induced oscillations on unmanned multi-rotor aircraft

systems. A deep-learning neural network model implementation of the short-time Fourier transform (STFT) for real-time identification of the onset and resolution of PIO in multirotor UAS. Our research provides a mechanism to identify the onset of this phenomena and to communicate the degree of PIO severity to the pilot in a way that improves mitigation of these events. This can serve to provide insights as to the application of the existing body of research to the dynamical modes of multirotor aircraft. We also investigate the development of PIOs during the execution of MTEs during precision UAS missions. This understanding can inform future research to improve control systems for multirotor UAS.

1.6 Overview of Dissertation

In Chapter 2, we endeavor to provide an understanding of the dynamics of fixed-wing and multirotor aircraft, describe the basic functionalities of flight control systems, and describe the details the types of pilot-induced oscillations and how pilot-aircraft interactions contribute to each type of phenomena. In Chapter 3, we introduce our alternative reality system architecture, AviatAR, along with our flight-space volume model for representing the interactions between the environment, pilot, and UAS during mission execution. We will also discuss the methods of how all of these components work together to provide an AR interface that enables a high-information experience for the pilot with a low cognitive processing load. In Chapter 4, we present our experiments and their results. Chapter 5 presents the analysis of the data from our experiments and provides discussion. Chapter 6 presents the conclusions drawn from our work and identifies future research opportunities.

CHAPTER 2: SUPPORTING THEORY AND LITERATURE REVIEW

In this section, we will first provide a basic overview and comparison of the flight mode dynamics of fixed- vs. rotary-wing aircraft and flight control system methods. We will then define and describe the phenomena of pilot-induced oscillations and how the different types of PIO affect an aircraft, and then will further address the nonlinear nature of Type III PIO, which is of most interest to our research. We will then discuss some of the functions and capabilities of flight-control systems found in basic multirotor aircraft and how the functionality of these control systems may contribute to the development of Type III PIO in a pilot-aircraft system. Our focus then shifts to the pilot as a controller, where we will discuss the integration of the human pilot within the aircraft system. We will examine how the perceptive and cognitive abilities of the human pilot contribute to pilot SA and system performance, and how both of these contribute to the phenomenon of PIO. We will also review the current state of research into understanding PIOs, including the highly-nonlinear Category III PIO. Finally, we will review the state of control methods in aviation systems to identify opportunities to focus on for research.

2.1 Aircraft Types

There are two basic types of conventional aircraft that we are interested in for the purposes of this paper. The first, fixed-wing aircraft, are those for which lift is produced as a result of airflow from the forward movement of the aircraft over an airfoil-shaped wing. The second, rotary-wing aircraft, generate lift by the rotation of two or more airfoil-shaped wings on an assembly called a *rotor* about a central axis. The primary difference in capabilities between these two types of aircraft are

the methods of takeoff. Most, but not all, fixed wing aircraft are *conventional takeoff and landing* (CTOL), achieving flight after accelerating down a runway to generate sufficient lift to offset their weight. Rotary-wing aircraft, on the other hand, are generally capable of *vertical take-off and landing* (VTOL), enabling the aircraft to achieve takeoff from a nearly stationary point once the rotating wing speed and angle of attack generates sufficient lift to offset their weight. Rotary-wing aircraft are also capable of a flight mode known as hover, where the aircraft remains in nearly stationary flight over a fixed position. Aircraft designs such as the Lockheed Martin Lighting II F-35B variant and the Bell Boeing V-22 Osprey are capable of both CTOL and VTOL, as well as other flight modes, exist but are beyond the scope of this discussion.

2.1.1 Fixed-wing Aircraft

While a conventional winged aircraft is in flight, is is subject to a number of expected normal forces, shown in Figure 2.1. The most constant of these is the weight of the plane exerted by the force of gravity proportional to the mass of the airframe. As thrust is generated by the action of the propeller and forward motion of the plane occurs, the flow of air across the wings of the aircraft creates a force known as lift which is counter to the force of weight caused by gravity acting on the plane. Weight and lift produce vertical motion of the aircraft on the y-axis. While the engine of the plane is in operation, the propeller induces thrust on the aircraft, which is a pulling or pushing force on the airframe if the engine is front-mounted or rear-mounted, respectively. A sufficient forward velocity of the aircraft generates enough lift to bring the plane aloft. Counter to this force, the friction of the skin as well as the effects of the aerodynamics of the aircraft generates a counter-force to thrust, which is known as drag. Thrust and drag produce longitudinal motion of the aircraft on the x-axis. A third type of motion known as lateral motion can move the aircraft along its z-axis. This motion is induced on the plane as a function of movements of the control surfaces

in concert with the vertical and longitudinal forces on the the aircraft. Longitudinal, vertical, and lateral motions of the aircraft are referred to as translational motions and result in the movement of the aircraft through space.

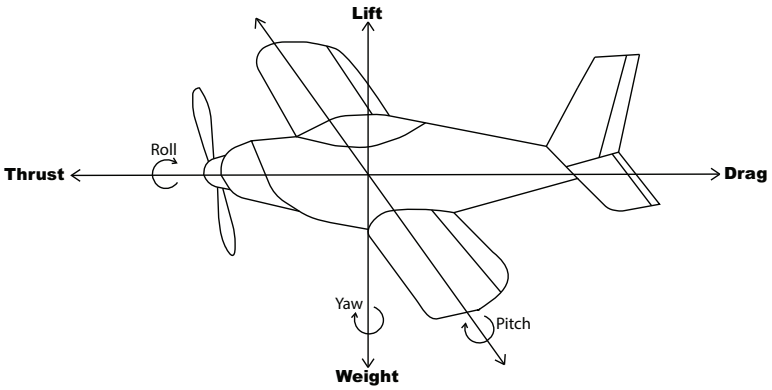

Figure 2.1: Forces and motions of a winged aircraft in flight.

In addition to these motions, the control surfaces of the aircraft produce three additional motions that govern changes in aircraft position about the x-, y-, and z-axes and, in combination, can lead to changes in the resultant *translational motions* of the aircraft. *Roll* is a rotation of the aircraft about its x-axis center-line. This motion is caused by the actions of the ailerons that, alone, does not change the direction of the aircraft's translational motion vectors. *Yaw*, a rotation of the aircraft about its y-axis center-line, is typically caused by the action of the rear rudder and, coupled with the thrust of the aircraft, can change the direction of the aircraft's longitudinal motion vector and also produce lateral motion of the aircraft. Finally, *pitch* is a rotation about the z-axis of the aircraft typically caused by the action of the rear elevator of the aircraft and can, in conjunction with thrust, directly affect the vertical motion of the aircraft as well as indirectly affecting the longitudinal vector with respect to gravitational forces generated on the aircraft. Roll, pitch, and yaw are known as the *rotational motions* of the aircraft. The combination of translational and rotational motions of the aircraft provide six *degrees of freedom* (DOF) for the motion of the aircraft.

2.1.2 Rotary-wing Aircraft

Rotary-wing aircraft, or *rotorcraft*, are a type of aircraft in which lift is achieved solely from a spinning "wing", or rotor [38]. The earliest mass-produced helicopter was the R-4 in 1942, designed by Igor Sikorski. In the common two-rotor helicopter, a primary rotary wing, provides lift to the aircraft, while a smaller rotor to the rear of the aircraft provides a counter-force orthogonal to the angular force induced on the airframe sufficient to prevent the airframe from rotating about the y-axis while enabling the aircraft to turn through a yaw motion. Forward and backward motion are controlled by a tilting of the primary rotor, changing the pitch of the aircraft and producing thrust by changing the lift vector of the aircraft. Rotary aircraft principally employ a vertical takeoff and landing (VTOL) flight strategy, although additional flight modes are possible. This VTOL flight strategy enables the vehicle to operate in areas where take-off and landing are restricted to vertical operations, as well as to hover over an area for an extended period of time [38].

Quadcopters are a type of rotorcraft with four main rotors providing lift. Each rotor acts as a wing for the aircraft, providing lift as a direct function of the thrust provided by each rotor. The forces on a multirotor aircraft in flight, as well as the motions resulting from those forces, are much more complex than those acting on a fixed-wing aircraft in flight. As shown in Figure 2.2, a quadcopter has its rotors mounted to the arms of an x-shaped frame. In this design, each pair of adjacent arms forms a 90-degree angle about a central hub and the length of all arms are usually the same to simplify control and to promote aircraft stability.

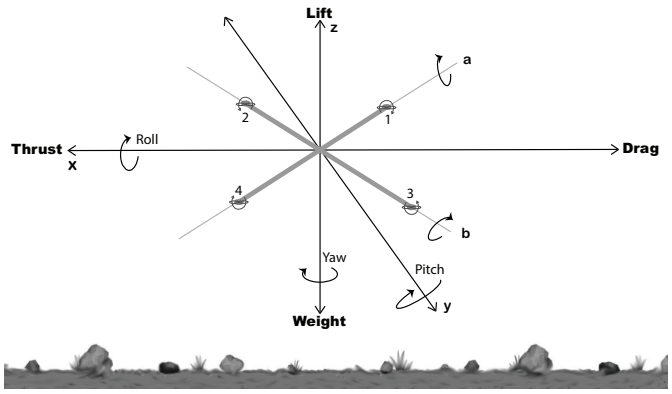

Figure 2.2: Forces and motions of a quadcopter in flight.

When a multi-rotor aircraft such as a quadcopter is hovering in a stationary position at a stationary height, all four motors must produce a constant, equivalent level of thrust, assuming a balanced aircraft body. For the vehicle to move forward as in Figure 2.3(a), it must tilt toward the direction of travel. To accomplish this, rotors (1,3) at the rear of the aircraft increase in thrust to lift the rear of the vehicle while rotors (2,4) at the front maintain their current level of thrust so that the altitude of the aircraft remains relatively constant. The reverse case in Figure 2.2(b) is similar, except that rotors (1,3) maintain their current level of thrust and rotors (2,4) increase thrust to lift the front of the vehicle. For lateral motions, a similar set of actions happen with rotors (1,2) and (3,4) coordinating their changes in thrust to achieve lateral motion.

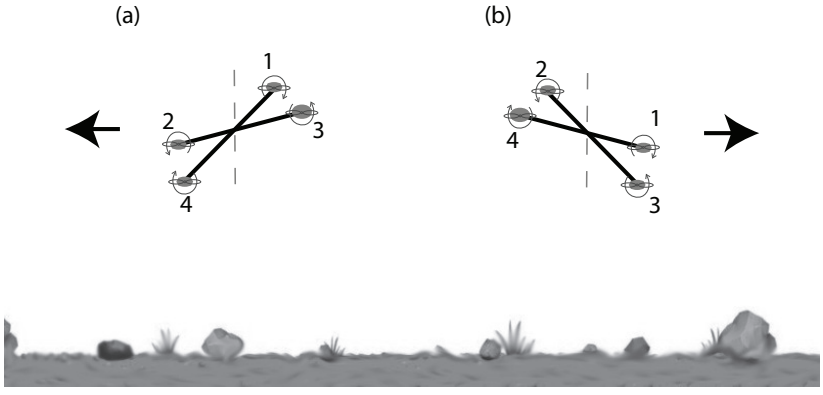

Figure 2.3: Forward (a) and reverse (b) quadcopter motion in flight.

Because a multi-rotor aircraft relies on the coordinated thrust of each rotor unit to maintain normal flight and to maneuver, the complexity associated with flight for this type of vehicle is significantly greater than normal winged aircraft. While the quadcopter has six DOF just as a fixed-wing aircraft, the quadcopter does not have the same constraints on its rotational motion as the fixed-wing aircraft. Because of this, the quadcopter is constantly oscillating over many points as it seeks to maintain its target position. If these oscillations are not sufficiently damped by the flight control system, they can saturate the flight controller and lead to catastrophic damage to the surrounding property or loss of the aircraft.

2.2 Pilot-Induced Oscillations

In the simplest terms, *pilot-induced oscillation* (PIO) are any sustained oscillation of the vehicle over a time period resulting from interactions between the pilot and the vehicle controls. While this was initially identified and principally studied as a phenomenon in aircraft operation, PIOs can commonly occur in the operation of large trucks and recreational vehicles (trailer sway), commercial buses, boats and ships, motorcycles, and automobiles [7, 8, 9, 10, 11]. In one example, Maki and Naoya studied a phenomenon in which ships under control of an autopilot will auto-orient broadside to waves when running at low speed in following and quartering seas [39]. This *broaching-to* phenomenon is the result of the yaw-roll dynamics of the vessel's motion coupled with the surge-sway dynamics of wave motion. Under this condition, they found that the application of additional effort to maintain the desired course of the vehicle did not prevent the broaching condition. The tendency of the ship to adopt a position of being broadside, or lengthwise perpendicular to the direction of oncoming waves, made the ship subject to capsize.

The Department of Defense Handbook, *Flying Qualities of Piloted Aircraft (MIL-HDBK-1797)* defines a PIO as "sustained or uncontrollable oscillations resulting from the efforts of the pilot to control the aircraft" [40]. This undesirable coupling between

the pilot and aircraft may be either a direct result of the pilots actions in attempting to maintain control of the aircraft or may be indirect in that the pilot's interactions with the controls are overwhelmingly affected in a way by some external stimuli that results in the PIO, known as *biodynamic feedthrough* [41]. One such case of an indirect PIO is a significant vibration in the airframe that is so extreme that it translates through the pilot into the controls in a feedback loop [42]. While the former is typically either a result of aircraft engineering [43, 44] or the effect of pilot "gain" induced by body mechanics [45], the latter is becoming the more predominant incident mode as aircraft designs strive to achieve higher performance, incorporate a higher percentage of less-rigid composite materials in their construction, and increasingly rely upon fly-by-wire flight control systems that can magnify nonlinear pilot-system effects [44, 46]. After decades of analysis of flights that experienced such oscillations, as well as accidents where these oscillations either contributed to or were the direct cause of the incidents, a significant focus on research into the causes of and mitigation strategies for these anomalies began in the early 1960s [5, 42, 19, 47].

2.2.1 Categories of PIOs

Three categories of PIOs have been defined based on the characteristics of the control element participating in the PIO as well as the pilot behavior coupled to the control response, shown in Table 2.1. The PIO categories are qualitative measures and are not indicative of the severity of the PIO.

Table 2.1: PIO Categories. Adapted from McRuer [12].

Category	Description
I	Essentially Linear Pilot-Vehicle System Oscillation
II	Quasi-Linear Pilot-Vehicle System Oscillations with Surface Rate or Position Limiting
III	Essentially Non-Linear Pilot-Vehicle System Oscillations with Transitions

In Category I PIO, a linear relationship between pilot input and control output is largely linear in nature [12]. For example, the feedback from the airframe oscillation to the pilot's body that intensifies effects on the aircraft's controls and causes the intensity of the oscillation to increase. This category of PIO can generally be eliminated by the pilot relaxing their body or loosening their grip on the controls [12]. This "relaxation" of the pilot's control posture is analogous to decreasing the gain on the inputs into a feedback controller [12].

A Category II PIO is described as a quasi-linear pilot-vehicle oscillation associated with control surface rate or position limiting as a causative factor [12]. In this category, either the position of a control surface cannot be adjusted quickly enough by the pilot's movement of the aircraft's controls or the position of the control surface does not match the extent to which the pilot has manipulated the controls. In situations such as aerial refueling and maneuvers at high speed, these limitations prevent rapid changes to control surfaces that could be catastrophic to the airframe, introducing a lag between pilot actions and aircraft response [48]. However, when an excursion from normal flight operation occurs and the pilot needs to exercise an exceptional level of control over the aircraft, these rate- and position-limiting behaviors can lead to situations where the positions of the pilot controls get out of phase with the control surfaces of the aircraft [46]. Related to this situation, it has been proposed that

a PIO only exists once the pilot controls are out of phase by 180 degrees with the attitude, angular velocity, or acceleration with respect to ground [49]. Category II PIOs are some of the most researched events in this area as they are severe in nature and contribute to the most crashes in comparison with all PIO-related incidents [50].

The third type of PIO, or Category III, is described as "essentially non-linear pilot-vehicle system oscillations with transitions" [49]. Whereas Category I and II PIOs exhibited a linear or somewhat-linear relationship between pilot actions and effect on the control surfaces manipulated, Category III PIOs exhibit very nonlinear transitions in either the dynamics of the control surfaces or in the behavior of the pilot [12]. These transitions in aircraft performance, from the perspective of the pilot, can appear as a failure in aircraft systems in what is known as the "flying qualities cliff" [51]. Category III PIOs can be very severe in nature and are very complicated to analyze. Category III PIOs are the type of events that we will examine in this dissertation.

2.2.2 Category III PIOs as Emergent Behavior

As stated above, Category III PIOs are characterized by interactions between the pilot and the aircraft that are non-linear in nature. What this seeks to convey is that, under the collective conditions of the pilot, the aircraft, and the flight environment at the time of the PIO occurrence, the relationship between the pilot's action on the control actuator is significantly disproportional to the resultant effect caused by the control surface on the aircraft. Also, under standard design parameters for the aircraft and normal flight conditions, such a non-linear response would not be expected to occur. Such unexpected behavior from the interaction of pilot, aircraft, and environment under normal operating conditions is similar to the phenomenon of emergence that appears in the study of complex adaptive systems [52].

In Category I and II PIOs, it has been identified that the appearance of sinusoidal cycles in pilot control-vehicle response relationships appear after the onset of the PIO

event. Because of the non-linearities associated with the Type III PIO, the normal control-response relationship appears to move about a fixed point of the system. This has been seen since the late 1940s, as aircraft design incorporated advances in technology such as jet power, shortened and swept wing designs, and supersonic flight to achieve and maintain air superiority. As these new features were incorporated into aircraft, phenomena appeared during flight that were not anticipated during the design process. Some of these conditions appeared as discontinuities in the expected behavior of the aircraft under extreme performance conditions. These jump discontinuities were later identified as Hopf bifurcations, and were previously identified by the appearance of limit cycle behavior in what were previously thought to be stable systems [53]. These systems, at worst, were believed to follow the dynamics of van der Pol or Duffing oscillators, which have stable limit cycles. This discontinuous behavior could lead to "jumps" from one operating regime to another with little warning to the pilot, giving the pilot the impression that some component or system failed mechanically, potentially causing the pilot to take the wrong course of action to recover the aircraft to a normal operating regime.

2.3 Flight Control Systems for Multi-rotor Aircraft

Most commercial flight control systems for unmanned multirotor aircraft use a *proportional-integral-derivative* (PID) controller to support stable flight operation. A PID controller uses a sum of three terms, each with their own gain, to take feedback from sensors and produce outputs to the motors to generate the desired motion of the aircraft [54]. One problem with closed-loop feedback controllers is known as windup [50]. In conventional systems where PID controls are applied, there are typically limits associated with the item being controlled. For example, if a pump has a maximum capacity to remove water from a compartment and water enters that compartment faster than the pump can remove it, at some point the control on pump speed may become saturated. No matter how much the controller calls on the pump to increase

its speed to meet the demand to remove water from the compartment, the pump's throttle control is saturated and cannot meet the requested increases. In this case, the error between the output of the controller (the speed set-point of the pump to achieve a volume of water removal) and the feedback signal (the change in water level in the compartment) will increase without bounds. One solution to this control problem is known as anti-windup methods. In an anti-windup method, once it is determined that the requested change to the controlled element (in this case, the speed of a pump) is no longer yielding the desired process improvement (the reduction of error between the process set-point and the next input from the closed-loop system), one or more of the gain parameters in the PID controller are set to zero to limit how much the system can over-saturate. The gain parameter most typically set to zero is the integration gain [55].

The flight controller on a multi-rotor aircraft piloted by a human controller (HC) typically takes its inputs from a joystick-based radio frequency (RF) transmitter, as shown in Figure 2.4. The primary motion controls on the transmitter consist of two joysticks. In the most common configuration for right-handed pilots, the left joystick controls the aggregate motor thrust affecting altitude along the z-axis using the up-down motion and the yaw motion about the z-axis using the left-right motion. The right joystick is used to control the pitch motion along the y-axis using the up-down motion and the roll motion about the x-axis using the left-right motion. These four signals are used by the flight controller to compute the speed changes for each motor necessary to translate the HC input into the aircraft's actual motion.

One significant challenge for the remote pilot with these control systems is identifying the current attitude of the UAS from a distance and rapidly translating movements of the joystick controls to match that attitude. Simple mistakes in evaluating the UAS attitude can result in significant errors in joystick motions to adjust the position of the UAS. Under the constraints of a complex mission, this can result in

property damage, injury to humans, and loss of aircraft.

In addition to distance affecting a pilot's ability to evaluate vehicle attitude, the distance between the HC and the aircraft can introduce a significant delay from when an aircraft begins to enter a dangerous situation until the HC recognizes the onset of this condition [56]. Additional time passes as the HC decides on a plan of action and reacts to the situation. Finally, there is a certain propagation delay between the HC reaction and engaging the controls and from the time of control manipulation until the actuator response affects the drone. The combination of these delays in command execution can be perceived by the HC much in the same way that controls response in a human-piloted aircraft subject to rate limiting is perceived by the pilot.

Figure 2.4: Typical RF transmitter used for remote-control aircraft operation. Image courtesy of Horizon Hobby, LLC.

2.4 The Pilot as a Controller

When studying the augmented control of a remotely-piloted semi-autonomous aircraft, we must understand the contribution of the human pilot to the control of the system as to enable a harmonious collaboration between pilot and computer. The pilot, in fact, becomes part of the aircraft control system. In this section, we seek to

better understand the effects of a pilot's neurological and cognitive processes on their neuromuscular system that serves as the pilot-machine interface in this system.

2.4.1 The Human Pilot

In the simplest case of a human operating any type of non-autonomous vehicle, a very simple model can be created to describe the control of a vehicle [6]. In Figure 2.5 (a), we have a simple control-feedback loop that takes an input from the environment and produces a system output that represents the new vehicle position and motion after one epoch of control. The input is referred to as the *system forcing function*, $i(t)$, and represents the motion of the target or the desired location for the vehicle to obtain. The next block in the diagram is referred to as *display*, and this represents the pilot's perception of the target's position and motion relative to their vehicle as well as the error in vehicle position as the gradient computed from one or more previous epochs of control. From this information, the pilot can make adjustments in an attempt to track the target more closely in the next epoch. One problem with this simplified model is that it lumps all of the pilot's perception, cognitive function, neuromuscular system function, and environmental effects into a single error term to add to the next input from $i(t)$.

A somewhat more detailed version of this model is seen in 2.5 (b). This version of the model still contains all of the components of the previous model, but also includes feedback from psychophysiological and physiological measures from the sensory dynamics and human operator system blocks [6]. By capturing variables from these sections of the pilot-vehicle system, the model can better learn how each stage of the system contributes to overall system performance.

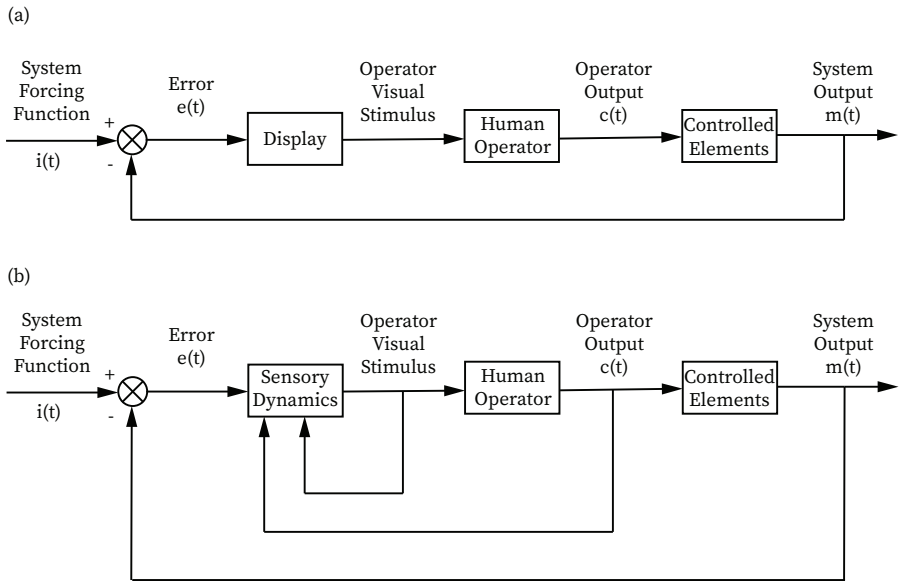

Figure 2.5: Simple model of pilot-vehicle control. (a) A simple control-feedback loop. (b) A more complex model with multiple internal feedback loops.

Consider the case of a student pilot practicing a game of "follow the leader" in a simulator. The goal of this exercise is to have the student follow a lead plane as closely as possible, mimicking its movements to learn control of the aircraft. Figure 2.6 contains a theoretical output of values of each of these functions over time. The system forcing function $i(t)$ in this case is the position of the lead plane that the pilot is following. The system output, $m(t)$, is the position of the student's plane throughout the exercise.

We see that the student's plane tracks closely with the lead plane throughout the exercise, as comparing the values of $i(t)$ and $m(t)$ over time. We also note an almost identical track between the positional error of the student's plane as recorded by $e(t)$ and the changes in operator output $c(t)$, lagging by approximately 150 milliseconds to represent the cognitive delay of the pilot between recognition of the error and actuator movement to correct the error [6]. These continual adjustments by the student are almost sinusoidal in nature, and feed back into the system error term $e(t)$ along with position changes from $i(t)$. It is easy to infer how these frequent changes in $c(t)$ could lead to larger and larger cyclical changes in $m(t)$ that may eventually result in

loss of control of the aircraft without sufficient damping. To help reduce the effects of these types of pilot-vehicle coupling, a damping method known as *actuator rate limiting* was introduced into the flight control systems of aircraft to attenuate the high frequency signal [57].

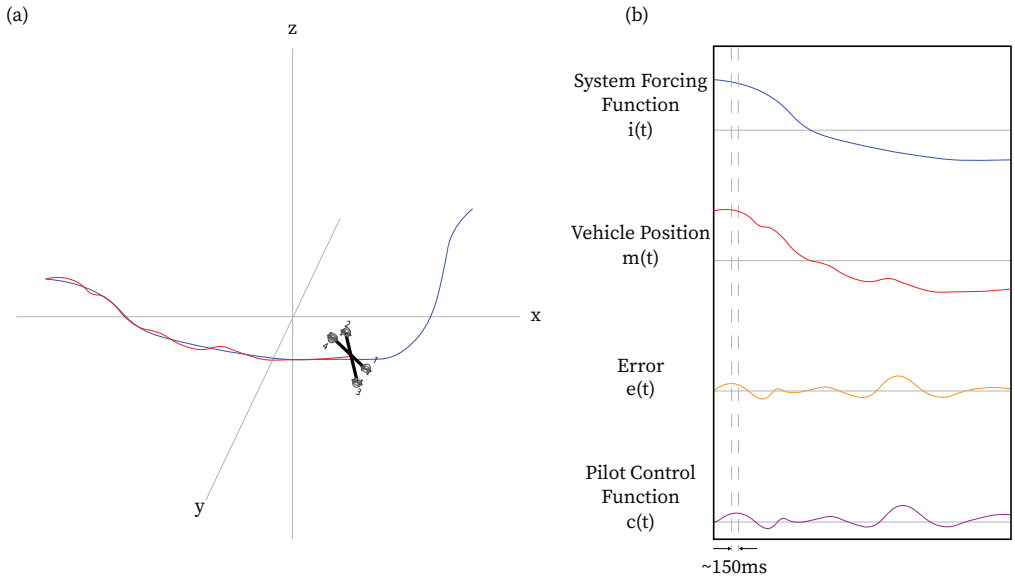

Figure 2.6: A representation of a pilot playing "follow the leader". (a) A map of the aircraft's position over time vs the target trajectory. (b) An output graph of the state of the pilot-vehicle model in compensatory mode.

2.5 Perception and Cognition in the Human Pilot

While in flight, a human pilot is subjected to a broad range of sensory stimuli from the environment, the aircraft, and the numerous controls and communication systems employed in modern avionics systems. While the pilot may perceive the state of an aircraft from motion resistance and haptic feedback in the control actuators [24, 25, 23], the sensing of auditory motion of the aircraft and its surroundings [58], and perception of forces acting on the aircraft via the vestibular system [59, 60], the engaged pilot receives most of their information to actively control an aircraft from visual input. It is therefore crucial to keep in mind the cognitive capacity of a pilot when designing an aircraft system for its mission.

One major goal of aircraft systems design is to enable a high degree of pilot *situ-*

ational awareness (SA), as defined by Endsley in ([61]). A pilot's SA can be defined as the degree to which a person is cognizant of their surroundings and the activities taking place within, how well they comprehend the consequences of these activities on themselves and their interests, and how well they can incorporate those consequences into their mental model of the immediate and longer term time frames. These mechanisms of perception affect pilot situational awareness and enable the pilot to switch perception modes effectively to maintain or regain situational awareness while operating the aircraft.

In this section, we will review the *successive organization of perceptions* model used to describe the three modes of human pilot, discuss SA and how it relates to SOP, and review how the human visual and neuromuscular systems inform and relate to the human control of an aircraft.

2.5.1 Successive Organization of Perceptions

Beginning in the 1950s, researchers began to study how pilots learn to interact with their aircraft and how this can affect their ability to recognize and respond to excursions from normal operation of their aircraft. One of the first models, *successive organizations of perceptions* (SOP), was derived from the prior work by Annett and Kay related to the interactions and feedback processes between industrial machine operators and their machines [19, 62]. In the SOP model, pilot behavior is classified into three modes of operation. *Compensatory* mode is effectively the condition of a novice pilot. The pilot tracks an objective and makes immediate adjustment to the controls to keep the plane tracking strictly to optimally reach this objective while following a set of fundamental "laws" for control of their aircraft [6].

In *pursuit* mode, the pilot relies upon their experience and training to guide them not only about what to expect during a mission, but also how to react to those events when they occur. While the pilot still tracks the objective and actively controls the aircraft to achieve that objective, experience can also guide the decisions and

enable the pilot to make short-term predictions to further inform those actions. Both compensatory and pursuit modes are tight closed-loop control mechanisms between the pilot and the aircraft.

In *precognitive* (precog) mode, the pilot operates under the mode that they have effectively complete information about the state of the mission as well as the state of the aircraft [19]. Under these assumptions, the pilot relies upon their knowledge and experience to make decisions well in advance of situations that arise, taking actions based on a priori assumptions of what will happen as opposed to direct feedback from the system. This is really an almost open-loop synchronous interaction between the pilot and aircraft that resembles pursuit mode but with negligible lag between pilot observation and action, sometimes even pre-action by the pilot in anticipation of a future state, as long as there is close tracking between the pilot's precog actions and the response by the system [47]. As a result, it is likely that a deviation between the actual and planned trajectories of the aircraft will begin to diverge. When this happens, the pilot moves back to pursuit or even compensatory mode until the flight begins to track to precog inputs once again.

One important finding from this research is the insight that the HC reaction-time lag can have a significant effect on the controlled element (CE) of an aircraft, especially during unexpected high-frequency, high-intensity events, such as Category III PIOs. It was intuitive that these shifts among the various perception modes can have a knock-on effect on pilot ability to respond to nonlinear excursions from normal flight patterns [63].

2.5.2 Situational Awareness of the Human Pilot

Situational awareness (SA) can be defined as the degree to which a person is cognizant of their surroundings and the activities taking place within, how well they comprehend the consequences of these activities on themselves and their interests, and how well they can incorporate those consequences into their mental model of the

immediate and longer term time frames. With respect to the operation of an UAS, SA is the ability of the operator to understand and maintain awareness of how flight-related elements affect the operator's current and future levels of performance [64]. These flight-related elements include risk elements from the broad categories of flight, pilot, aircraft, environment, and mission. It is critical to an operator's maintenance of SA that changes in these flight-related elements during the mission are internalized by the operator and any necessary mission changes are actively incorporated into the flight plan.

2.5.2.1 Endsley's Situational Awareness Model

In Endsley's Situation Awareness Model, there are three levels of SA that a subject can achieve [65, 61]. The first is an awareness of the events and conditions of the environment around the subject. The second level is the subject's ability to incorporate these events and conditions into their narrative, to understand and to be able to explain how they and others around them are affected by the events. The third level extends this even farther, to the point where the subject can project possible future states that integrates this awareness and can be used for planning.

We can extend these levels to the paradigm of UAS operation. In Level 1 SA, the operator can perceive the flight-related elements from the surrounding environment. Level 1 SA is that of an interested observer of an activity might attain. Level 2 SA extends the operator's perception of these elements into an integration of this data to produce an understanding of the current situation and how the flight-related elements affect the current state. Level 2 SA represents the capability of an apprentice / student operator or even an experienced operator with no training on the particular aircraft system employed by the mission. The highest level, Level 3 SA, is when the operator is capable of projecting the future state of the environment given the sensor inputs, system knowledge, and experience, and to select a course of action (COA) using that information. Level 3 SA is the degree of awareness demonstrated by an

experienced pilot who is trained and experienced on the particular aircraft system employed for the mission.

2.5.2.2 The Observe-Orient-Decide-Act (OODA) Model

One model of the SA concept in decision making is the *observe-orient-decide-act* (OODA) loop, developed by USAF Col. John Boyd [66]. This is a closed-loop feedback loop where an operator gains a mental picture of a situation and its constraints, applies knowledge to produce a set of possible actions to take, and selects a COA. Once this COA is taken, the operator observes the actual outcome attributed to the COA as well as any new inputs and then repeats the OODA process. The observe, orient, and decide actions in this loop align to SA Levels 1 through 3 respectively.

The OODA loop is most closely associated with high-level information fusion (HLIF) process associated with large-scale information gathering and intelligence activities. In HLIF, loosely-coupled and weakly-correlated source (e.g., human-generated "soft") data and sensor (i.e., "hard") data is combined during the observe and orient phases of the process. These analysis processes lend themselves well to a sequential process of independent activities of intelligence product creation, interpretation, decision-making, and execution of a COA.

2.5.2.3 The Recognition-Primed Decision Model

Another model of SA in decision making is Klein's *recognition-primed decision* (RPD) model [67]. This model was developed through Klein et al.'s observations of fire platoon commanders' decision-making processes during emergency events [68]. When interviewed, fire commanders consistently stated that their selected COAs were chosen based on recognition of patterns from past experiences from training or prior missions. Additionally, these commanders recalled that they didn't have any internal or external debate over alternate COAs to select the optimal choice, but they immediately homed-in on their selected COA as a result of their observations of the unfolding situation.

The RPD model starts with the observation of the situation and determining if the observer recognizes it as a known archetype or as similar to a prior experience. Once this recognition occurs, four types of information are produced as a result. These are: an expectation of events and outcomes associated with the situation; a set of cues for the decision maker to determine if the recognized situation is still accurate or if the situation must be reevaluated; a set of goals that are realistic given the situation; and a set of typical actions taken given the situation. In a simple situation where there is only a single COA available, that action is selected and the result observed. In a more complex situation where there are multiple COAs available for the situation, each action is evaluated to determine its effectiveness and order of application to the current situation. Once this evaluation is complete, the selected COAs are executed and the results observed. At any point during the execution of the planned COAs, the plan may be modified as the situation unfolds; principally, this occurs when the observer recognizes the situation morphing into another recognized archetype.

A major strength of the RPD model is that it overcomes the OODA assumptions of a fairly static environment with a sequential chain of independent activities. The RPD model expects a dynamic and changing environment that can interrupt and change the current COA without re-starting the OODA process loop [69].

2.5.3 The Human Visual System as Related to SOP

As mentioned at the beginning of this section, most of the information that a human pilot operates from is informed by visual processes. This may come from visually scanning the environment at various distances out from the aircraft, interpreting *augmented-* or *mixed-reality* (AR/MR) information provided by *heads-up displays* (HUDs) painted on the aircraft canopy, or by observing instruments and controls inside of the aircraft cabin. To better understand how the presentation of information to the pilot affects the SOP mode and maintenance of pilot SA, we will do a review of the human visual system and how its components and functions can inform avionics

systems design.

The human eye is the optical sensory organ that captures images and converts it to neural impulses. This is accomplished via the lens, cornea, pupil, and iris that, together with feedback from the retina, control the focus, magnification, and amount of light presented to the retina for conversion to neural impulses. In Figure 2.7, we see a representation of this structure. As light enters the eye, the image is inverted by the lens and is refracted onto the retina. There are actually two different areas of the retina that are of interest to us. As the image entering the eye is flipped, the outermost regions of the visual field are projected onto the nasal retina of each eye, while the central area of the visual field are projected onto the temporal retina of each eye. From this, we can see that stimuli associated with peripheral vision will be processed by the nasal retina of each eye.

As these neural impulses leave the eye via the optic nerve, the nerve of each eye enters a structure of the brain called the *optic chiasma*. In this structure, signals from the left and right temporal retinae are routed to the left and right *lateral geniculate nucleus* (LGN), respectively [70]. While signals from the temporal retinae remain on the same side of the brain as the respective eye that sensed the information, signals from the nasal retina of each eye cross to the opposite side's LGN. This means that signals from the periphery of the left eye cross the optic chiasma and are sent to the right LGN, and vice versa.

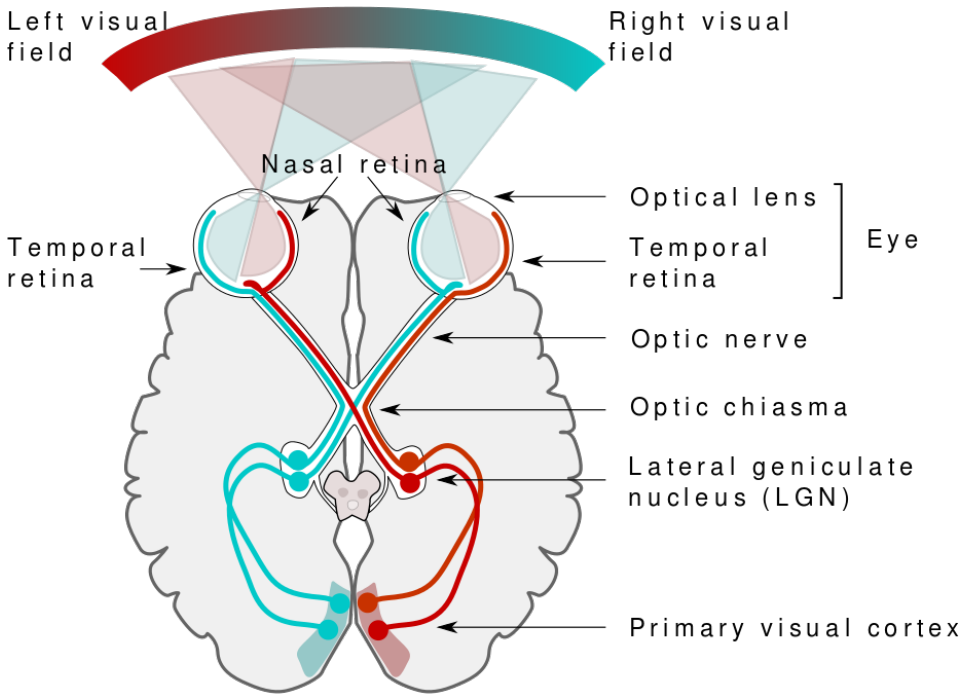

Figure 2.7: Illustration of the human-visual pathway, from the eyes to the lateral geniculate nucleus. ©Miquel Perello Nieto / Wikimedia Commons / CC-BY-SA-4.0

The LGN takes the signals from the optic nerve and mixes them with information from other parts of the brain, such as the visual cortex and the superior colliculus. This information then leaves the LGN via two pathways through the optic radiation to the primary visual cortex. The optic radiation is made up of the axons from the left and right LGN to the left and right primary visual cortex, respectively. The two pathways from the LGN to the visual cortex each carry information from different parts of the retina, as illustrated in Figure 2.8. Signals from the lower half of the field of view travel via the *dorsal stream* through the upper region of the optic radiations to the upper part of the visual cortex, while signals from the upper half of the field of vision take a longer path to the lower visual cortex via the *ventral stream* via a structure known as *Meyer's loop*.

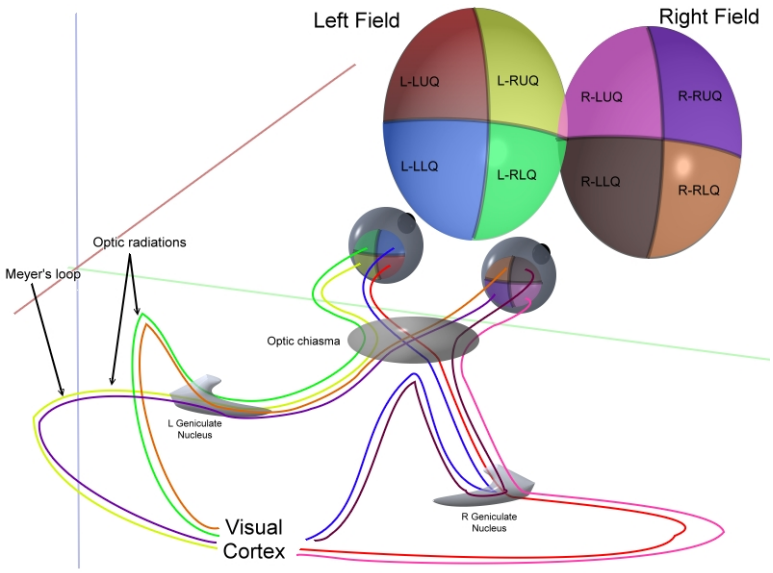

Figure 2.8: Illustration of the human-visual pathway, from the eyes to the lateral geniculate nucleus. ©User:Ratznium / Wikimedia Commons / CC-BY-2.5

Originally, the ventral and dorsal streams were known as the *what* and *where* visual streams, as initial investigation of the ventral stream seemed to be more closely associated with identification and classification functions while the dorsal stream seemed to be more associated with object tracking and motor actions [71]. As more and more clinical evidence was collected from patients with various brain injuries, this strict interpretation of the systems became less supported [71, 72]. One current hypothesis is that the ventral stream produces a higher-resolution view of an area of specific focus, while the dorsal stream samples the larger field of view more often and at a lower resolution than the ventral stream. This is the basis for the *exploration and exploitation* model proposed by Sheth et al. in ([72]). In this model, the ventral system works to provide a rich understanding of the area of focus by the individual (i.e., "exploitation"), while the dorsal stream constantly scans the periphery to detect low-resolution signals of novel events such as motion or changes in background color or brightness intensity (i.e., "exploration") [73]. These differences in processing types suggest different scanning strategies for eye movement. The exploitation behavior proposed for the ventral mode strategy requires eye saccades over a very small range

of motion, typically $< 10^{\circ}$ range of motion from the point of interest [72]. The exploration mode, in contrast, requires saccades with a much broader range of motion, typically $> 20^{\circ}$, to produce a sufficient *visual space* to support situational awareness [72, 74, 75]. The effects of these modes have been verified using functional magnetic resonance imaging (fMRI) by Barton and Brewer in ([76] and the effective visual space size necessary to support the information processing capacity of each mode has been modeled using genetic programming (GP) techniques in ([74, 75, 77]).

2.5.4 Neuromuscular Models of Pilot Response

To better understand how the cognitive states outlined by SOP affected pilot response, research began to integrate the human physiological effects of cognition and reaction into the closed-loop pilot-aircraft model. In the closed-loop model of the pilot neuromuscular actuation response developed by McRuer in ([5]), the neural time delay as well as the activation of muscle spindle complexes during an event introduced an initial overshoot in response level, which settled to the desired response level in an operator-specific effective time delay. This time delay, τ_e, was identified to be proportionate to the dynamic tension of the pilot. The level of tension in the pilot's musculature had a measurable and significant effect on the lead time (τ_{lead}) from the point of action onset to the steady-state output, as well as the lag time (τ_{lag}) between the time of recognition that a new action was required and the point of actual response to that signal [5]. This dynamic tension of the pilot was referred to as *pilot gain* in the system model. One basic insight from this is that a relaxed pilot is less tightly-coupled to the aircraft, which has a dampening effect of pilot interactions on the system as the required pilot bandwidth to respond to stimulus from the aircraft system decreases [5].

2.5.5 Mathematical Models of HC Behavior

The next seminal work was the analysis and documentation of dynamical systems models of how the human body as controlled by the *neuromuscular system* (NMS) behaved under various environmental and physiological conditions. McRuer and Krendel sought to distill the essence of all available and viable insights from research up until that time to codify a cohesive set of mathematical models and principles related to the dynamics of HC performance under the SOP modes of pilot behavior [6]. While the detailed content of this document isn't directly important to our review, it must be understood that practically all research in pilot dynamics is based, either directly or on derivative works, on this document.

It is also easy to envision how various methods of training artificial neural networks could be used to train individual specialized models (e.g., the sensory dynamics and human operator blocks) on a broad variety of inputs. These specialized models can then be then incorporated into larger, more complex deep models of the larger pilot-vehicle model. This concept has been used in practice since the early 1990s in applications such as stacked neural networks used in chemical process control systems [78].

2.6 Bifurcation Analysis and Catastrophe Theory Methodology

In 1979, Mehra and Carroll devised an approach that applied methods from topology, bifurcation analysis, and catastrophe theory to a specific class of instabilities that appeared during high angle-of-attack (AOA), or high-α, conditions [53]. Their goal was to provide a methodology capable of indicating aircraft stability taking the whole system of systems into account. This was a necessary condition of completion for the methodology, as it had been shown that the interactions between the systems and components of the aircraft, along with pilot dynamics, produced nonlinear phenomena at high-α conditions.

Bifurcation Analysis and Catastrophe Theory Methodology (BACTM) was a tool for analysis of the nonlinear systems. It enabled engineers and designers to determine the stability of the system, the presence of limit cycles about system states, and a characterization of bifurcation and jump behaviors present in the system [53]. BACTM could be used to analyze $(x + c)$-dimensional systems, where x and c represent the number of state and control variables in the system, respectively. The primary difference in the quality of these two types of variables is their rates of change; state variables varying rapidly as the system develops, and control variables changing more slowly as the pilot interprets the aircraft state and decides upon a course of action [53].

Once the state and control variables are specified and conditioned, the equilibrium surfaces of the system are computed by solving a system of nonlinear equation in terms of the variables. The goal of this is to produce a polynomial that can be reduced to a canonical model under catastrophe theory; otherwise, the solutions resulting in an equilibrium state can be found using iterative methods [53]. Once the equilibrium surfaces have been identified, iterative methods are used to compute the bifurcation surfaces under which jump dynamics exist. These surfaces are then used to infer the nonlinear phenomena present in the system [53]. One such item confirmed using this method was the existence of *Hopf bifurcations* as a cause of jump discontinuity behavior postulated years earlier [53].

2.7 Manual Control Cybernetics - State of the Art

Now we jump forward over three decades to understand how things have changed. In 2017, Mulder et al. published a review of the state of the current trends and state-of-the-art methods in ([79]). Mulder et al. describe the previously-mentioned methods as being the state-of-the-art in control cybernetics theory "developed in the 1960s ... for 1960s technology" [79] and describes it as inadequate to move our understanding forward without significant additional research. One such inadequacy is

that the performance of a human operator is generally modeled as a unitary process that, given a sometimes complex set of inputs (stimuli), produces an output that cannot necessarily be analyzed to understand the reasoning used to achieve the output. To help enable the next set of advances in control cybernetics necessary to achieve the goal of an adaptive human control model, Mulder et al. have proposed a novel five-step framework to guide future research.

The first two components of the framework are develop an understanding of (Step 1) pursuit and (Step 2) preview modes of pilot operation in terms of how to develop a universal model that includes them. Pursuit, as described in the context of SOP in Section 2.5.1, is the expected behavior from a competent, experienced pilot where a combination of objective-seeking and optimal control is used in mission execution. Preview is an extension of the pursuit mode where the pilot has visibility to not only the immediate view in front of the plane plus the visual information used in the pursuit task, but also can see several seconds or more of where the plane will travel [80]. These cues about the future state of the mission can then be incorporated into the decisions made by the pilot in pursuit mode to improve the decision-making activities of the pilot.

An example of this can be seen in Figure 2.9. If the pilot is operating in a purely compensatory mode, they are focused strictly on acquisition of the target and is reacting on minimizing the distance (error) between the crosshairs and the opponent's aircraft. When the pilot is in pursuit mode, they are still focused on the mission objective - acquiring the enemy's aircraft - but they take more of the surrounding environment into account when making decisions. In the referenced example figure, the pilot sees the approaching mountain range and can begin to alter their course, knowing that the opponent will likely make similar course adjustments to avoid a crash. In the extended case, where a preview of several seconds is available to the pilot, a different decision may be made as a result of including that information in

the decision-making process. For example, if the pilot "sees" the approaching enemy formation approaching in the distance, a decision to abort the mission to avoid contact with a superior number of enemy aircraft may be selected as the prudent course of action. This ability to include future information, gained either by natural vision or through radar, satellite imagery, or other sensor mechanism, provides the equivalent of a time-advance preview of what will happen beyond the window used for normal pursuit-mode decision-making.

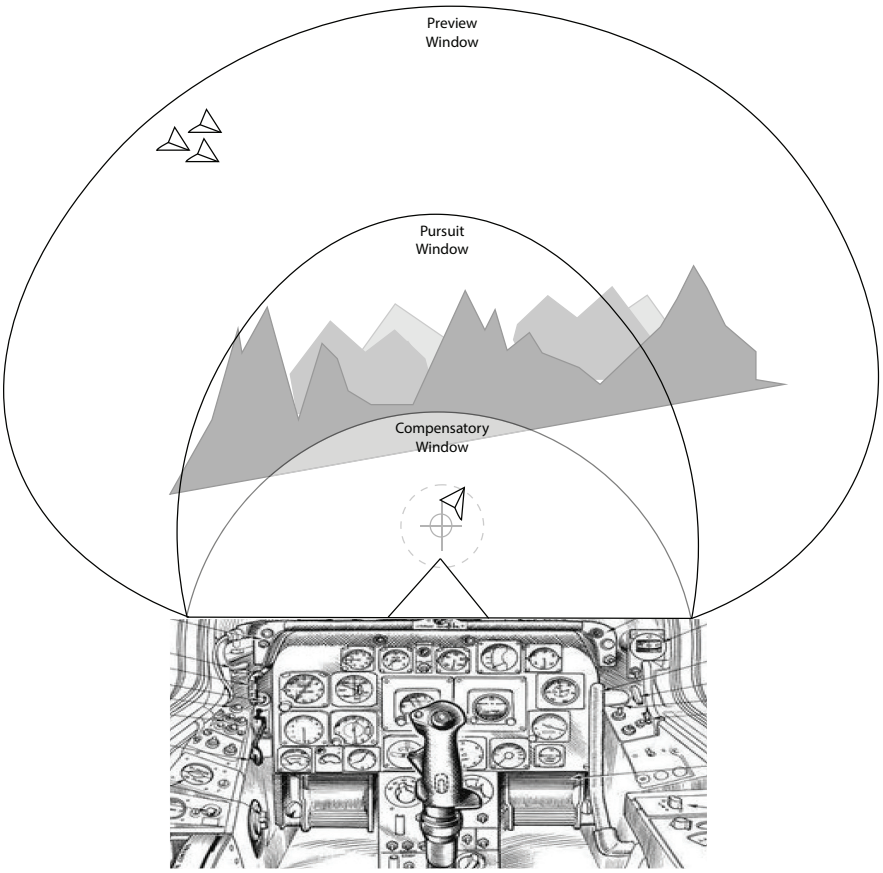

Figure 2.9: Illustration of the compensatory, pursuit, and preview timescales. Adapted from van der El, et al. in ([80])

Step 3 of the novel framework is to isolate the neuromuscular adaptations of pilots and model each of these components to understand how they affect pilot dynamics. Whereas McRuer et al. considered the entire NMS of the pilot along with their cognitive functions as a single unit of "pilot gain" in the aircraft-pilot model in ([6]),

the novel framework in proposes a much more detailed model of the individual NMS components develop and contribute to the performance of the pilot [79].

The final two steps of the novel framework address the cognitive components of the HC. Step 4 is related to understanding how a pilot learns a set of tasks and develops the deep competency in those tasks required to advance from a novice to a skilled professional pilot. This can help to better understand the relationship between the development of competency in a task and the effects to the NMS components associated with performance of the task [79]. Closely related to learning, Step 5 focuses on understanding how a pilot learns to adapt to different situations that don't match their internal models learned from previously-encountered scenarios. In this situation, the pilot selects the best action given prior experience. Regardless of the result, new knowledge is learned from the situation and the pilot's knowledge base is broadened through a form of reinforcement learning [81].

While Mulder et al. describe the current models in manual control cybernetics as woefully under-powered, they present a few innovations in the field that contribute meaningfully to their roadmap [79]. The first of these is related to understanding the methods in which a HC to integrate information from the preview activity into their responses related to the pursuit mode activity. In most current HC models that include preview tracking as a feature, the base model derivation comes from the family of two-channel extended convolution models, the CE predictor models, or the HC optimal control models [80]. In each of these classes of models, assumptions about the effects of preview on the HC performance are statically integrated into the structure of the model. The goal in ([80]) was to have the model learn the contributions of preview on the HC and to evaluate the learned models against the three standard model types proposed by Sheridan in ([82]). The model learned using this method identified two distinct preview tracking responses not found in Sheridan's three classes of models. The first response, described as the *near-viewpoint* response,

examines the environment from 0.1 to 0.9 seconds out from the target [79]. This near-viewpoint response makes up the majority of the preview component of HC response and is complementary to pursuit mode for high-frequency objective tracking. The second component, the *far-viewpoint* response, focuses on a region 0.6 to 2 seconds beyond the target. This second response is used by the HC to track low-frequency components in the target region [80]. The presence of this feature correlates to reduced vigilance by the HC on the primary target.

Another finding of interest by Mulder et al. is the adaptation of the HC response to sudden changes in target motion or the operating conditions or surroundings. Of significant interest to us are the shifts between automatic and manual control responses, in which the HC may shift from precognitive mode to pursuit mode while re-establishing tracking with the target and the environment to increase situational awareness [79]. These slow variable changes are associated with fatigue, loss of awareness, and learning saturation and may create a new signal that serves as an indicator of reduced control or loss of HC situational awareness.

2.8 Cognitive Delay as a Causative Agent of Steering Oscillations

Sharma et al. in ([83]) examine the effects of cognitive delay on the generation of steering oscillation in human automobile drivers. As previously mentioned, we believe that there are strong similarities in the cognitive operations of the human operator of any vehicle and their effects on the introduction of emergent behaviors such as PIOs; therefore, we include their findings in this analysis. The focus on Sharma et al.'s work is that of inadequate focus of the HC on the driving task either because of inadequate cognitive ability or insufficient cognitive capacity at that moment in time [83]. By inadequate cognitive ability, one meaning provided by the authors is that the HC temporarily may be incapable of performing at their normal level because of fatigue or some similar reason. Another meaning is that the cognitive skill of the HC degrades over time because of technologies that augment operator capabilities, such

as anti-lock breaks, traction control systems, or other features that cause the HC to lower their level of task vigilence [83]. Similarly, the intent of insufficient cognitive capacity means that the HC has either allocated attention to activities unrelated to vehicular control or the volume of traffic or the complexity of the driving situation exceeds the ability of the driver to manage or cope with the situation at hand [83]. In either case, Sharma et al. hypothesized that any delays affecting the performance of the HC but not directly leading to the immediate termination of vehicle travel would manifest as a pattern of oscillations in the HC control function, $c(t)$ [83]. Their reasoning for this was the application of the Nyquist stability criterion satisfying a condition for maintaining the oscillatory state [84]. Sharma et al. proposed that the identification of these emergent oscillation patterns could be used to signal a form of preemptive alert to the vehicle operator of their reduced capacity for vehicle operation [83].

To test this hypothesis, Sharma et al. developed a model driving agent using genetic programming (GP) methods to simulate a human driver under optimal conditions. This agent operated a simulated vehicle using The Open Source Racing Car Simulator (TORCS). Once an "optimal" agent was produced after 100 epochs, the code was modified to allow for the introduction of an operator delay, τ, to better represent to the cognitive delay of a human driver. For the purpose of their experiment, they tested values for τ of 0ms, 100ms, 200ms, and 400ms for three different test cases: straight road driving, entering a corner, and exiting a corner, each for a 2s interval [83]. For each of the three cases, a perceptible and increasing oscillation appeared in the changes in steering angle applied by the agent over the travelled distance as τ increased over its range. However, for the corner-entry and corner-exit cases, as τ exceeded 100ms, steering angle adjustments by the agent exceeded the boundary of safe and comfortable operation in both cases [83].

The results of the delayed agent in this experiment exhibited similar behavior to

a human pilot operating under the compensatory mode of SOP discussed in Section 2.5.1. This result demonstrates that this GP agent model used by Sharma et al. could potentially serve as a basis for a HC model for aircraft pilots.

2.9 Eye Tracking Behaviors During Flight

In ([85]), Korek et al. sought to correlate pilot ocular activity as a proxy for SA during a specific flight activity known as an *offset landing maneuver*. In this standard test activity, a pilot on-approach for a landing must change to an adjacent parallel runway for a landing [86]. Given enough advance notice of the change, the pilot can easily adjust course in a smooth s-shaped maneuver to line-up with the new runway for approach. However, as the notice of the required change comes with less distance from the touchdown point, the pilot is required to execute more aggressive actuator commands and devote more visual attention outside of the cockpit to successfully line-up the aircraft with the adjacent runway.

In their experiments, Korek et al. used eye-tracking instruments to capture the eye position of pilots throughout the offset landing procedure to quantify the changes in pilot gaze time percentages between the primary flight display (PFD) instruments and focus outside of the cockpit as the test parameters changed. These tests were performed with two pilots, one of which was a commercial line pilot while the other was a seasoned test pilot. Each pilot performed three variations of the landing: (1) a baseline landing that did not incorporate the offset procedure; (2) an offset landing starting a 4 nautical mile (nm) from the runway; and, (3) an offset landing starting at 2 nm from the runway. Their tests demonstrated that pilot visual attention was focused outside of the cockpit for an average of 82% of the time during the simulation, making it the most important element of pilot attention during this maneuver [85]. In reviewing the data from the experiment, we noted that the test data indicated that the line pilot, being less experienced under a broad range of flying conditions than the test pilot, exhibited a much stricter return to pursuit mode SOP flight patterns

than the test pilot during the offset landing maneuver. This can be deduced from the larger magnitude of yaw and roll actuator motions in each trial. These oscillations increased significantly for both pilots as the notification of runway change approached a 2 nm limit [85].

The conclusion drawn from these trials by Korek et al. was that pilot attention in high-workload situations was primarily focused on the area outside of the cockpit [85]. Also, this led to an assumption that PFD components such as airspeed, attitude, and altitude readouts that are frequently referenced during high-workload activities should be located closer to the window boundary on the aircraft to minimize the ocular transition time from PFD to window and back [85].

CHAPTER 3: PROPOSED APPROACH - AVIATAR

From our research, it is clear that enhancing pilot situational awareness, mission workload management, and aircraft control are current and active areas of research. We believe that work done in these areas can be applied to various other operational media. For example, the phenomenon of pilot-induced oscillations remains an open research problem not only in manned aircraft flight [87, 41], but also in ships [39], automobiles [8, 11, 83], large trucks [9], trains [7], spacecraft [49], and even wheelchairs [4]. While the manifestations and degree of these PIO are many and varied, there are commonalities of cause among the different types.

With a goal of increasing pilot capabilities by optimizing available operator bandwidth, we propose an augmented reality system called *AviatAR*. AviatAR, an Aviation-centric Augmented Reality system, is an integrated system of sensors, processing systems, and a see-through head-mounted display based on the Microsoft (Bellevue, WA) HoloLens 2 mixed-reality glasses, shown in Figure 3.1. The HoloLens head-mounted display (HMD) is coupled with an application built using Unity Technologies (San Francisco, CA) Unity Pro software and the Microsoft Mixed-Reality Toolkit (MRTK) to present real-time information to and to interact with the pilot. The goal of this HMD system is to maximize the information flow to the pilot in a way that minimizes distraction from mission tasking and cognitive workload load required for information processing. This method, derived from the research done by Matthews on *glanceable displays* in ([88]), seeks to balance the information content and symbology of the UI components to keep the total cognitive processing level of the pilot to a minimum, leaving sufficient cognitive budget for the pilot to deal with unforeseeable situations that may arrive during a mission.

For the purpose of our study, we will adopt the terminology used by Descheneaux et al. in ([89]) to describe the terms augmented reality and virtual reality, as well as to differentiate among the methods used to achieve augmented reality. *Augmented reality* (AR) is when the user principally sees the real world with augmented images projected onto that image. *Virtual reality* (VR), on the other hand, is when the user sees an artificial world with representations of real-world and augmented objects projected into it. Descheneaux et al. describe two types of augmented reality implementations. The first is called *video see-through*, which is when the viewer sees both the real environment captured by cameras along with the augmented virtual objects added to the environment through digital displays. The second is described as *optical see-through*, which is when the viewer sees the real environment through a transparent lens and augmented virtual objects are added to the environment are projected onto the lens using methods such as prisms. Optical see-through AR is the method employed by the Microsoft HoloLens 2 HMD device.

Figure 3.1: Image of Microsoft HoloLens 2 mixed-reality glasses.

3.1 System Purpose and Method of Operation

The principal purpose of AviatAR is to enhance the UAS pilot's SA during flight mission operations by providing flight quality and telemetry information to the pilot in a manner that consumes minimal cognitive budget of the pilot. To accomplish this goal, we have implemented a set of low-complexity visual cues that are overlaid with the scene that the pilot views through the clear lenses of the HMD. We believe that using an optical see-through method presents a lower cognitive workload for the pilot to accommodate information, especially augmented informational cues meant to overcome issues associated with pilot-vehicle distance.

One such problem for remote pilots is the perception of small-scale changes in vehicle attitude associated with UAS motion from a distance. What may be a sufficient change in attitude to affect UAS flight quality may be imperceptible to the remote pilot. Furthermore, these imperceptible changes, if left unchecked, can lead to emergent behaviors that may jeopardize achievement of the MTE or even lead to damage or catastrophic loss of the aircraft, such as PIO. As an example of this, let's look at the pitch and roll profile shown in Figure 3.2 (a).

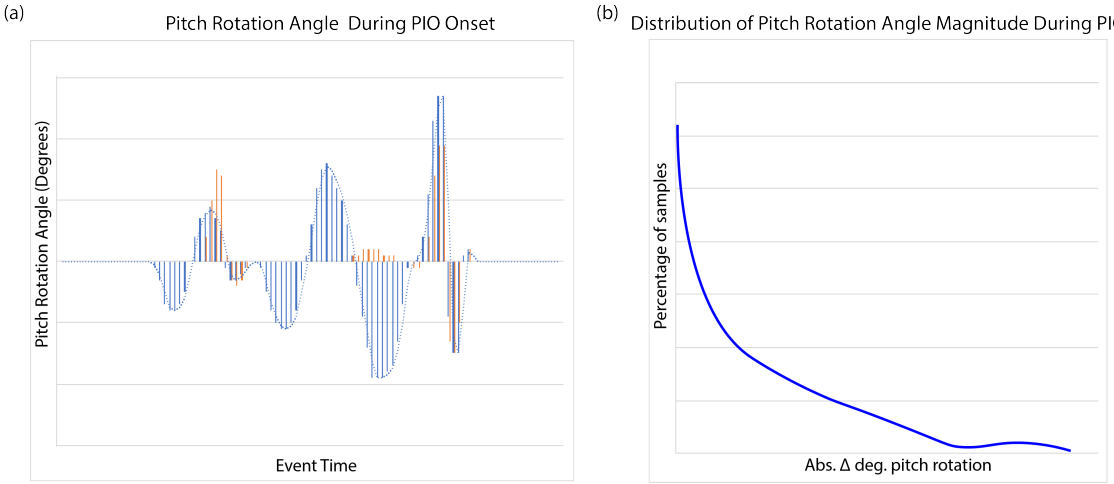

Figure 3.2: Illustration of pitch angle changes during PIO event.

In the 1-second interval before the pitch and roll oscillations reach a discernable

level, the stable oscillation of these control parameters are in the sub-degree range. Then, over the next eight seconds, as the PIO develops, we see the rapid increase in rotational pitch angle changes, leading to a crash of the UAS during the eighth second of the PIO event. As illustrated in Figure 3.2 (b), the pitch angle changes during a PIO event follow a power law distribution. For over 90 percent of the flight duration, the yaw, pitch, and roll measurements vary by less than 2 deg / 100 ms with altitude changes less than 1 ft/s during straight, level flight, as derived from our data from Experiment 1. In Figure 3.3, we see two stable flight mode regimes as oscillations between 133 and 138 degrees of yaw and between 142 and 145 degrees of yaw before and after a PIO event, respectively. This data was captured during one of our experiments that will be discussed later. The first regime lasted for 20.6 seconds, and the second regime lasted for approximately 17 seconds. These two regimes are illustrative of a flight dynamics mode known as a Dutch Roll, which takes its name from similarity to a figure skating maneuver [6]. We can see the excursion from stable flight when the PIO develops, causing an abrupt regime change to the next stable fixed point. Prior to this sudden shift, the UAS was oscillating about a stable fixed point. After the shift, the UAS began oscillation about a new stable fixed point.

Our research has identified that at distances $\geq$25 feet, as present in our experiments, it is very difficult for a pilot to recognize these subtle oscillations in aircraft yaw, roll, and pitch until it is too late for the pilot to take actions to successfully mitigate these pathological behaviors. One capability of our AviatAR system is a display indicator to inform the pilot of oscillation frequency and magnitude in each of the 3 rotational DOFs of the vehicle.

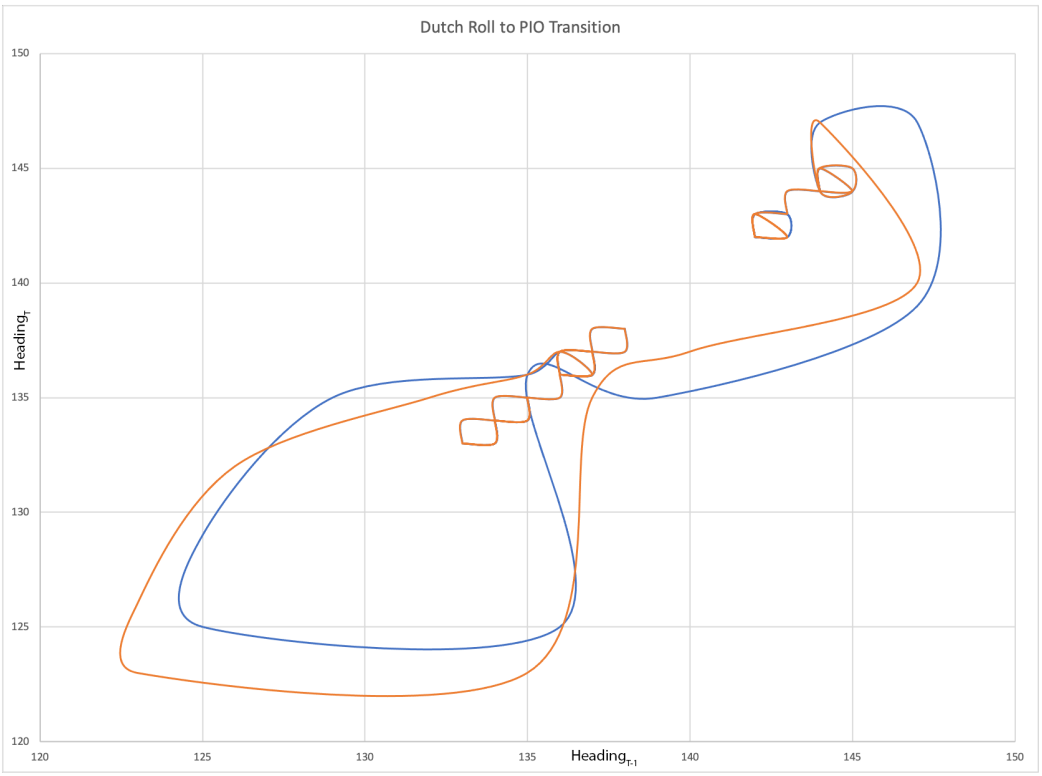

Figure 3.3: Lorenz map of Dutch roll to PIO transition during precision hover trial.

We use an angular measure known as *minute of angle* (MOA) to describe the effective field of view represented by one MOA (60 MOA = 1 degree of angle) from the perspective of the observer. At a distance of 100 yards, 1 MOA equates to an elevation of 1.047 inch. Figure 3.4 shows our UAS at a distance of 25 feet from the pilot. In this drawing, a vertical change of 1.047 inch is represented in vehicle altitude. Using the equation

$$1MOA = \frac{1.047in}{300ft} = \frac{y}{25ft} \tag{3.1}$$

we can determine the vertical distance for 1 MOA represented by solving for y

$$y_{25} = \frac{25ft}{1.047in * 300ft} = 0.0872in \tag{3.2}$$

showing that 1 MOA at a distance of 25 feet equates to a vertical distance of 0.0872

inches. To figure out how many MOA equates to our 1-inch change in UAS vertical position, we solve the equation

$$MOA_{25ft} = 1in/0.0872 \approx 11.468 \tag{3.3}$$

approximately an 11.468 MOA change in angular position of the UAS with respect to the pilot.

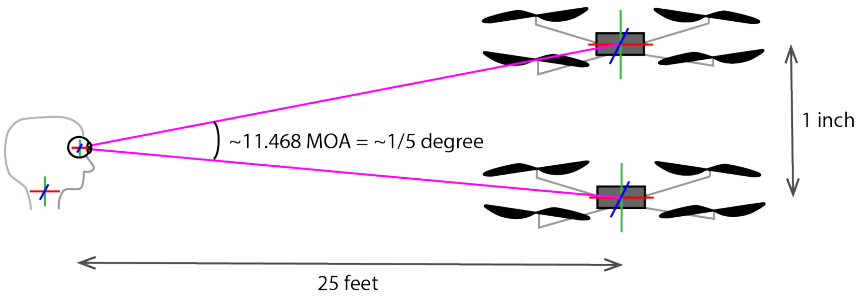

Figure 3.4: Illustration of pilot perception of UAS motion at a distance.

On the HoloLens 2 device, the accuracy of the eye-tracking function is estimated to be 1.5 to 3 degrees of the target. At our target range of 25 feet, we can use the value computed from Formula 3.2 to compute the vertical distance for 3 degrees as

$$y_{3deg@25ft} = 3deg * \frac{60MOA}{1DOA} * 0.0872in = 15.7050in \tag{3.4}$$

Figure 3.5 illustrates these bounds of certainty. A square, yellow box is drawn around a UAS in-flight at a distance of 25 feet from the pilot. If the pilot is focusing on the aircraft in flight, their eyes will principally gaze over the area inside of the box.

Because MOA calculations are proportional to the horizontal position of the observer, we can see that, at the farthest extent of our range (50 ft), 3 DOA at 50 ft doubles the vertical elevation found by Equation 3.2 to 31.41 inches vertical elevation. It can be readily inferred that, as the horizontal distance between the pilot and the UAS increases, the more certainty of the specific gaze target becomes.

Figure 3.5: Illustration of pilot visual certainty cone using Microsoft HoloLens 2 HMD at 25 feet from UAS.

Another challenge with using eye movements as a targeting mechanism is that they are very "noisy" because of the attention-seeking behavior of the visual system and saccadic eye movements. The eye primarily focuses on the position of the focus of current attention (e.g., the UAS on the course), but it will also move about to other positions other than the focus area (e.g., a nearby marker flag flapping in the breeze, the nearby hover target, etc.). Because of the sporadic nature of focus, it is best to think of sensed eye position data as having greater accuracy over longer time periods but low accuracy over shorter time periods.

3.2 System Components

A number of components are required in order to build the AviatAR platform. Even though we opted to use the Microsoft HoloLens 2 HMD that contains a rich selection of sensors and cameras, we had to implement a mechanism to capture both the pilot

and UAS positional information in a very accurate manner. As this data is collected in real-time, it is sent to a centralized computer for processing and inclusion into our map of the environment. Finally, this updated data is made available to the HMD via a web service to plot the current position and attitude of the UAS in the HoloLens environment, along with information to assist the pilot with decision-making during the mission.

3.2.1 PIO Detection Neural Network

One key component of our system is a deep neural network that detects the presence of oscillations that fit the pattern of PIO onset. This network consistently evaluates a sliding window of the last 20 samples of telemetry data to identify frequency patterns associated with PIO development and classifies this data into three categories as defined by the frequency spectra of the vehicle motion. The architecture of this detector network is shown in Figure 3.6.

Our network design takes inspiration from the network used by Zhu et al. to detect and identify P-waves in seismic analysis [90]. Our network takes a 20-sample sliding window of inputs for aileron and rudder inputs from the pilot controls along with the actual roll and yaw attitude values for the UAS and processes 10 samples for each of these inputs through a short-time Fourier transform (STFT) to produce the frequency spectra for each of the last 10 iterations with a 1-step shift through the window. The frequency spectra produced by each STFT computation is fed into a rectified linear unit (ReLU) layer for each 10-sample unit of data. Each ReLU output is then fed into a long short-term memory (LSTM) layer with the forget gate of the next LSTM unit connected to the output gate of the previous LSTM unit. The output of each LSTM layer is fed into a second LSTM layer for each sample window, the output of which is connected to the forget gate of the next layer's second LSTM layer. This feed-forward continues through each of the 10 parallel sampling units to identify frequency shift patterns over time to enable accurate classification of PIO intensity and shifts in the

pattern. The output of the second LSTM in the tenth sampling unit is then fed into a ReLU layer trained to produce an aggregate frequency spectrum quantity that is fed into a softmax layer to label the current UAS operating state as either a low, medium, or high intensity value for PIO presence.

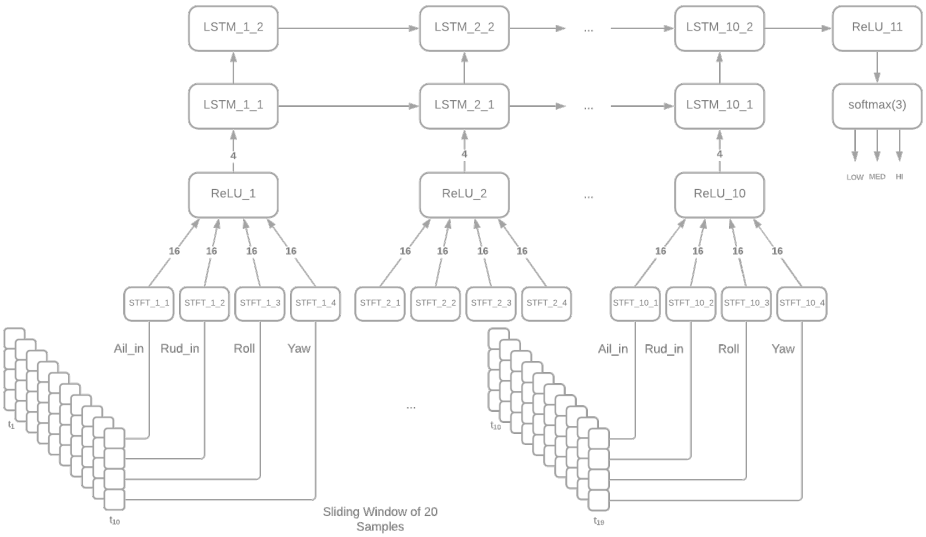

Figure 3.6: Architecture of deep neural network for PIO detection.

3.2.2 Operator and UAS Position Detection

To acquire the most accurate position possible of both the pilot and UAS in real-time, we equipped both the UAS and the HMD with a u-blox AG (Thalwil, CH) C099-F9P application board, shown in Figure 3.7. The C099 module contains two separate system-on-chip (SoC) modules: an ODIN-W2 wireless communications processor, and a ZED-F9P high-accuracy GNSS/RTK module. The ODIN wireless communications process provides both 2.4/5 GHz WiFi network capabilities as well as Bluetooth network connectivity for the C099 board. The ZED-F9P module receives global navigational satellite system (GNSS) information from the GPS, GLONASS, BeiDou, and other navigational satellite systems. By using two C099 modules mounted to the HMD and the UAS, we are able to use the *real-time kinematics* (RTK) capabilities of the u-blox ZED-F9P module to employ *differential GNSS* (DGNSS), a method

that uses two or more GNSS receivers to compute the current positions of the UAS as well as the operator at better than 2 cm positional accuracy at the ranges used in our experiments. The *base* C099 module installed in the HMD and the *rover* module installed on the UAS communicate over a dedicated 2.4 MHz WiFi network to exchange differential correction messages using a protocol defined the Radio Technical Commission for Maritime Services (RTCM) under the reference RTCM 10403.1 Issue 3.1.

To enable the HoloLens application with information from the UAS, we added an Intel Corporation (Santa Clara, CA) RealSense T265 tracking camera along with a RealSense D435 depth camera to the vehicle. Shown in Figure 3.9, the T265 contains two monochrome fish-eye cameras that provide a 170 degree field of vision (FOV), an inertial measurement unit (IMU) consisting of a 3-axis accelerometer and a 3-axis gyroscope to track rotation and acceleration of the vehicle at 6 DOF at 200 Hz sampling rate, as well as an Intel Movidius Myriad visual processing unit (VPU) that runs the visual inertial odometry simultaneous location and mapping (V-SLAM) algorithms on the camera. The D435 adds an additional RGB camera along with an additional active infrared depth camera with an 86 x 57 degree FOV at a resolution of 1280 x 720 pixels and a frame rate of up to 90 frames per second (FPS). This second camera provides an RGB sensor for our OpenCV programs as well as additional resolution for closer-range imaging to create a more defined point cloud image of the area that UAS is facing.

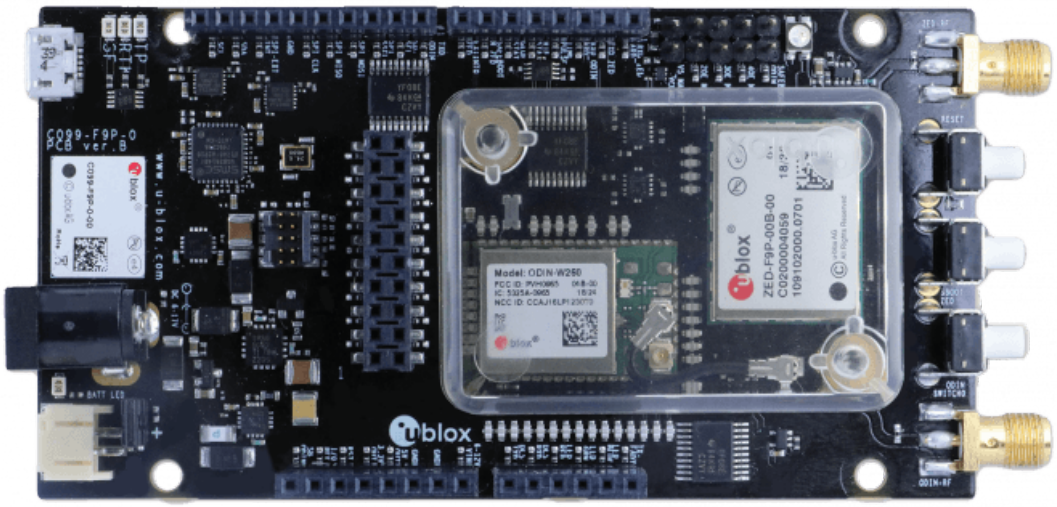

Figure 3.7: Image of u-blox C099-F9P GNSS/RTK module.

3.2.3 UAS Implementation

The Sys/ML block definition diagram (BDD) for the UAS implementation components is shown in Figure 3.8. The T265 and the D435 cameras are connected to an NVIDIA Corporation (Santa Clara, CA) Jetson Nano (Figure 3.10) computer using USB 3.1 interfaces. The Nano has a 4-core ARM processor equipped with a 128-core NVIDIA Maxwell GPU and runs the Ubuntu 18.04 LTS operating system along with custom software developed by our team in C++ to process the images and the data from the RealSense cameras to integrate with navigational data from the C099 module. The rover C099 module is connected to the Nano using the universal asynchronous receiver / transmitter (UART) on each board. Every 50 ms, as determined by the GPS clock on the C099 module, these values are posted to an Apache Kafka topic on the FSVM server.

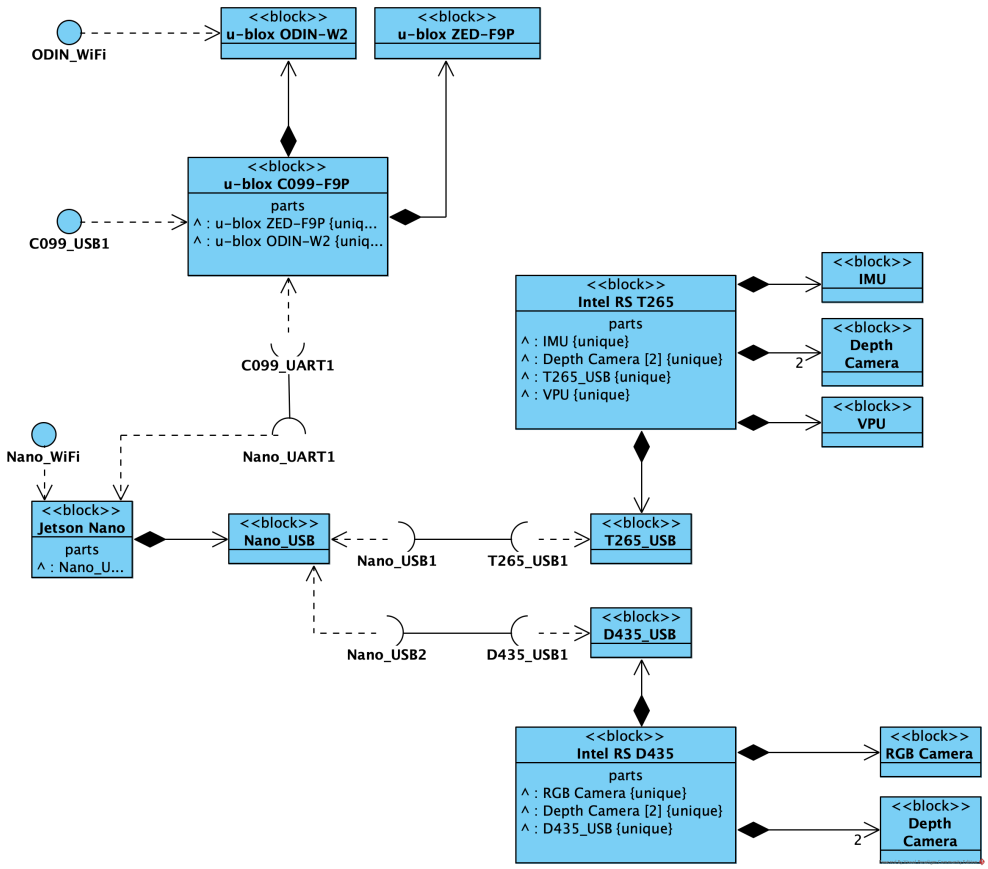

Figure 3.8: Sys/ML block diagram of UAS system components.

Figure 3.9: Image of Intel RealSense T265 tracking camera module mounted with D435 depth camera.

Figure 3.10: Image of NVIDIA Jetson Nano module.

3.2.4 HMD Implementation

The primary user interface for this system is based on the Microsoft HoloLens 2 mixed reality device. The HoloLens device contains a multi-core ARM64 processor with 4GB of RAM and runs the Microsoft Windows Holographic Operating System. Microsoft provides application programming interfaces (APIs) to access all of the sensors on the HoloLens 2 device, including cameras, microphones eye- and gaze-tracking cameras, as well as the gyroscope, accelerometer, and magnetometer. Figure 3.11 shows the Sys/ML BDD for the HMD system.

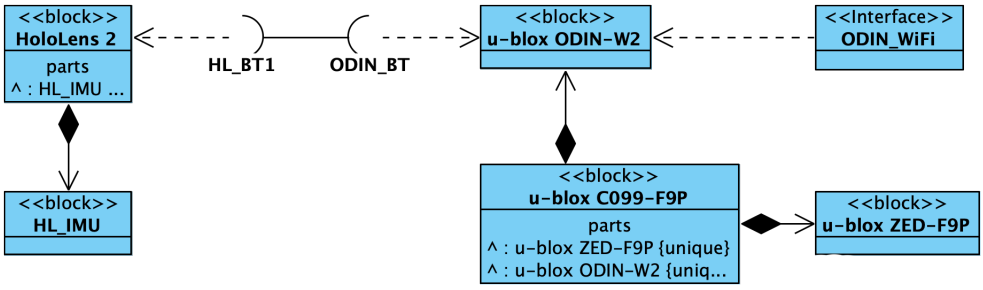

Figure 3.11: Sys/ML block definition diagram of HMD system components.

Since the HoloLens is intended for indoor-use only, it is not equipped with a GPS

sensor. Similar to the UAS implementation, we attached a u-blox C099-F9P module to the HoloLens device to function as the base unit for the RTK capability. The base u-blox C099-F9P module is paired with the HMD using one of the five Bluetooth radio channels on the HoloLens. For simplicity, we attached the C099 module and its antennas to the head strap on top of the HoloLens using zip ties. This ensures that the GNSS antenna location was centered on the pilot's location at all times.

The Microsoft HoloLens 2 device does not typically provide direct access to all of the cameras and sensors on the headset. To access these sensors, a special "research mode" must be enabled on the device to directly access the IMU, eye-tracking sensors, depth-tracking camera data, and microphones [91]. Once this mode is enabled and the user consents to this additional level of data collection, HoloLens 2 applications can access these additional features.

When research mode is enabled on the HoloLens 2, we have access to all of the sensor streams on the HMD. Data from these sensor streams are activated by invoking `OpenStream`, and data from each stream is retrieved using the `GetNextBuffer` method. `GetNextBuffer` is a blocking method, so individual threads are used for each of the gyroscope, accelerometer, and magnetometer sensors on the device. We also used one thread to communicate with the C099 module.

3.3 The Flight-space Volume Model

At the heart of the application is the *flight-space volume model* (FSVM), which is a real-time representation of the three-dimensional conversation between the pilot and the UAS being piloted. The FSVM is hosted on an Ubuntu Linux 18.04 instance on a Dell (Round Rock, TX) Inspiron G7 laptop equipped with 32 GB RAM, 1 TB SSD hard drive, an Intel i7-9750H CPU with 6 cores at 2.60 GHz, and an NVIDIA GeForce RTX 2060 GPU with 1920 CUDA cores at 0.96 GHz and 6144 MB GPU RAM. In addition to the Linux OS, the FSVM server includes an Apache Kafka 2.6.0 instance to receive telemetry and position updates from both the UAS and the HMD systems.

The FSVM is built using proprietary C++ modules to implement our graph-oriented environment map.

At the beginning of a flight sequence, the initial FSVM consists of the polygon bounded by the quaternion that represents the position and height of the base C099 sensor located on the HMD and the quaternion representing the location of the rover C099 sensor located on the UAS, typically on a level flat surface some distance away from the pilot, along with some small but non-zero radius about this line between the two points. If the pilot moves their head about the space, say to look at their feet, the FSVM can be expanded using information returned by the short- and long-throw cameras located on the HoloLens. The newly-expanded FSVM representation may look like the representation in Figure 3.13. As the pilot and the UAS navigate the space, the volume is expanded to contain the new voxels of data, which include both the position and trajectory information of the pilot and UAS at various times. The FSVM serves as both a history of the flight from both the pilot and vehicle perspective as well as the current state of the pilot-UAS interaction. An illustration of the FSVM concept is shown in Figure 3.12.

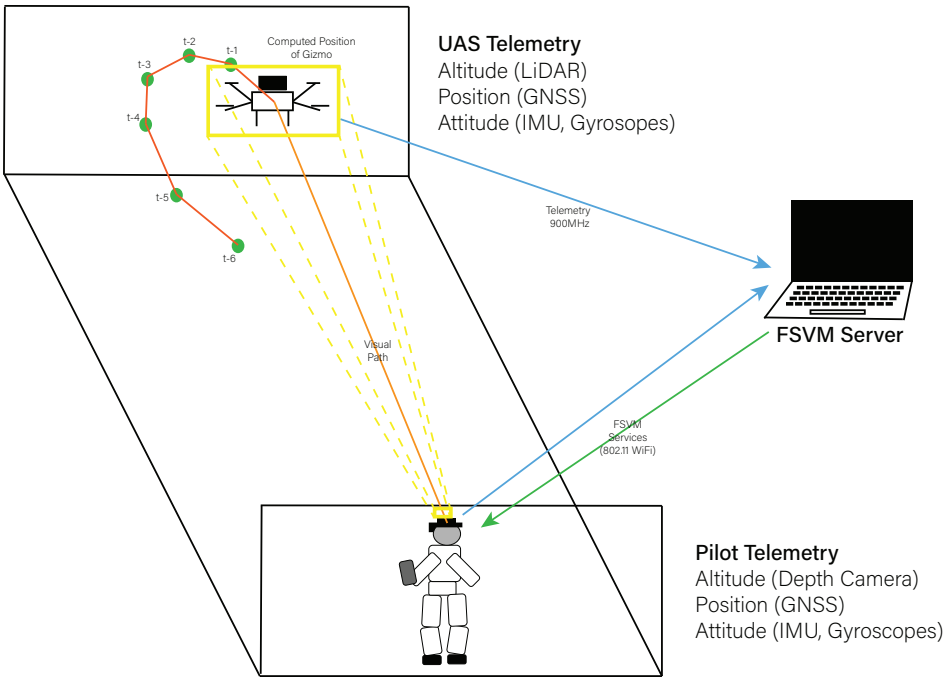

Figure 3.12: Flight-space volume model concept illustration.

Construction of the FSVM map must be done from the perspective of the pilot as well as from the UAS to ensure proper initialization of the computational systems on each station. To achieve this, we placed 30 mm x 30 mm RSZ4 reflective targets from Rothbucher Systeme (Bad Reichenhall, DE) at the base and the center of each of the seven positions located on the course shown in Figure 3.13 (a). We also placed additional targets on the center of the UAS from the front-facing side as well as the center of the base module on top of the pilot HMD. An example of this marker is shown in Figure 3.14.

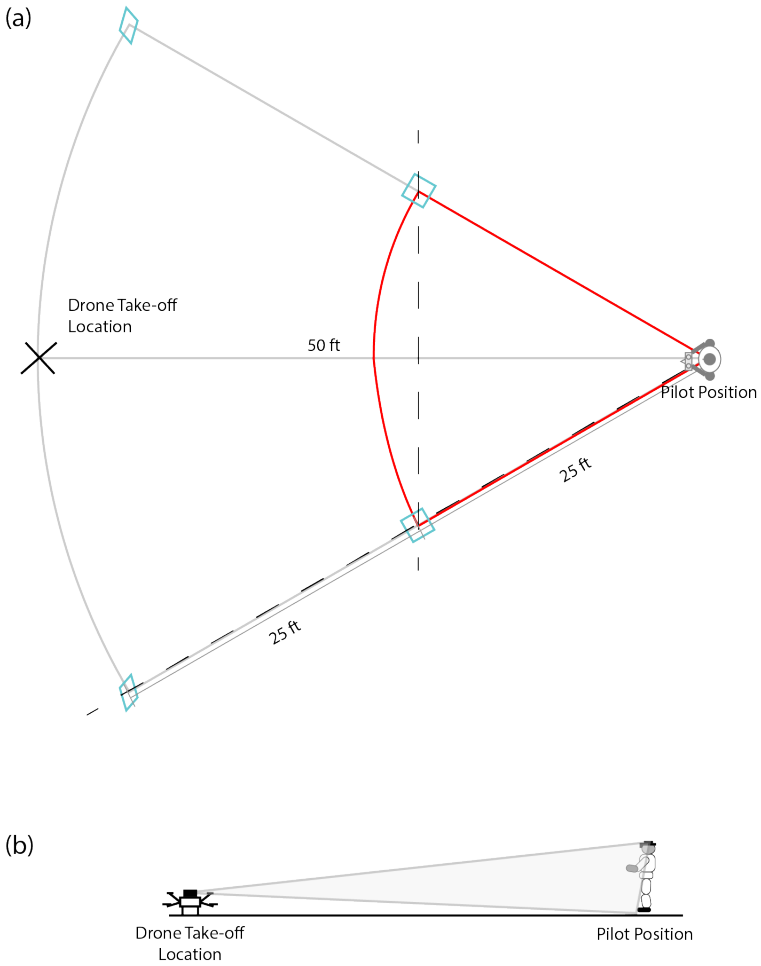

Figure 3.13: Initial example flight-space volume model.

Figure 3.14: Rothbucher Systeme RSZ3 30 mm x 30 mm reflective target.

3.3.1 Pre-flight Calibration

Prior to flight, the FSVM must be calibrated to identify the relative position of the UAS to the pilot position as well as to the rest of the target positions on the course. To accomplish this, a calibration process must be executed on both the UAS FCS as well as on the AviatAR HMD to identify the relative positions and angles of the UAS and the pilot with respect to these benchmark locations on the course. This will establish the initialized FSVM space.

3.3.2 Position Capture

To compute the tracking information for the UAS to be displayed on the HMD, we must first capture the full position of the pilot's head as well as the full position of the UAS. Since these programs run on two different platforms and have to capture data from both the IMU on each device as well as data from the C099 module and then integrate these together to produce the current state of the FSVM, we will address each separately.

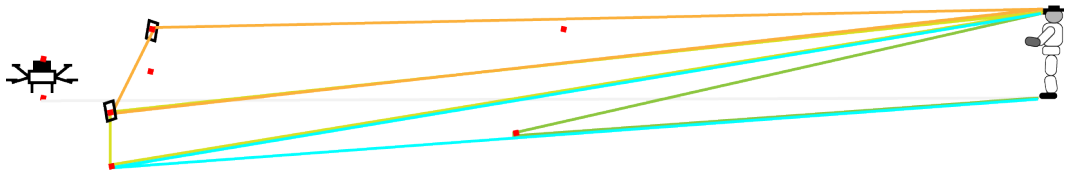

Figure 3.15: Representation of FSVM model during initialization.

3.3.2.1 UAS Position Capture

The high-level method to capture the information from the IMU on the T265 camera is shown in Algorithm 1. We first create an instance of the `rs2::pipeline` class to process data streams from the camera. For our purposes, we are interested in the `RS2_STREAM_ACCEL` and `RS2_STREAM_GYRO` streams, so we enable those using the `rs2::config.enable_stream` method. Now we set up a loop on the Nano process to read the accelerometer and gyroscope frames from each stream using the `rs2::frameset.first` method to get the next frame from each stream. We

then use this data to create instances of `rs2::motion_frame` objects for each frame of each type (accelerometer and gyroscope).

Since we have two separate sets of motion date from the IMU - the gyroscope vectors that tell us the current rate of roll, pitch, and yaw as well as the accelerometer vectors that tell us the current amount of roll, pitch, and yaw - we have to integrate each of these elements into every new calculated roll, pitch, and yaw value computed from the IMU data. For the gyroscope data, this is accomplished using the equations:

$$roll = roll + dR_{roll_{gyro}}dt \tag{3.5}$$

$$pitch = pitch - dR_{pitch_{gyro}}dt \tag{3.6}$$

$$yaw = yaw + dR_{yaw_{gyro}}dt \tag{3.7}$$

The equations labeled as 3.5, 3.6, and 3.7 represent the portion of Algorithm 1 identified as `processGyroscopeFrame`.

Each of the values from the gyroscope data provides a rate of roll, pitch, and yaw in radians per second. To convert this data into an angular displacement, we take the amount of time between the last two measurements to compute the value of dt, and multiply this by the rate of change in radians per second dR for each measurement. In the case of roll and yaw, we add it to the prior value of each to accumulate the new value of each as shown in Equations 3.5 and 3.7. In the case of pitch shown in Equation 3.6, we subtract the value from the current value of pitch since, in our convention, positive measures of the roll are indicated to the right and negative to the left, which is inverse to how a pilot would think of the forward or backward pitch of an aircraft.

To use the accelerometer data, we must first calculate the resultant normal vector that represents to pull of gravity against the accelerometer. This is done using the

Pythagorean theorem

$$R = \sqrt{x_{accel}^2 + y_{accel}^2 + z_{accel}^2} \tag{3.8}$$

where the values for x_{accel}, y_{accel}, and z_{accel} are read from the accelerometer frame motion data. With this value for R, we can now compute the new values for roll, yaw, and pitch from the accelerometer motion frame data as

$$roll_{accel} = acos(x_{accel}/R) \tag{3.9}$$

$$yaw_{accel} = acos(y_{accel}/R) \tag{3.10}$$

$$pitch_{accel} = acos(z_{accel}/R) \tag{3.11}$$

Equations 3.8, 3.9, 3.10, and 3.11 represent the portion of Algorithm 1 identified as `processAccelerometerFrame`.

When combining data for each of the rotational angles from the gyroscope and the accelerometer, we need to consider the sampling frequency of each device. A gyroscope is a high-frequency device, able to deliver an accurate measure of the rotational rate of change on each axis, whereas an accelerometer provides a much noisier signal that includes many different signals along with the changes in kinematics of the UAS. As such, averaging the accelerometer signals over a much longer time provides a better drift compensation offset for the gyroscope data, effectively acting as a low-pass filter for the accelerometer data. This is commonly implemented in embedded systems as a *complementary filter* to apply a higher proportion of the high-frequency sample from the gyroscope along with the complementary amount of the low-frequency sample from the accelerometer to the updated roll, yaw, and pitch estimates in each cycle [92, 93]. This has become the recommended practice in the use of motion and positional data in mobile devices, pedometers, and robots because of the low computational demand and complexity, as opposed to more computationally-

heavy mechanisms such as the Kalman filter [94]. The complementary filter equations are

$$roll = roll * C_{gyro} + roll_{accel} * C_{accel} \tag{3.12}$$

$$pitch = pitch * C_{gyro} + pitch_{accel} * C_{accel} \tag{3.13}$$

$$yaw = yaw * C_{gyro} + yaw_{accel} * C_{accel} \tag{3.14}$$

In our program to process IMU frames from the RealSense T265 camera, we set the constants C_{gyro} and C_{accel} to 0.98 and 0.02, respectively. These are arbitrary percentages used for a variety of gyroscope / accelerometer hardware but should be validated for any particular application.

Algorithm 1: Algorithm to capture frames from T265 IMU to compute yaw/pitch/roll

```
/* mix coefficients for complementary filter                    */
/* these constants must sum to 1.0                              */
C_ACCEL ⟵ 0.02;
C_GYRO ⟵ 0.98;
yaw ← pitch ← roll ← 0.0;
pl ← new Pipeline();
pl.enableAccelerometerStream();
pl.enableGyroscopeStream();
while active do
    frames ← pl.pollFrames();
    for f in frames do
        accel ← f.getAccelerometerFrame();
        gyro ← f.getGyroscopeFrame();
        tstamp ← f.getFrameTimestamp();
        dt ← tstamp − last_tstamp;
        last_tstamp ← tstamp;
    end
    (roll_g, pitch_g, yaw_g) ← processGyroscopeFrame(gyro);
    (roll_a, pitch_a, yaw_a) ← processAccelerometerFrame(accel);
    /* integrate using a complementary filter                   */
    roll ← (roll_g * dt) * C_GYRO + roll_a * C_ACCEL;
    pitch ← (pitch_g * dt) * C_GYRO + pitch_a * C_ACCEL;
    roll ← (yaw_g * dt) * C_GYRO + yaw_a * C_ACCEL;
end
```

3.3.2.2 HMD Position Capture

The HMD sits just in front of the forehead of the pilot and is attached using a latitudinal band that rests just above the ears and attaches to the computer pack on the back of the head. An additional strap connects longitudinally from the goggles to the computer pack and runs centrally over the top of the head. The latitudinal band is adjustable for fit to hold the goggles steadily in place, effectively fixing their position to the pilot's forehead.

In Figure 3.16, we see a representation of a pilot's head. At the location of the neck, we have a collection of angles that represent the three angles of rotation of the human neck: the rotation from the resting front horizontal position of the head as it rotates upward or downward, θ_n; the side-to-side rotation of the head about the z-axis, ψ_n; and the side-to-side rotation about the x-axis, φ_n. Similarly, the HMD has a set of rotational angles θ_h, ψ_h, and φ_h that represent the same motions as the neck counterparts. Since the HMD is fixed in position to this pilot's forehead and the human skull is a rigid body, any change in the neck rotational angles corresponds to the same change in angles of the HMD. As the neck rotational angles change, the translation in position of the HMD in space changes as a function of the distance from the point of neck rotation to the center of the HMD on the pilot's forehead. For example, if the distance from the neck "joint" to the HMD position is 6 inches, a change of 2 DOA (120 MOA) in θ_n at the neck will translate to a 2 DOA change in θ_h but will result in a translational change in HMD position according to the equation

$$\Delta y_{1MOA@6in} = \frac{6in}{1.047in * 300ft} = 0.0016in \tag{3.15}$$

and, accordingly, 120 MOA equates to

$$\Delta y_h = 120MOA * 0.0016in = 0.191in \tag{3.16}$$

resulting in an approximately 0.2 in rise in HMD position from a positive 2 degree change in neck angle position φ along the y-axis.

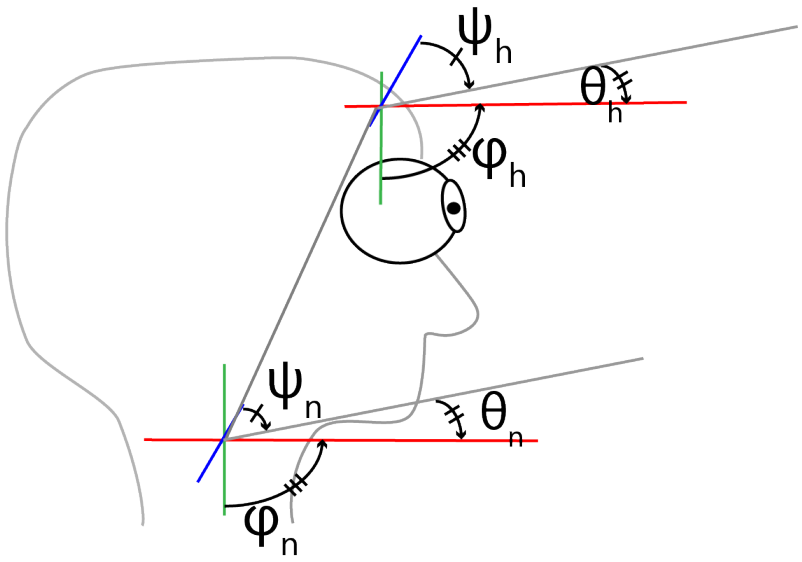

Figure 3.16: Illustration of the relationship between neck angles n and IMU angles h of the HMD.

Similar to the conditioning of gyroscope and accelerometer data captured from the T265 camera, we applied the logic Algorithm 1 to implement the complementary filter for the HoloLens device, with some additional components. The IMU of the HoloLens 2 device contains both a 3-axis accelerometer and 3-axis gyroscope as found in the T265 IMU; however, the HoloLens 2 IMU also includes a 3-axis magnetometer to measure the actual heading . A magnetometer is similar in nature to a gyroscope, in that it measures changes in magnetic fields along each axis to determine the rate of change of rotation, $\frac{dR}{dt}$ in each axis over time. This change is then used to compute the current position about each axis. Since the magnetometer is similar to the gyroscope in its stability, we changed the coefficient used by the complementary filter for C_{gyro} to 0.49 and added an additional coefficient, C_{mag}, and set its value to 0.49 to treat its input equal to the gyroscope data in the computation.

3.4 User Interface

A central component of the AviatAR system is the AR user interface. This user interface is projected onto the HoloLens display by a Unity Pro application using information from the HMD sensors as well as from the FSVM web services.

3.4.0.1 Position Interpolation from Sensor Data

In Section 3.3.2 above, we discussed how GNSS position data and IMU pose data are acquired from both the HMD and the UAS. Once this data is sent to the Kafka queues on the FSVM server, the Tait-Bryan angles for each object's position vectors are computed and the resultant vector calculated from this information. This provides the display position for the UAS bounding box to be computed, along with the size of the collision space for the UAS using a 3 degree of angle accuracy estimate for eye tracking by the HoloLens device with respect to the pilot's visual field.

3.4.1 The Unity Game Environment

In the Unity game development system, the user environment of a game is referred to as a scene. For our project, we use a single scene to represent the world view that the pilot interacts with during a flight. Unity uses a generic object class called a GameObject to represent items within the game environment. GameObjects are components that can be manipulated and interacted with by the player or the environment. In our base scene that represents our training course, we have multiple GameObjects:

- `HoverBoard`, represents the two 3x4 targets centered at 5 feet above ground, 50 feet from the pilot
- `HoverTarget`, represents the two 3x4 targets on the ground placed 25 feet from the pilot and center-aligned with the path to the HoverBoards
- `UasBox`, represents the UAS as it transits the course

Each of these GameObjects has a Unity component called a Box Collider associated with it. These Box Colliders enable the AviatAR UI to provide feedback to the pilot during flight by visual cues. An example of these cues are seen in Figure 3.17. In this figure, we see the pilot's view through the 54 degree diagonal field of view of the HoloLens 2 HMD. the UasBox object is seen around the UAS in-flight, scaled for the 3 DOA relative height and width at the distance from the pilot. Centered within this box is a set of three lines that represent the relative x-, y-, and z-axes through the center of the UAS, with lengths and directions of each line representing the current orientation of the UAS in space. A long green line represents the normal vector from the center of the UAS to the approximate level of the ground, at which point extends a circle roughly the diameter of the UAS. This enables the pilot to more easily identify the area under the vehicle to help gauge navigation of the UAS over a specific target area.

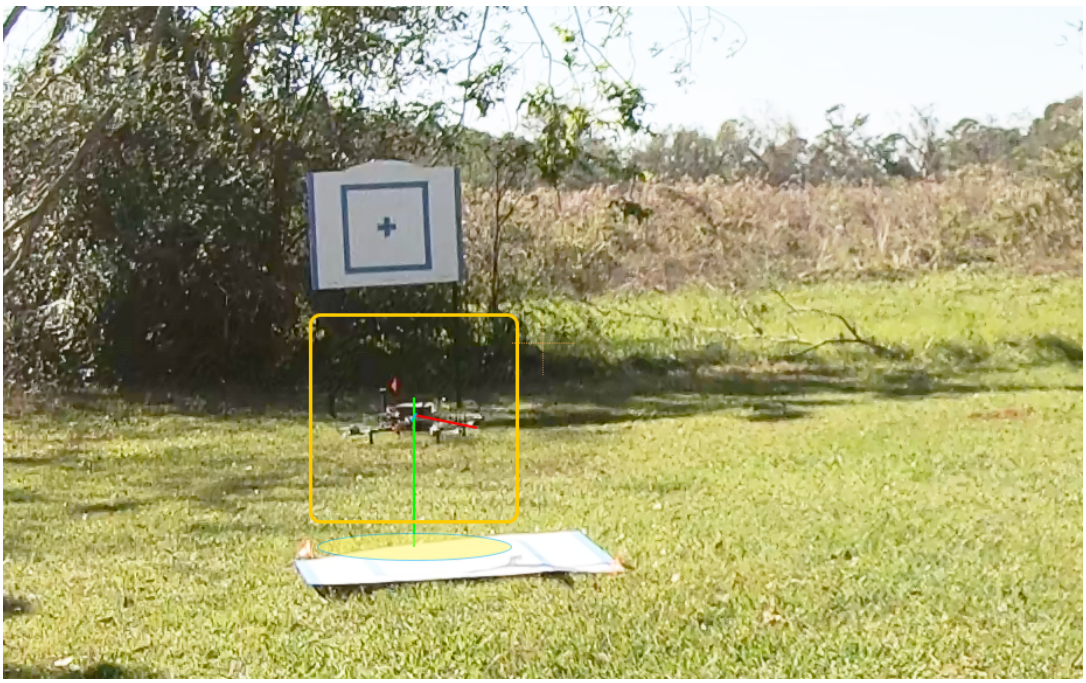

Figure 3.17: AviatAR UI example view during flight.

Each object in Unity has an associated set of transforms. These transforms enable us to pragmatically set the position, rotation, and scale of the object in three-

dimensional space. This is a necessary functionality to move the set of components associated with the UasBox object as the UAS position on the course changes.

The AviatAR application gets the information to accomplish object transform adjustment from a web services application programming interface (API) provided by FSVM. This API provides a collection of services that are invoked from the Unity application during the initialization sequence as well as during flight operations. To initialize the positional information for each transform, FSVM provides a method, `setxxxInitialPosition`, that updates FSVM with initial data from the C099 modules to set the positional coordinates as well as establishes the magnetic bearings for each device. The `xxx` is replaced with `Uas` or `Hmd` depending on where we are working with the UAS or HMD, respectively. These values are used to offset the local rotational device values provided natively for the IMUs.

On initialization of our control sequence, we assume that the UAS is sitting in the center of its launch box, with the front of the vehicle facing the pilot box. In the `World` coordinate system (WCS) of the scene, the Euler angles associated with the pilot rotational position are (0,0,0) and the angles for the UAS rotational position are (0,180,0). These are relative positions used in the Unity system and must be adjusted by the actual magnetic positions of each location. The factors used for this adjustment are computed during the initialization routine.

To initialize the UAS system, we added a red and green LED circuit attached to pins 12 and 18 of the header on the Nano. We also attached a normally-open single-pole single-throw (SPST) push-button circuit to pin 22 of the header. Once the UAS is placed on the take-off box, pressing the push-button invokes the `initUasIMU` program on the Nano. This program uses OpenCV to acquire images from the RGB camera on the D435 camera module and use the OpenCV `cv::MatOp::roi` method to crop the image to a 64 x 128 pixel region from the center of the image. This strip of the original image represents the direct view from the center of the camera on

the front of the UAS and is passed to a convolutional neural network (CNN) model that has been trained on images of the RSZ3 reflective target shown in Figure 3.14. The architecture of this CNN is shown in Figure 3.18. The red LED on the Nano blinks until the model returns an output $\geq$0.85 indicating high likelihood that it has located the marker in the center of the image. This blinking indicates to the person performing the calibration the UAS that continued adjustment of the UAS' position on the pad must continue. Once the model identifies that the marker has been found in the proper zone, the red LED stops flashing, the green LED turns steadily on, the initialization program sends the GNSS position and IMU values to the FSVM using the `setUasInitialPosition` API method, and the UAS initialization routine exits.

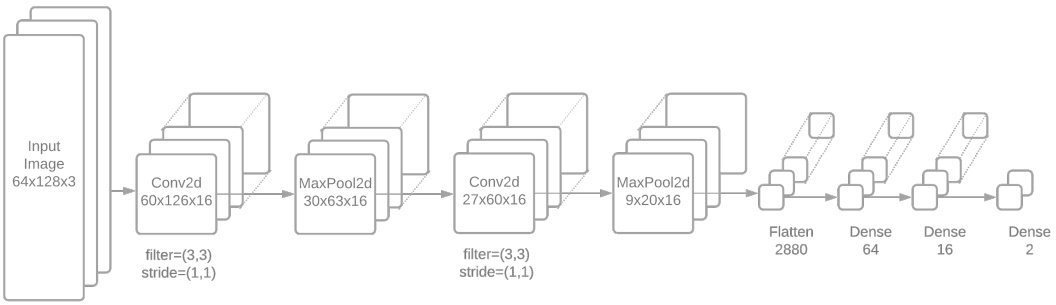

Figure 3.18: Architecture of convolutional neural network used to detect targets in `initUasIMU` program.

After UAS calibration is complete, we then perform the HMD calibration. To do this, the HMD user launches the `initHmdIMU` application from the HoloLens. This opens a Unity application on the device and prompts the user to place markers on the UAS takeoff position as well as the hover targets and the hover pad. This placement is done using a Bluetooth-enabled Microsoft XBox game controller that is paired with the HoloLens 2 device. As the user places each target, the eye-tracking and head pose information of the user during these activities is captured for later use. After these targets are placed, the transform data for each GameObject is sent to the FSVM

using the `setHmdInitialPosition` API method and the program ends.

A call to the `getCurrentPosition` method returns a JSON structure with the structure shown in Listing 3.1. The JSON payload from this operation returns 8 values. The first three values represent the position of the UAS in space as centimeters. The `x_pos` element is the distance to the left (negative) or the right (positive) of the pilot position. `z_pos` value represents the distance from the pilot position, with negative values representing a point behind the pilot box relative to the initial point of the UAS at takeoff. The `y_pos` value represents the vertical position of the UAS AGL; this value could be negative if the current altitude of the UAS is less than the altitude of the takeoff position, such as in the case where the initial takeoff occurred on the peak of a hill. The next three values relate to the attitude of the UAS in space, as measured in degrees. The `pitch` and `roll` values have a range of -180 to 180 degrees, while the `yaw` value has a range of 0 to 360 degrees. The final two values, `lat` and `lon` represent the coordinates of the UAS on the surface of the Earth down to ±2 cm accuracy, which we are able to resolve because of the precision of DGNSS with RTK.

Listing 3.1: JSON payload response for `getCurrentPosition` method.

```
1  {
2      "getCurrentPosition_response" : {
3      "pilot_position" : {
4          "x_pos" : 914.40,
5          "y_pos" " 3168,
6          "z_pos" : 7620,
7          "pitch" : -12.3,
8          "roll"  : 2.7,
9          "yaw"   : 157.2,
10         "lat"   : 30.5887554,
```

```
11          "lon"    : -87.8726997
12      },
13      "uas_position" : {
14          "x_pos" : 914.40,
15          "y_pos" " 3168,
16          "z_pos" : 7620,
17          "pitch" : -12.3,
18          "roll"  : 2.7,
19          "yaw"   : 157.2,
20          "lat"   : 30.5887554,
21          "lon"   : -87.8726997
22      }
23  }
```

3.4.2 UAS Location Rendering within HMD Visual Space

To enable integration of the features of the Microsoft HoloLens 2 with the Unity environment, we import the Microsoft mixed-reality toolkit (MRTK) objects into our Unity game project. This loads the libraries into the Unity environment so that all of the necessary code is included when the C# code is generated during an application build to access the HoloLens sensors. In many cases, the MRTK scripts adapt the hand, eye, and head movement sensors to the standard actions of a joystick controller. Unity natively supports voice inputs, so the microphones on the HoloLens 2 directly support this capability.

To correctly render the position of the UAS in the Unity environment, we need to know the distance from the pilot to the vehicle. This path over the surface of a spheroid is known as a *geodesic*. Since we are computing this distance between the UAS and the pilot using their latitudes and longitudes with centimeter-accuracy

thanks to DGNSS, we have the necessary inputs for this calculation.

When high-precision is not a requirement, we will typically use the *haversine* formula to compute the length of the geodesic s between two points. The haversine formula can be stated by the equation

$$s = 2r \cdot arcsin(\sqrt{sin^2(\frac{\varphi_2 - \varphi_1}{2}) + cos(\varphi_1)cos(\varphi_2)sin^2(\frac{\lambda_2 - \lambda_1}{2})}) \tag{3.17}$$

where r is the radius of the sphere, and (φ_1, λ_1) and (φ_2, λ_2) are the latitude and longitude of the two points between which we are calculating the geodesic s. For our specific situation, we can make this calculation more accurate by calculating the specific radius of the Earth at our location and adding the height above sea level. Since we are only operating over a very small area, the error from the haversine assumption of the spherical shape of the Earth would be negligible. In order to make our solution more general, however, we have elected to pursue an approach that treats the Earth as an oblate spheroid.

There are several methods available to compute short geodesic length with distances less than 500 kilometers, such as the Bowring formulae, the Gauss mid-latitude formulae, and others [95]. One challenge with these methods is that the accuracy of the solution is variable depending upon the latitudes over which the measurements are taken as well as the length of the geodesic being measured. In 1975, Vincenty devised a set of methods for computing long geodesics capable of reaching an arbitrary level of precision less than 1 mm [96]. The particular method of interest to us in Vincenty's method is the solution to what is referred to as the *inverse problem*, which has us compute the shortest geodesic between two points located anywhere on the planet. For the inverse problem, we must first compute the polar angle λ_{12} between the two meridians pass through each point to an appropriate level of accuracy. Once we have this angle, we can then compute the length of the side alternate to the polar angle that represents the length of the geodesic s.

Algorithm 2: Pseudocode for Vincenty's Algorithm for inverse solution - adapted from [96]

/* latitude and longitude values as inputs must be to */
/* seven decimal places to achieve 1cm accuracy */

Data: φ_1, λ_1, φ_2, λ_2 ; /* lat. and lon. of points 1 & 2 */

Result: s ; /* distance between points */

const $C_{precision} \leftarrow 0.00000001$; /* 10e-8 approx 1cm accuracy */

begin

$a \leftarrow 6378137.0$; /* len. of radius at equator (m) */

$f \leftarrow 1/298.257223563$; /* flattening of ellipsoid */

$b \leftarrow (1-f)a$; /* len. of radius at poles (m) */

$u_1 \leftarrow arctan((1-f)tan(\varphi_1))$;

$u_2 \leftarrow arctan((1-f)tan(\varphi_2))$;

$\Delta\lambda = L = \lambda_2 - \lambda_1$; /* set initial value of $\Delta\lambda$ to L */

repeat

$sin\sigma \leftarrow \sqrt{(cos(u_2)sin(\Delta\lambda))^2 + (cos(u_1)sin(u_2) - sin(u_1)cos(u_2)cos(\Delta\lambda))^2}$;

$cos\sigma \leftarrow sin(u_1)sin(u_2) + cos(u_1)cos(u_2)cos(\Delta\lambda)$;

$\sigma \leftarrow arctan2(sin\sigma, cos\sigma)$;

$sin\alpha \leftarrow (cos(u_1)cos(u_2)sin(\Delta\lambda))/sin\sigma$;

$cos2\sigma_m \leftarrow cos\sigma - (2sin(u_1)sin(u_2))/(1-sin^2(\alpha))$;

$C \leftarrow \frac{f}{16}cos^2(\alpha)[4 + f(4 - 3cos^2(\alpha))]$;

$\Delta\lambda \leftarrow L + (1-C)f(sin\alpha)\{\sigma + C(sin\sigma)[cos2\sigma_m + C(cos\sigma)(-1 + 2cos^2(2\sigma_m))]\}$

until $\Delta\lambda \leq C_{precision}$;

$u^2 \leftarrow cos^2(\alpha)[(a^2 - b^2)/b^2]$;

$A \leftarrow 1 + \frac{u^2}{16384}(4096 + u^2[-768 + u^2(320 - 175u^2)])$;

$B \leftarrow \frac{u^2}{1024}(256 + u^2[-128 + u^2(74 - 47u^2)])$;

$\Delta\sigma \leftarrow Bsin\sigma\{cos2\sigma_m + \frac{1}{4}B(cos\sigma[-1 + (2cos2\sigma_m)^2) - \frac{B}{6}cos2\sigma_m[-3 +$

$4(sin\sigma)^2][-3 + 4(cos2\sigma_m)^2])\}$;

$s \leftarrow bA(\sigma - \delta\sigma)$;

end

Vincenty's inverse method algorithm consists of two pieces: an iterative component that uses Newton's method to arrive at the value of the angle λ_{12}. To inform these calculations, data from the World Geodetic System 1984 (WGS-84) model of the Earth produced by the US National Geospatial Intelligence Agency is used [97]. Three pieces of data from this model are necessary to compute the curvatures between the two points and the pole included in the great circle route: the *flattening* constant that describes how the curvature changes between the equator and the pole; the radius of the Earth at the equator, known as the *semi-major axis*; and the radius of the Earth at the poles, known as the *semi-minor axis*.

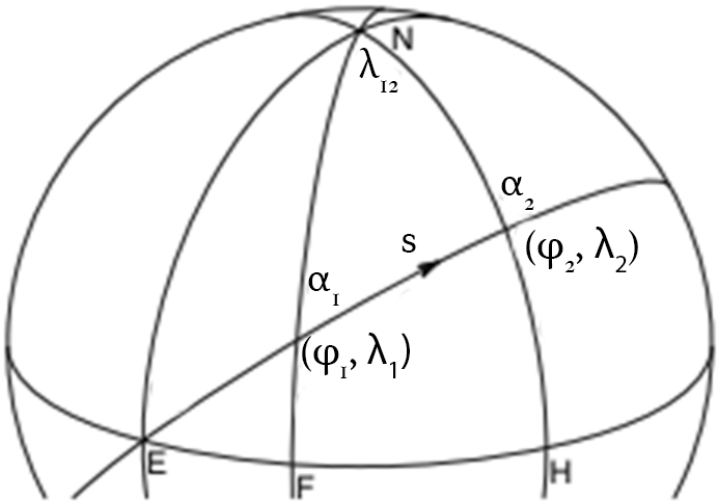

Figure 3.19: Illustration of using Vincenty's inverse method to compute the length of geodesic s for two points (φ_1, λ_1) and (φ_2, λ_2).

An illustration of this is shown in Figure 3.19. For our two points $A = (\varphi_1, \lambda_1)$ and $B = (\varphi_2, \lambda_2)$ which reside on meridians F and H respectively, we can calculate the azimuths α_1 and α_2 using the cosine of the flattening constant f to produce the radius of the Earth at each given point. Once we have these points in $\mathbb{R}_3$, we can than iteratively improve the value of λ_{12} to an appropriate level of accuracy. For the purpose of our model, we seek centimeter-level accuracy; Vincenty's method provides

a potential for up to 0.5 mm accuracy [96]. We can then use the values computed in the iterative section to compute the geodesic s.

By using the latitude and longitude pairs from our C099 modules on the HMD and the UAS, we can obtain the distance and from the pilot position to the UAS to at least 2 cm of accuracy using Vicenty's method from the previous section. This is used to set the position of the `UasBox` GameObject in the Unity application.

3.4.3 Visual Cue Rendering

Now that we are able to capture the position of the UAS relative to the pilot in real-time, along with the current pose of the UAS relative to the pilot, we can maintain the pilot's SA with this visual cue. In addition to this collection of information, we also want to provide the pilot with a low-complexity cue to aid in identification of oscillation onset and intensity. To keep the complexity low, we selected a simple line as an indicator of UAS oscillation and colored the line depending upon the principle frequency (ν) of oscillation: green for principal frequency spectrum $\nu \leq 10$ Hz, yellow for the presence of signal components $\nu > 10$ Hz with amplitudes > 2 but less than 5 in aggregate for all components > 10 Hz, and red for any condition exceeding yellow state. To test our theory that lower-complexity, high-information density cues improve pilot performance, we implemented the cues using three methods: attaching the visual cue to the `UasBox` object in the pilot's superior primary FOV; placing the cue in the superior peripheral FOV of the pilot's non-dominant eye; and placing the cue in the inferior peripheral FOV of the pilot's non-dominant eye.

3.4.3.1 Superior Primary FOV-located Cue

For Survey 2 Evolution 2, we attached a simple cue to the top of the `UasBox` GameObject in our Unity scene. By placing the cue in this position, we ensure that the cue remains in the superior primary FOV for both eyes, as the pilot's attention is principally focused on the UAS during flight. The pilot sees the cue through the

right-upper quadrant of the left eye and the left-upper quadrant of the right eye when looking at the UAS. With the cue in this position in each eye, the cue image is processed by each eye through the optic chiasma, the LGN on the same side as the eye, through the Meyer's loop, and finally by the visual cortex. This follows the more complex ventral stream visual process as discussed in Section 2.5.3.

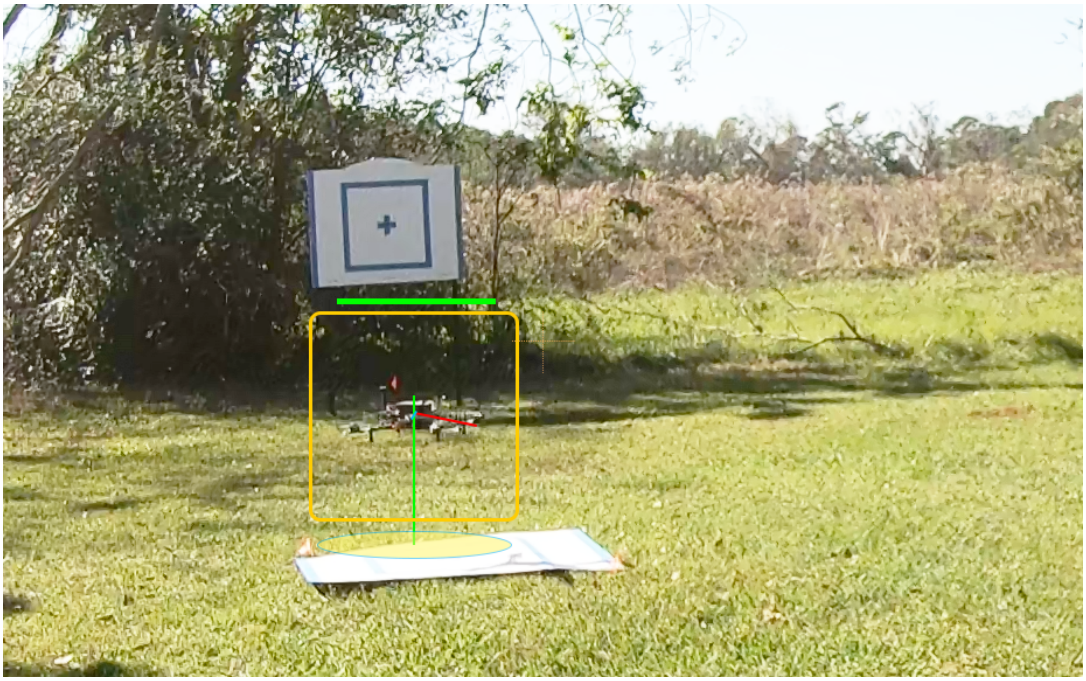

Figure 3.20: Illustration of visual cue attached to `UasBox` object for Experiment 2 part 1.

3.4.3.2 Peripheral FOV-located Cue

For Experiment 2 Part 2, we placed the same cue used in Section 3.4.3.1 in the peripheral FOV of the pilot by projecting it on the outer edge of the HoloLens 2 lens. We also tested for two cases: one case where we presented the cue to the pilot in the superior (upper) peripheral FOV, and a second case where we presented the cue in the inferior (lower) peripheral FOV.

For Survey 2 Evolution 3 of the experiment, we placed the cue in the lower left corner of our Unity scene, at a 45-degree diagonal to the horizontal, also to better engage the peripheral processes. In this position, we ensured that the cue was located

in the inferior peripheral FOV for the non-dominant eye, with the pilot seeing the cue through the left-upper quadrant of their left eye. We elected to display the cue for the pilot's non-dominant eye, which was the left eye in this case, based on research by Jung et al. that indicates that peripheral field processing is asymmetric with respect to "handedness" [98]. With the cue in this position for the left eye, the image is processed through the optic chiasma to the LGN on the opposite side of the brain, through the optic radiations, and directly to the visual cortex. This path follows the dorsal stream visual process associated with the identification of motion and placement of objects in the visual field, as discussed in Section 3.4.3.1.

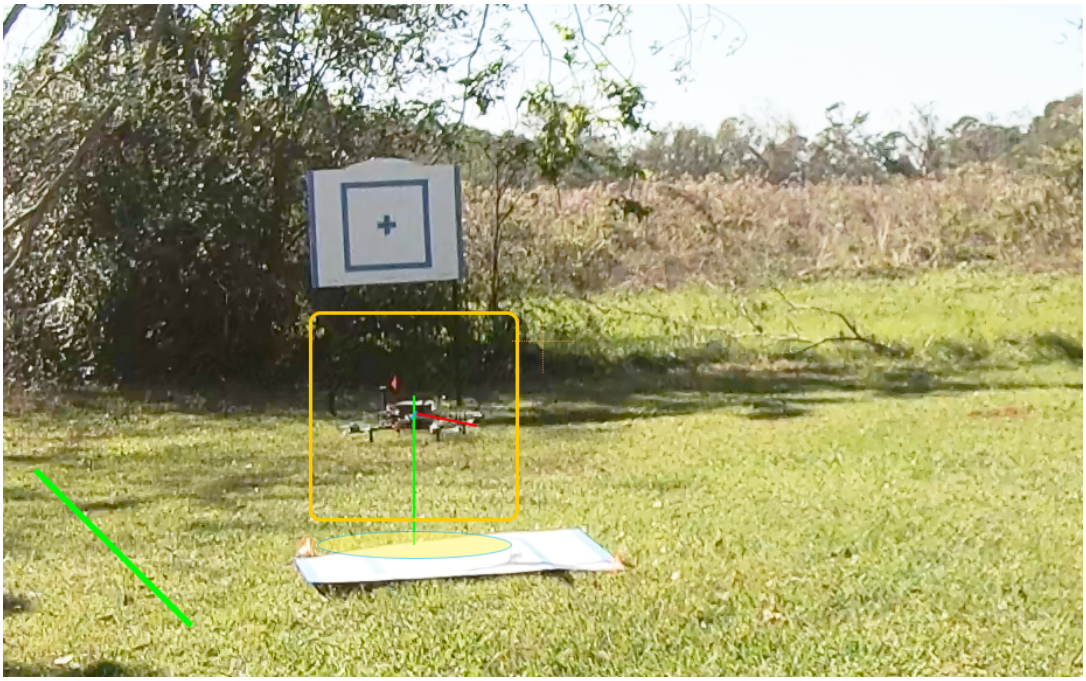

Figure 3.21: Illustration of visual cue shown in inferior peripheral FOV, pilot's non-dominant eye for Experiment 2 part 2b.

CHAPTER 4: METHOD

For our experiments, we selected a variety of tasks from the category of *Precision, Non-Aggressive* as identified in NASA document *CR-2020-220564, Defining Handling Qualities of Unmanned Aerial Systems: Phase II Final Report* [13]. The sUAS used in these experiments was a custom quadcopter built by Abbottics LLC (Charlotte, NC). The vehicle operated under DOD Unmanned Systems Autonomy Level 1, in which the vehicle is under control of a human operator at all times and performs no autonomous or semi-autonomous flight control [99]. The parameters for the quadcopter are outlined in Table A.1 found in Appendix A.

For our experiments, we used the Vehicle 1 variant of the UAS shown in Figure 4.1 to complete the MTEs. The salient difference for this UAS was the choice of a stiffer 11x3.7 carbon fiber propeller to better manage UAS performance under the challenging environmental conditions, primarily a prevailing 7 kt easterly wind present throughout the duration of the experiments. We then evaluated the results of the trials against the results published in ([13]) to compare the accuracy of execution as well as the difficulty of using a transmitter-mounted display to aid in the execution of MTEs.

4.1 Survey 1 - Pilot Performance Baseline

In the first survey, our goal was to use a set of well-defined mission task elements (MTEs) to better understand the competition for pilot attention during a mission using a human-piloted sUAS under real-world operating conditions. These results will be used to better understand how current data feedback methods contribute both to improve and to reduce pilot SA during a mission while also serving to define

a baseline for pilot performance.

We took inspiration for this experiment from Klyde et al. in *NASA/CR-2020-220564, Defining Handling Qualities of Unmanned Aerial Systems: Phase II Final Report* [13]. This report provides a baseline for describing the handling qualities and performance measures of both fixed- and rotary-wing UAS as well as a framework and a set of exercises for measuring the capabilities of the UAS systems.

Figure 4.1: Picture of drone used in Experiment 1. Drone equipped with 11x3.7 propellers in picture; 12x4.5 propeller shown on left for reference.

The specific exercises performed in this experiment are derived from the rotary wing mission task elements (MTEs) as defined in Sections C.1.a (precision hover), .b (lateral sidestep), and .d (landing) with some notable changes in method. First, unlike the evaluations performed at the NASA Langley Research Center (LaRC) Autonomy Incubator as documented in ([13]), our tests were performed outdoors under normal weather conditions (daylight hours, no rain, and wind speed $<$ 10 kt). This is an important differentiating factor, in that the current version of the NASA report does not yet address UAS performance response requirements under turbulence

and gust conditions [13]. Second, we performed two separate variations of this trial: one variation with instrumentation information presented to the pilot via a 4.3-inch LCD display attached to the RF transmitter unit as seen in Figure 4.2 and a second variation only using the pilot's vision to manage the flight. Finally, the Tarot drones used in the LaRC tests were equipped with a Pixhawk PX4 autopilot as the on-board FC, operating as an Autonomy Level 2 vehicle. This capability provides a significant advantage over the Eagle Tree Systems Vector used on the Abbottics drones in that the PX4 FC maintains the current hover level once set by the pilot, even when the UAS is under the influence of cross- or head-winds. For this experiment, the Vector was configured to require continuous control by the pilot. This selection was intentional to make our tests more rigorous and dependent upon pilot performance.

Figure 4.2: Picture of RF transmitter with a standard 4.3 inch LCD monitor used in Experiment 1.

Each activity, or *mission task element* (MTE), falls into one of four classifications of the preciseness or aggressiveness required of the UAS in its performance. In this context, *precision* connotes the requirement of control accuracy of the UAS in its path following as well as smoothness of altitude and attitude changes. Similarly, *aggressiveness* connotes the requirement of the UAS to respond succinctly to sudden and sharp changes to control actuators while maintaining safe and stable flight control. Klyde et al. identify four combinations of these classifications, summarized in Table 4.1 [13].

The layout for each of these exercises is addressed in ([13]) and is shown in Figure 4.3 (a), as adapted for this study. It consists of a circular sector with two radii of 50 ft each from a central point where the pilot stands, swept over a 60° angle. At the end of each of these radii, a marker known as a *hover board* is placed with the target center 5 ft above the ground. This marker, described in Figure 4.3 (b) is used as an indicator of the target vertical distance of the UAS above ground level (AGL), as well as to indicate both vertical and lateral (left-right) horizontal deviation within the *desirable* (less than 1 ft of deviation from center) and *acceptable* (less than 2 ft of deviation from center) accuracy classes. Inside of this sector, a second arc is swept over the same 60° angle from the point with two radii of 25 ft. At the end of each of these shorter radii, a marker known as a *hover* or *landing target* is placed, centered on the endpoint of the radius lines. These markers follow the same format as the hover board, and are used along with the hover boards to indicate the amount of lateral and longitudinal horizontal deviation of the UAS from the center of the target, as well as to serve as a landing zone for the UAS as needed.

Table 4.1: Precision and aggressiveness classes for UAS MTEs. Adapted from Klyde et al. [13].

Category	Description
Non-precision, Non-aggressive	Actions with a high tolerance in phase delay between control actuation and UAS response as well as a low bandwidth requirement for the UAS to safely respond to rapid changes in control surface changes (e.g., normal flight operations inclusive of altitude and attitude adjustments)
Non-precision, Aggressive	Actions with a high tolerance in phase delay between control actuation and UAS response but requiring a high bandwidth requirement for the UAS to safely respond to rapid changes in control surface changes (e.g., obstacle or threat avoidance)
Precision, Non-aggressive	Actions with a lower tolerance in phase delay between control actuation and UAS response as well as a lower bandwidth requirement for the UAS to safely respond to rapid changes in control surface changes (e.g., station keeping, landing, payload delivery, etc.)
Precision, Aggressive	Actions with a lower tolerance in phase delay between control actuation and UAS response as well but a higher bandwidth requirement for the UAS to safely respond to rapid changes in control surface changes (e.g., wind generator cleaning/inspection, aerial dogfighting, etc.)

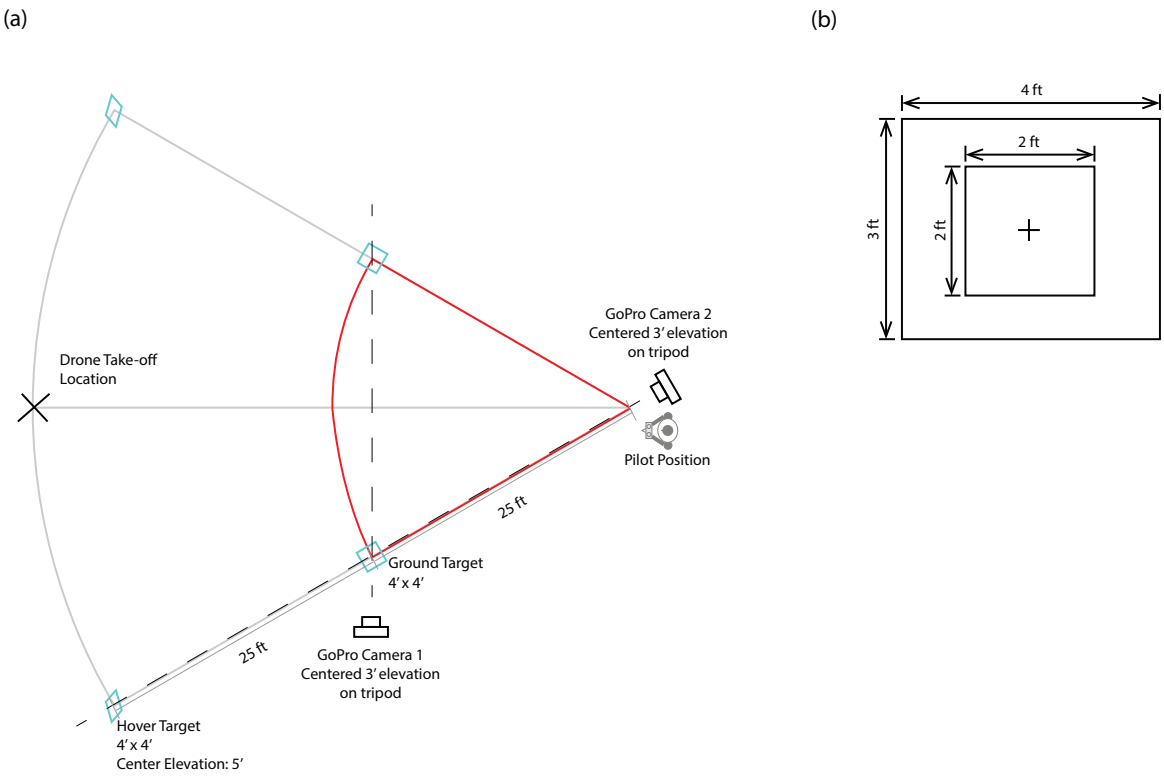

Figure 4.3: Illustration of (a) the drone course used in Experiment 1 and (b) the hover board / landing target specification, as envisioned from Klyde et al. in ([13]).

Each UAS in this experiment is equipped with an Eagle Tree Systems (Bellevue, WA) Vector flight controller (FC). This FC is configured to record telemetry data every 100 ms (10 Hz). The specific data points used in this analysis are shown in Table 4.2. In addition to these data elements, flight notification events are also captured as they occur. The specific flight notification events used for our analysis are the *Multirotor is ARMED* and *Multirotor is DISARMED* events, which bookend each flight's relevant data. An example analysis of the data between a set of armed/disarmed events is shown in Figure 4.4. To compute each metric, we evaluate each sample for the elevation and compass heading variables and compare them to the target values for position at that instant and compute the mean absolute error for the last five consecutive points. The label assigned for this point is then selected based on the desired/adequate/unacceptable criteria for each element. These criteria are defined in each MTE specification. These labels were then augmented with video data to

analyze the physical positioning of the UAS within the target zone for each MTE.

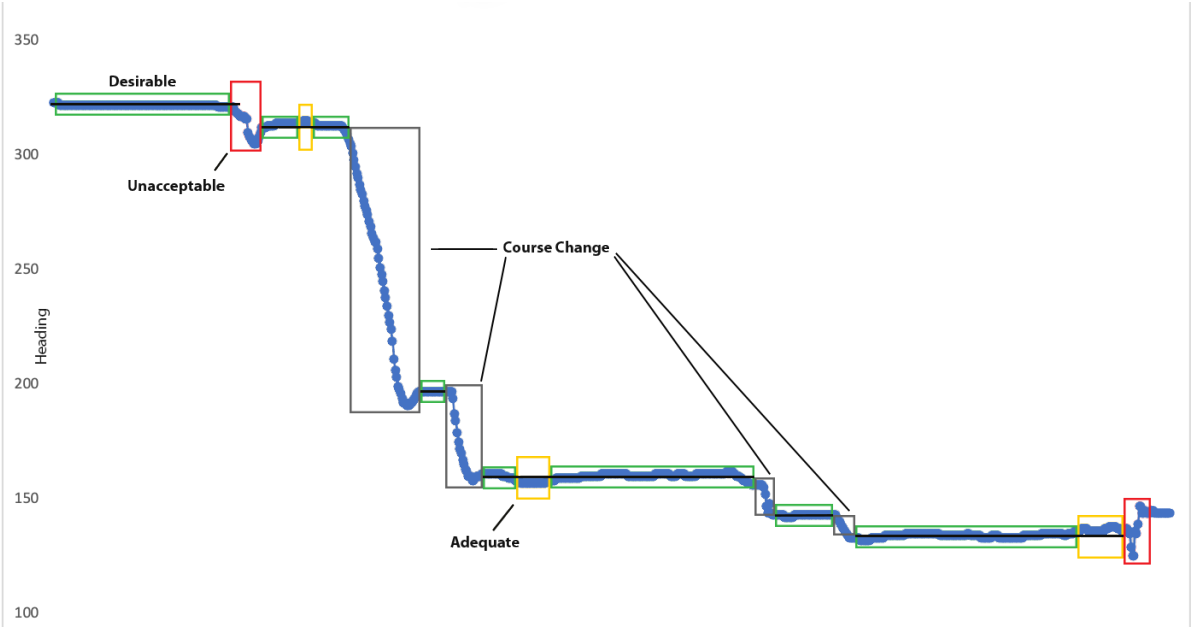

Figure 4.4: Example analysis of UAS flightpath telemetry data captured from Eagle Tree Vector FC.

Table 4.2: Telemetry data elements captured during trial runs.

Element	Description	Range
Altitude	Elevation AGL (ft)	0-30
Compass	Compass heading (deg)	0-360
Pitch	UAS pitch (deg)	±180
Roll	UAS roll (deg)	±180
Yaw	UAS yaw (deg)	±180
Aileron_Rx_Input	Receiver aileron input (%)	0-100
Elevator_Rx_Input	Receiver elevator input (%)	0-100
Rudder_Rx_Input	Receiver rudder input (%)	0-100
Throttle_Rx_Input	Receiver throttle input (%)	0-100

To record the trials from this experiment for later analysis, video was captured using two GoPro (San Mateo, CA) HERO7 action cameras positioned as noted in Figure

4.3. Each camera was mounted on a tripod with a vertical visual center set at three feet AGL. To synchronize video for analysis, each camera was also equipped with a Timecode Systems Ltd. (Worcester, UK) SyncBac PRO timecode generator/transmitter to record a synchronized SMPTE 12M timecode signal in the video streams. Cameras were controlled using the Multi-Cam-Control app written by Harald Meyer on an Apple (Cupertino, CA) iPhone 11 Pro Max. The video files were loaded into Adobe (San Jose, CA) Premiere Pro for analysis.

Five iterations of each variation of the experiment were flown with Vehicle 1, described in Table A.1. Each iteration was evaluated using three classes derived from quantitative values recorded during each maneuver. The three classes are defined in Table 4.3.

Table 4.3: Performance classes for UAS MTEs. Adapted from Klyde et al. [13].

Class	Description
Desired	Meets strictest level of specified tolerances for all identified test criteria; no undesirable vehicle motions that affect task performance
Adequate	Meets lowest acceptable level of specified tolerances for all identified test criteria; no undesirable vehicle motions or oscillations that affect safe flight of the aircraft during task performance
Unacceptable	Does not meet lowest acceptable level of specified tolerances for one or more identified test criteria or the aircraft exhibits undesirable vehicle motions or oscillations that may indicate unsafe vehicle performance during task execution

4.1.1 Precision Hover

In Section 3.1.a of ([13]), the precision hover MTE exercise is defined as a precision, non-aggressive activity with the goal of maintaining a constrained hover over a target after transitioning from a non-aggressive approach of approximately 5 kts, starting from the drone take-off position indicated in Figure 4.5. For this maneuver, the desired(*adequate*) performance criteria are:

- $\geq$30 sec of stabilized hover in desired(*adequate*) region of hover target
- $\pm 1(2)$ ft altitude deviation from hover board center
- $\pm 1(2)$ ft lateral deviation from hover board center
- $\pm 1(2)$ ft longitudinal (fore/aft) deviation from center of hover target
- $\pm 5(10)^\circ$ heading deviation from hover target or hover board
- No undesirable motions that affect task performance (oscillations that impact system stability or flight safety during execution of the MTE)

In our experiment, we performed five trials of each of the left and right precision hover exercises for both the monitor-aided instrument and the visual-only methods. The averages for these trials are shown along with the pilot averages from the LaRC pilot results in Table 4.4. Detailed trial results can be found in Appendix B in Tables B.1 and B.2. With of the significant crosswind ($\sim$7 kt Easterly wind), there were significant challenges keeping the sUAS on-course throughout the maneuver, and it took very significant effort by the pilot to keep the drone on-station once the UAS arrived at each target. Because of the amount of concentration required to maintain control of the aircraft, looking downward to read and interpret the data on the LCD monitor attached to the RF transmitter resulted in loss of control and/or crash of the sUAS in all five trials for both the left and right hover scenarios. For the pilot

visual-only trials, there was a significantly better outcome for all metrics with the exception of fore/aft (Y position) control, similar to the LaRC experiment results. The LaRC trials postulated issues with judging depth perception as a contributing factor to their low scores in this metric. We tend to agree with this belief from our experiences. One trial exhibited the development of a significant PIO during MTE execution, discussed in detail below. Because of the significant risk of damage to the test aircraft, a decision was made to remove the trials associated with the use of the transmitter-mounted LCD display from the remainder of the exercises.

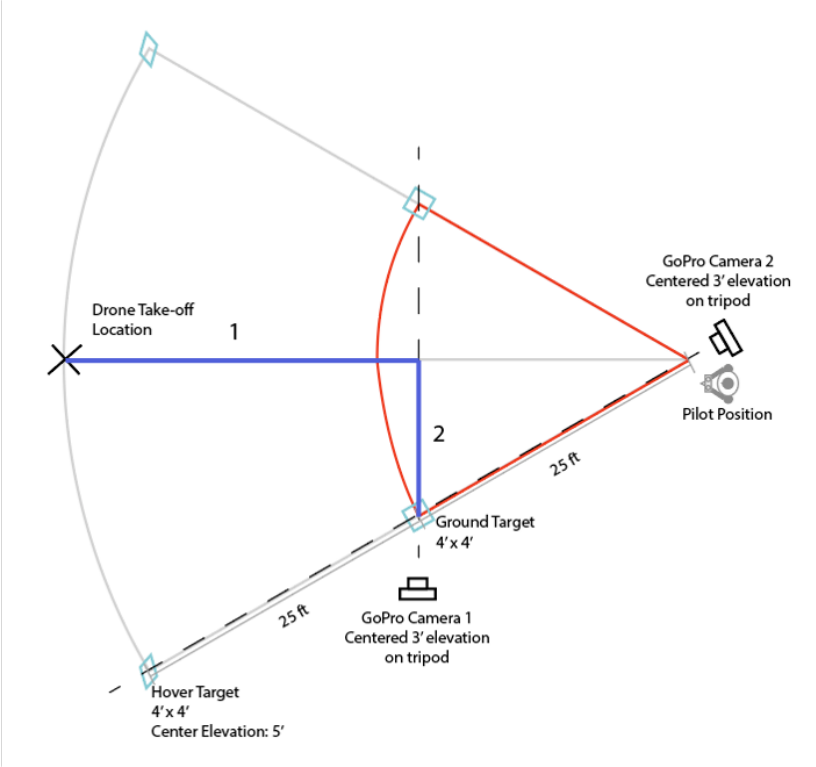

Figure 4.5: Precision hover MTE activity.

Table 4.4: NASA LaRC precision hover MTE pilot performance averages with pilot baselines for Survey 1. From ([13]).

Average Pilot Performance for Precision Hover MTE								
	Altitude		Fore/Aft Position		Lateral Position		Heading Angle	
Pilot	Desired	Adeq.	Desired	Adeq.	Desired	Adeq.	Desired	Adeq.
1	100.00	100.00	36.78	92.11	100.00	100.00	100.00	100.00
2	89.52	100.00	18.23	42.91	99.84	100.00	91.68	100.00
3	80.46	88.15	21.55	35.11	88.96	100.00	81.30	92.33
AVG	89.99	96.05	25.52	56.71	96.27	100.00	90.99	97.44
Disp	32.59	61.42	30.41	43.73	33.51	61.77	52.96	76.70
No Disp	69.97	78.42	39.14	44.75	76.09	83.00	75.88	83.51

In the analysis of the hover component of a Precision Hover trial revealed an interesting insight. The Lorenz maps of the course heading (blue) and yaw (red) during this section of the trial is shown in Figure 4.6. The limit cycle about the 135 deg point represents a Dutch roll flight mode, which is a standard flight dynamics mode in winged aircraft flight. This oscillation is a combination of yaw (indicated by the course changes) and roll (not shown) maneuvers and is not considered to be a form of PIO. In winged aircraft, this would be indicated by a "tail waggle", where the heading remains constant but the pitch and yaw of the aircraft varies; in a rotary-winged aircraft, there is no rear aileron to force the aircraft to fly at an angled flight for extended periods of time. As we see in Figure 4.6, there was a sudden and extreme transition from the oscillation about the 135 deg limit cycle, indicated by the blue and red lines no longer being close to coincident during this transition. As this transition abated, it resulted in a new stable fixed point being established about the 143 deg heading with very similar dynamics as the prior fixed point. The period where the lines are askew represent a Hopf bifurcation and accompanies the regime

shift from the Dutch roll oscillation about the 135 deg stable fixed point to the new Dutch roll oscillation centered about the 143 deg stable fixed point. The observation of this phenomena during our test supports the assertion in Section 2.2.2 regarding the transition between two independent and apparently stable limit cycles via Hopf bifurcation.

A review of the 10 test flights during the precision hover indicated the precision hover exercise found 7 occurrences of PIO-related bifurcations in the data, all associated with the attempt at precision station-keeping above the hover target. At least one of these PIO-transition cycles was corrected through a large increase in throttle, lifting the vehicle out of the oscillation. In review of the qualitative pilot assessment information in Section E.2.b of ([13], commentary is included that all three pilots faced challenges with oscillatory motion during their indoor trials without the presence of wind. The study by Klyde et al. made an assumption that this was caused by dirty air as a result of wind currents from the sUAS rotor wash being reflected back into the flight path of the vehicle causing a force known as *upwash*. We submit that this could serve as a proxy for stray wind currents in an open environment and produced similar results as seen in our trials.

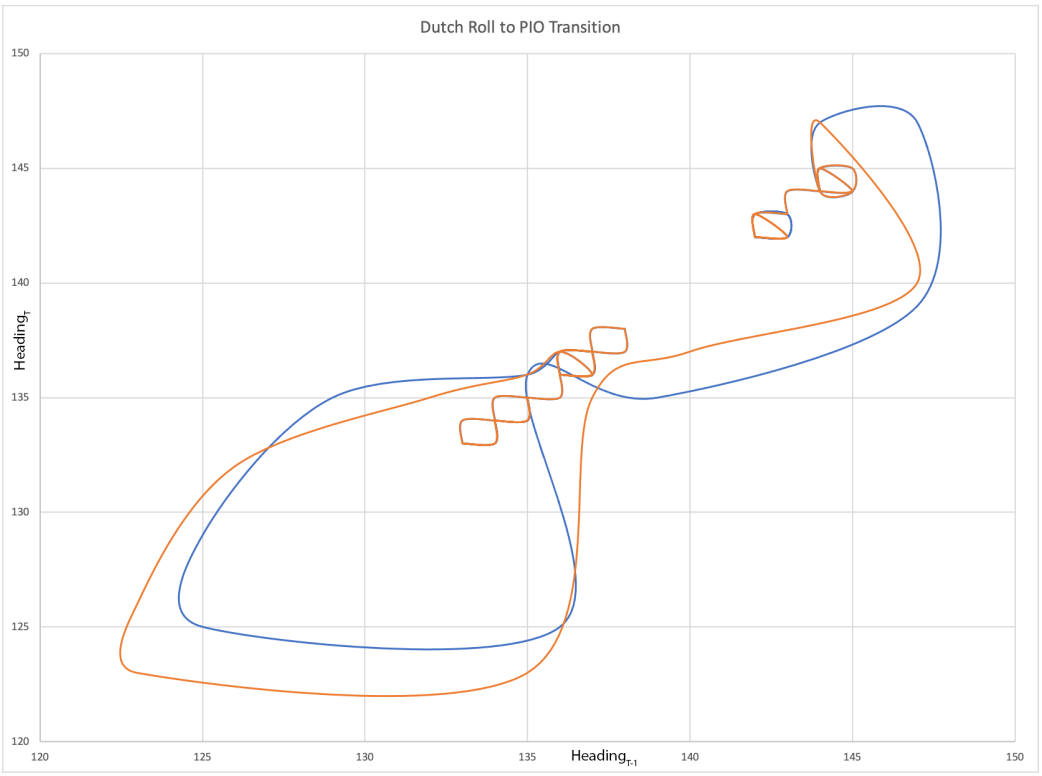

Figure 4.6: Lorenz map of Dutch roll to PIO transition during precision hover trial.

4.1.2 Lateral Sidestep

In Section 3.1.b of ([13]), Klyde et al. describe the lateral sidestep MTE exercise as a precision, non-aggressive activity with the goal of maintaining a constrained hover over a target after transitioning from a non-aggressive approach of approximately 5 kts, starting from the drone take-off position indicated in Figure 4.7. Once a successful hover has been achieved, the pilot must then make a stable transition to the alternate hover pad, accelerating to an approach speed of approximately 5 kts, decelerate smoothly upon reaching the proximate location of the alternate hover target, and maintain a successful hover at that location. Once this hover is complete, the pilot then returns the sUAS to the landing position. An important qualification of this MTE exercise is that each transitory motion component must be executed as a "single smooth maneuver" [13] to properly measure the handling qualities of the sUAS.

For the lateral sidestep MTE maneuver exercise, the desired(adequate) performance criteria are:

- $\pm 1(2)$ ft vertical deviation from hover board center at each capture point
- $\pm 1(2)$ ft lateral deviation from hover board center
- $\pm 1(2)$ ft longitudinal (fore/aft) deviation from center of hover target
- $\pm 5(10)^\circ$ heading deviation from reference heading

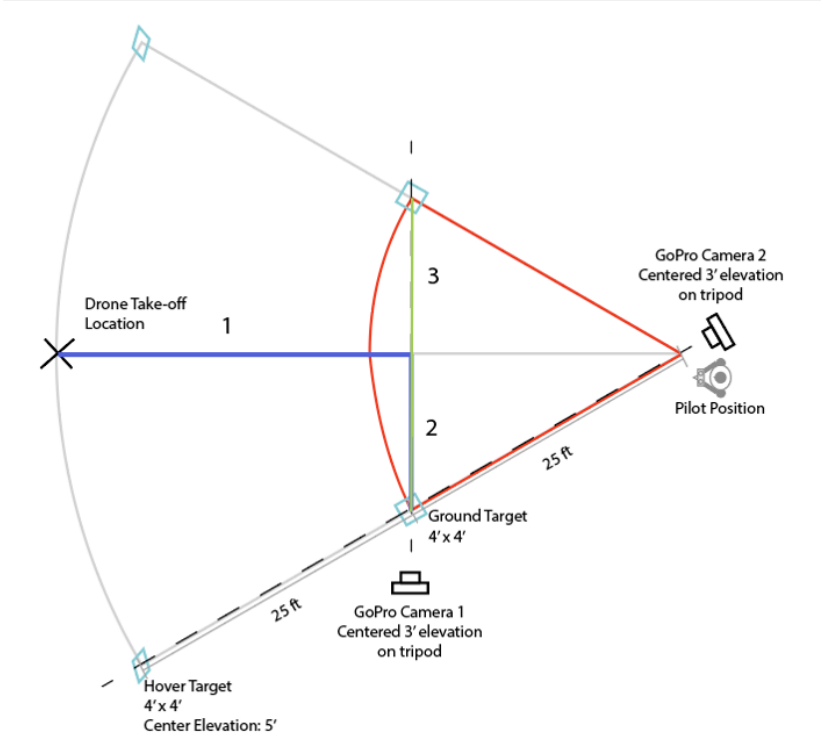

Figure 4.7: Lateral sidestep MTE activity.

In our experiment, we performed five trials of the lateral sidestep exercise using the visual-only method. The averages for these trials are shown along with the pilot averages from the LaRC pilot results in Table 4.5. Detailed trial results can be found in Appendix B in Table B.3. Weather conditions for this experiment were similar to those for the precision hover exercise: sunny, prevailing ~5 kt Easterly wind, and no

rain. As the lateral sidestep exercise is very similar to the precision hover exercise in the previous section, the difference being that, after a ≥30 second hover over the first target, a lateral movement to the second target is required coupled with a second ≥30 second hover. This increases the number of sample points over the time of the exercise, which increases the likeliness of a higher score for the pilot.

Table 4.5: NASA LaRC lateral sidestep MTE pilot performance averages with pilot baselines for Survey 1. From ([13]).

Average Pilot Performance for Lateral Sidestep MTE								
	Altitude		Fore/Aft Position		Lateral Position		Heading Angle	
Pilot	Desired	Adeq.	Desired	Adeq.	Desired	Adeq.	Desired	Adeq.
1	100.00	100.00	43.85	78.32	90.28	99.34	27.26	94.58
2	97.62	99.81	15.62	39.72	72.75	91.52	92.03	99.67
3	85.38	100.00	57.76	94.57	92.60	100.00	77.27	98.16
AVG	94.33	99.94	39.08	70.87	85.21	96.95	65.52	97.47
No Disp	81.90	84.58	44.82	47.89	75.35	86.17	83.51	88.31

Similar to the results in the precision hover exercise, we found evidence of PIOs during station-keeping above each of the hover targets. In Figure 4.8, one PIO is indicated between the first attempt at hover above the left target at an angle of approximately 40 degrees and its tight limit cycle and then the transition to the limit cycle centered at about an 80 degree heading during the successful hover.

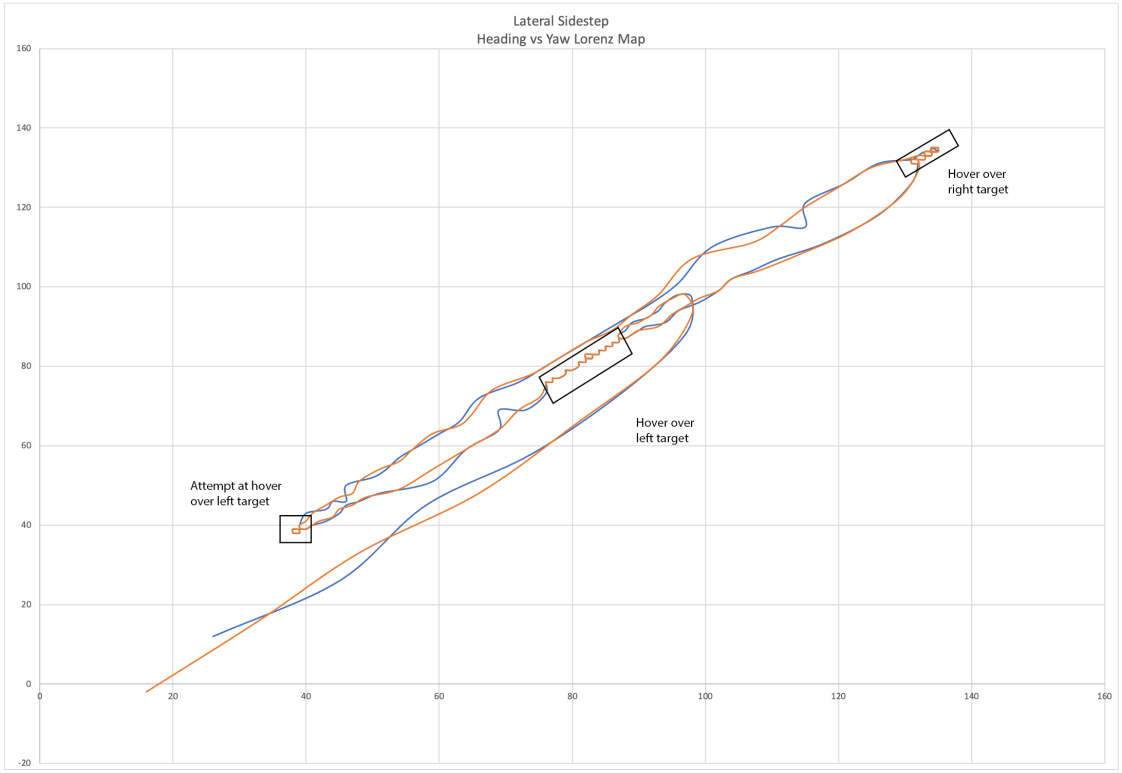

Figure 4.8: Lorenz map of a lateral sidestep trial.

4.1.3 Landing

In Section 3.1.b of ([13]), Klyde et al. describe the landing MTE exercise as a non-precision, non-aggressive activity with the goal of transiting to a position >10 ft over the center of the selected landing target, hover, and then perform a continuous descent until landing as indicated in Figure 4.9. A stop is permitted to adjust the final descent rate prior to touchdown.

For this maneuver, the desired(*adequate*) performance criteria are:

- $\leq 2(4)$ fps vertical speed at touchdown
- $\pm 1(2)$ ft lateral deviation from center of landing target
- $\pm 1(2)$ ft longitudinal (fore/aft) deviation from center of landing target
- $\pm 5(10)^{\circ}$ heading deviation from landing marker

- Smooth, continuous descent with no undesirable motions that affect task performance (no system oscillations during execution of the MTE)

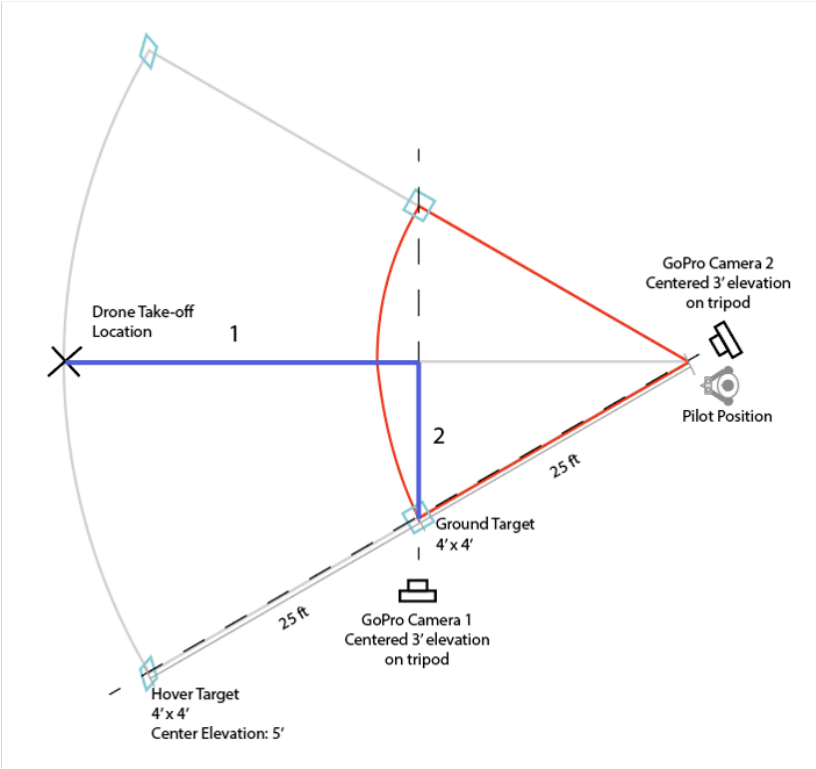

Figure 4.9: Landing MTE activity.

During the execution of this exercise, conditions were sunny with a prevailing Northerly wind at 10 kts, which is extreme for a UAS of this weight class. During the six trials for this activity, we used only the left landing target to provide the maximum clear area to reduce the risk of damage to the vehicle. In three trials, we experienced a Dutch roll oscillation caused by wind gusts preceding the onset of PIO associated with attempting to fight variable winds while attempting to maintain a smooth landing in the 2-4 fps range called for in the standards. Of the six trials, we made one landing that met the criteria for desirable criteria and three that met the adequate criteria. In one case, we experienced a sudden drop from a microburst that caused a crash. The other two trials resulted in off-target landings. In all cases, the closer the vehicle got to the landing position, the greater the oscillation from the

upwash.

Table 4.6: NASA LaRC landing MTE pilot performance averages with pilot baselines for Survey 1. From ([13]).

Average Pilot Performance for Landing MTE								
	Landing Speed		Fore/Aft Position		Lateral Position		Heading Angle	
Pilot	Desired	Adeq.	Desired	Adeq.	Desired	Adeq.	Desired	Adeq.
1	75.00	100.00	84.10	100.00	100.00	100.00	94.62	100.00
2	0.00	100.00	31.30	45.38	84.89	100.00	85.48	99.35
3	33.33	100.00	16.90	30.42	77.99	95.03	78.96	95.79
AVG	36.11	100.00	44.10	58.60	87.63	98.34	86.35	98.38
No Disp	51.90	59.88	44.35	49.07	81.43	84.39	83.00	86.38

4.1.4 Results and Discussion

The goal of this experiment was to apply the UAS handling quality tests to a sUAS in an uncontrolled outdoor environment to better understand how a sUAS under 2.5 lbs operating at Level 1 (human operated) autonomy compared to similar sUAS operating in an indoor environment. To do this, we attempted three of the MTEs outlined in ([13]) using similar sUAS, with and without using a transmitter-attached 4.3" LCD display. After a 100% crash rate in the first experiment, we opted to discontinue trials using the LCD display to minimize risk of destroying a drone. This change only affected our ability to judge the cognitive effects on the pilot of allocating attention between the visual piloting task and the reading of the receiver-attached display.

In all three tasks, our average results were lower than those of the NASA LaRC pilots. This was expected, as 1) the Tarot drones used in the LaRC trials had a higher autonomy level, requiring less direct vehicle control by the pilot during each MTE activity; and, 2) the indoor venue for the LaRC trials did not have to contend

with variable wind conditions and also had controlled lighting. In each of our trials, the vehicle experienced PIO events. After reviewing the notes from each exercise, we identified several contributing factors to these events.

- Similar to the LaRC cases, the ability to judge depth of field caused us to jog the sUAS to help read the fore/aft position of the vehicle. This may have been a contributing factor to PIO occurrence.

- Identification of the front of the drone was problematic at times. This led to errors in translation to control stick movements.

- The crosswind during the precision hover and lateral sidestep maneuvers and the headwind during the landing maneuver caused us to expend a lot of effort keeping the vehicle moving in the correct location. During station-keeping activities, we were constantly struggling to not overshoot or undershoot the position while fighting the crosswind.

- The crosswind also caused issues with landing, as it would suddenly disappear or change direction as the vehicle approached the ground, causing either an abrupt drop in vehicle altitude or a position shift away from the target center.

4.2 Survey 2 - Measure AviatAR-Equipped Pilot Performance

For Survey 2, we used the same course setup as Survey 1 and selected the same three MTEs from *NASA/CR-2020-220564, Defining Handling Qualities of Unmanned Aerial Systems: Phase II Final Report* [13]. The primary differences between Surveys 1 and 2 were:

- Vehicle 2 was equipped with the NVIDIA Nano, Intel RealSense cameras, and u-blox C099-F9P module

- Pilot wore the Microsoft HoloLens 2 HMD during MTE trials

- MTE missions were flown in the early hours of the morning

The inclusion of the sensor package on the UAS increased the weight by 430 grams. The larger propellers on Vehicle 2 provided the additional lifting power to negate the extra weight. We also found that the Microsoft HoloLens 2 display, not being specifically designed for outdoor use, did not have sufficient brightness to be useful during daylight or early evening, as the pilot faces the setting sun on our course. To overcome this, missions were flown 30 minutes after morning civil twilight to have minimal light effects and to meet legal requirements for UAS flight under 14 CFR Part 107 rules [2, 64]. The MTE missions were flown with a prevailing 8 kt Northerly wind for parity with the flights from Experiment 1. For each experiment, we performed five trials of each of the three MTEs for each of the three visual cue configurations. This took three days to complete to maintain suitable conditions for the HoloLens to be readable.

Prior to each set of experiments, the UAS and HMD calibration procedures were carried out on each day of trials. This helped to ensure consistency in the course layout from day to day, as the ground targets were taken in each night to minimize effects of overnight dew caused by the relatively high humidity of south Alabama. During both calibration and flight operations, both GoPro cameras were in-place and actively recording as in Experiment 1.

4.2.1 Evolution 1 - HMD with Gizmo Only

For Evolution 1, we equipped our pilot with the Microsoft HoloLens 2 AviatAR HMD with only the Gizmo feature to improve pilot awareness of UAS fore/aft and lateral position as well as heading while in flight. Similar to Survey 1, we conducted five trials of the precision hover, lateral sidestep, and landing maneuvers. The details for each of these maneuvers are found in Tables 4.7, 4.8, and 4.9, respectively.

Table 4.7: NASA LaRC precision hover MTE pilot performance averages for survey 2 evolution 1 - HMD with Gizmo only. From ([13]).

Average Pilot Performance for Precision Hover MTE								
	Altitude		Fore/Aft Position		Lateral Position		Heading Angle	
Pilot	Desired	Adeq.	Desired	Adeq.	Desired	Adeq.	Desired	Adeq.
1	100.00	100.00	36.78	92.11	100.00	100.00	100.00	100.00
2	89.52	100.00	18.23	42.91	99.84	100.00	91.68	100.00
3	80.46	88.15	21.55	35.11	88.96	100.00	81.30	92.33
AVG	89.99	96.05	25.52	56.71	96.27	100.00	90.99	97.44
No Disp	69.97	78.42	39.14	44.75	76.09	83.00	75.88	83.51
Gizmo	82.23	84.68	88.61	91.65	91.49	94.36	92.17	93.90

Table 4.8: NASA LaRC lateral sidestep MTE pilot performance averages for survey 2 evolution 1 - HMD with Gizmo only. From ([13]).

Average Pilot Performance for Lateral Sidestep MTE								
	Altitude		Fore/Aft Position		Lateral Position		Heading Angle	
Pilot	Desired	Adeq.	Desired	Adeq.	Desired	Adeq.	Desired	Adeq.
1	100.00	100.00	43.85	78.32	90.28	99.34	27.26	94.58
2	97.62	99.81	15.62	39.72	72.75	91.52	92.03	99.67
3	85.38	100.00	57.76	94.57	92.60	100.00	77.27	98.16
AVG	94.33	99.94	39.08	70.87	85.21	96.95	65.52	97.47
No Disp	81.90	84.58	44.82	47.89	75.35	86.17	83.51	88.31
Gizmo	84.90	87.80	90.94	92.83	91.16	92.24	91.94	94.21

Table 4.9: NASA LaRC landing MTE pilot performance averages for survey 2 evolution 1 - HMD with Gizmo only. From ([13]).

Average Pilot Performance for Landing MTE								
	Landing Speed		Fore/Aft Position		Lateral Position		Heading Angle	
Pilot	Desired	Adeq.	Desired	Adeq.	Desired	Adeq.	Desired	Adeq.
1	75.00	100.00	84.10	100.00	100.00	100.00	94.62	100.00
2	0.00	100.00	31.30	45.38	84.89	100.00	85.48	99.35
3	33.33	100.00	16.90	30.42	77.99	95.03	78.96	95.79
AVG	36.11	100.00	44.10	58.60	87.63	98.34	86.35	98.38
No Disp	51.90	59.88	44.35	49.07	81.43	84.39	83.00	86.38
Gizmo	50.20	54.21	88.62	91.63	90.10	92.17	82.81	89.52

4.2.1.1 Discussion

As compared to unaided pilot performance in Survey 1, a simple analysis of pilot performance for the HMD-equipped pilot for Evolution 1 shows improvement in practically every metric for all three MTE maneuvers, with the most dramatic improvements in the Fore/Aft Position metric. One metric associated with the Landing MTE, Landing Speed, showed no improvement over that of the unaided pilot. This seems a reasonable outcome, in that the Gizmo added in Evolution 1 provides no functionality to assist the pilot with vehicle speed control during ascent or descent.

4.2.2 Evolution 2 - Superior FOV-located Cue

For Evolution 2, we equipped our pilot with the Microsoft HoloLens 2 AviatAR HMD with the Gizmo feature but we included a visual cue to indicate PIO severity during flight. We placed the PIO severity cue at the top of the Gizmo in the pilot's superior field of vision. Similar to Survey 1, we conducted five trials of the precision hover, lateral sidestep, and landing maneuvers. The details for each of these maneuvers are found in Tables 4.10, 4.11, and 4.12, respectively.

4.2.2.1 Precision Hover

Table 4.10: NASA LaRC precision hover MTE pilot performance averages for survey 2 evolution 2 - HMD with Gizmo and superior FOV-located PIO onset cue. From ([13]).

Average Pilot Performance for Precision Hover MTE								
	Altitude		Fore/Aft Position		Lateral Position		Heading Angle	
Pilot	Desired	Adeq.	Desired	Adeq.	Desired	Adeq.	Desired	Adeq.
1	100.00	100.00	36.78	92.11	100.00	100.00	100.00	100.00
2	89.52	100.00	18.23	42.91	99.84	100.00	91.68	100.00
3	80.46	88.15	21.55	35.11	88.96	100.00	81.30	92.33
AVG	89.99	96.05	25.52	56.71	96.27	100.00	90.99	97.44
No Disp	69.97	78.42	39.14	44.75	76.09	83.00	75.88	83.51
Gizmo+Cue	88.40	89.96	93.38	93.91	92.56	93.70	87.11	88.66

4.2.2.2 Lateral Sidestep

Table 4.11: NASA LaRC lateral sidestep MTE pilot performance averages for survey 2 evolution 2 - HMD with Gizmo and superior FOV-located PIO onset cue. From ([13]).

Average Pilot Performance for Lateral Sidestep MTE								
	Altitude		Fore/Aft Position		Lateral Position		Heading Angle	
Pilot	Desired	Adeq.	Desired	Adeq.	Desired	Adeq.	Desired	Adeq.
1	100.00	100.00	43.85	78.32	90.28	99.34	27.26	94.58
2	97.62	99.81	15.62	39.72	72.75	91.52	92.03	99.67
3	85.38	100.00	57.76	94.57	92.60	100.00	77.27	98.16
AVG	94.33	99.94	39.08	70.87	85.21	96.95	65.52	97.47
No Disp	81.90	84.58	44.82	47.89	75.35	86.17	83.51	88.31
Gizmo+Cue	90.31	91.24	93.54	94.05	92.74	93.57	88.64	90.22

4.2.2.3 Landing

Table 4.12: NASA LaRC landing MTE pilot performance averages for survey 2 evolution 2 - HMD with Gizmo and superior FOV-located PIO onset cue. From ([13]).

Average Pilot Performance for Landing MTE								
	Landing Speed		Fore/Aft Position		Lateral Position		Heading Angle	
Pilot	Desired	Adeq.	Desired	Adeq.	Desired	Adeq.	Desired	Adeq.
1	75.00	100.00	84.10	100.00	100.00	100.00	94.62	100.00
2	0.00	100.00	31.30	45.38	84.89	100.00	85.48	99.35
3	33.33	100.00	16.90	30.42	77.99	95.03	78.96	95.79
AVG	36.11	100.00	44.10	58.60	87.63	98.34	86.35	98.38
No Disp	51.90	59.88	44.35	49.07	81.43	84.39	83.00	86.38
Gizmo+Cue	54.21	55.14	93.76	94.36	93.23	93.99	88.57	89.80

4.2.2.4 Discussion

As in Evolution 1, a simple analysis of pilot performance indicates similar improvements in metrics for all three MTE maneuvers. In Evolution 2, though, we also see improvements for each metric as compared to Evolution 1, indicating that presence of the PIO cue may be associated with improved levels of pilot performance. This seems reasonable from a cursory analysis of PIO detection and mitigation rates between Evolution 1 and Evolution 2, as seen in Tables C.2, C.4, and C.6 for Evolution 1 and in Tables C.8, C.10, and C.12 for Evolution 2, located in Appendix C. With the presence of the PIO cue, detected PIOs were mitigated at a much higher rate than in the absence of the cue, as would be reasonably expected. We believe it is reasonable to infer that this increased level of PIO mitigation effectiveness should manifest itself in better overall MTE performance.

4.2.3 Evolution 3 - Inferior Peripheral FOV-located Cue

For Evolution 3, we relocated the PIO Severity Cue from the top of the Gizmo in the superior FOV to the bottom left of the HMD display in the pilot's inferior peripheral FOV. The goals of this evolution were twofold: first, to determine if the placement of the cue in the inferior peripheral FOV would improve pilot performance by taking advantage of the ventral stream visual processing system and, secondly, to determine if placement of a persistent visual cue in the inferior peripheral FOV would have detrimental impacts on pilot performance associated with an attention-seeking shift in visual attention associated with changes to the cue. As in Evolution 2, we conducted five trials for each of the MTEs and the details for each of these maneuvers are found in Tables 4.13, 4.14, and 4.15, respectively.

4.2.3.1 Precision Hover

Table 4.13: NASA LaRC precision hover MTE pilot performance averages for survey 2 evolution 3 - HMD with Gizmo and inferior peripheral FOV-located PIO onset cue. From ([13]).

Average Pilot Performance for Precision Hover MTE								
	Altitude		Fore/Aft Position		Lateral Position		Heading Angle	
Pilot	Desired	Adeq.	Desired	Adeq.	Desired	Adeq.	Desired	Adeq.
1	100.00	100.00	36.78	92.11	100.00	100.00	100.00	100.00
2	89.52	100.00	18.23	42.91	99.84	100.00	91.68	100.00
3	80.46	88.15	21.55	35.11	88.96	100.00	81.30	92.33
AVG	89.99	96.05	25.52	56.71	96.27	100.00	90.99	97.44
No Disp	69.97	78.42	39.14	44.75	76.09	83.00	75.88	83.51
Gizmo+Cue	93.40	94.16	92.41	93.08	93.76	94.80	90.73	92.02

4.2.3.2 Lateral Sidestep

Table 4.14: NASA LaRC lateral sidestep MTE pilot performance averages for survey 2 evolution 3 - HMD with Gizmo and inferior peripheral FOV-located PIO onset cue. From ([13]).

Average Pilot Performance for Lateral Sidestep MTE								
	Altitude		Fore/Aft Position		Lateral Position		Heading Angle	
Pilot	Desired	Adeq.	Desired	Adeq.	Desired	Adeq.	Desired	Adeq.
1	100.00	100.00	43.85	78.32	90.28	99.34	27.26	94.58
2	97.62	99.81	15.62	39.72	72.75	91.52	92.03	99.67
3	85.38	100.00	57.76	94.57	92.60	100.00	77.27	98.16
AVG	94.33	99.94	39.08	70.87	85.21	96.95	65.52	97.47
No Disp	81.90	84.58	44.82	47.89	75.35	86.17	83.51	88.31
Gizmo+Cue	93.34	94.09	94.26	95.00	94.38	95.52	90.47	92.09

4.2.3.3 Landing

Table 4.15: NASA LaRC landing MTE pilot performance averages for survey 2 evolution 3 - HMD with Gizmo and inferior peripheral FOV-located PIO onset cue. From ([13]).

Average Pilot Performance for Landing MTE								
	Landing Speed		Fore/Aft Position		Lateral Position		Heading Angle	
Pilot	Desired	Adeq.	Desired	Adeq.	Desired	Adeq.	Desired	Adeq.
1	75.00	100.00	84.10	100.00	100.00	100.00	94.62	100.00
2	0.00	100.00	31.30	45.38	84.89	100.00	85.48	99.35
3	33.33	100.00	16.90	30.42	77.99	95.03	78.96	95.79
AVG	36.11	100.00	44.10	58.60	87.63	98.34	86.35	98.38
No Disp	51.90	59.88	44.35	49.07	81.43	84.39	83.00	86.38
Gizmo+Cue	71.06	75.88	92.96	95.01	92.97	95.28	87.57	90.34

4.2.3.4 Discussion

As in Evolution 2, we see similar improvements in metrics for all three MTE maneuvers as well as improvements in PIO mitigation rates between Evolution 2 and Evolution 3, as seen in Tables C.8, C.10, and C.12 for Evolution 2 and in Tables C.14, C.16, and C.18 for Evolution 2, located in Appendix C. With all other components of these evolutions being identical with the exception of the PIO Severity Cue location, we believe that it is reasonable to infer from these results that cue location in the inferior peripheral FOV may contribute to better pilot performance.

CHAPTER 5: ANALYSIS AND DISCUSSION

In this section, we attempt to evaluate our research hypotheses using the data from our surveys. From our first subject area, we will evaluate whether our survey data supports our hypotheses that an AR display can improve pilot accuracy and control and can help overcome the effects of pilot-aircraft distance on task accuracy. From our second subject area, we will also evaluate how cue placement affects pilot performance and discuss how these placements may take advantage of the structure of the human visual system to improve pilot focus and reduce cognitive load during mission execution.

5.1 Effect of AviatAR HMD with Gizmo on Positional Accuracy for MTEs

For this analysis, we compare both the Fore/Aft and Lateral Positional Accuracy metrics for the unaided pilot versus those of a pilot equipped with the AviatAR HMD with the Gizmo component. To evaluate this, we used the data from Appendix B for the unaided pilot performance and from Appendix C Section C.1 for the pilot equipped with the HMD with Gizmo component.

5.1.1 Design of Experiment

For this analysis, we compare the positional accuracy metrics for each of the MTE maneuvers for the unaided pilot from Survey 1 versus the pilot equipped with the AviatAR HMD with the Gizmo component from Survey 2 Evolution 1. Our hypotheses for this experiment are

H_0: There is no significant difference in positional accuracy between the unaided pilot and the pilot equipped with the AviatAR HMD with the Gizmo component

H_1: There is a significant difference in the two operators' positional accuracy for both

methods.

For our two samples, we have the following statistics for Fore/Aft and Lateral Positional Accuracy:

Table 5.1: Summary sample statistics for analysis of Positional Accuracy of unaided pilot versus pilot equipped with AviatAR HMD with Gizmo component.

	Survey 1		Survey 2 Evolution 1	
	Fore/Aft	Lateral	Fore/Aft	Lateral
Mean	39.14	76.09	88.61	91.49
Std Dev	9.10	10.64	5.34	1.34
N	5	5	5	5

Since we have two different pilot experiences, we will assume that the population standard deviations are not equal between the two groups. This requires us to determine the degrees of freedom in a more restrictive manner using the degrees of freedom for unequal variance test. The equation to calculate the degrees of freedom (df) for this experiment is defined as

$$df = \left\lfloor \frac{\left[\frac{s_1^2}{n_1} + \frac{s_2^2}{n_2}\right]^2}{\frac{\left(\frac{s_1^2}{n_1}\right)^2}{n_1 - 1} + \frac{\left(\frac{s_2^2}{n_1}\right)^2}{n_2 - 1}} \right\rfloor \tag{5.1}$$

5.1.2 Analysis

5.1.2.1 Fore/Aft Positional Accuracy

First, we compute the t-value for the Fore/Aft Positional Accuracy metric between the two populations. Substituting our values from Table 5.1 into Equation 5.1, we get a value of $df = 6$, which is reduced from $df = 8$ if we had assumed equal population standard deviations between the groups. We now compute our t value using the two-sample test of means for unknown and unequal σ_s using the equation

$$t = \left| \frac{\overline{X_1} - \overline{X_2}}{\sqrt{\frac{s_1^2}{n_1} + \frac{s_2^2}{n_2}}} \right| \tag{5.2}$$

Substituting our values from Table 5.1 into Equation 5.2, we get a value of $t = 10.48$. Consulting the Student's t distribution for a one-tailed test with a 95% CI, $\alpha = 0.025$, and $df = 6$, we find that we need a value of $t = 2.447$ in order to reject H_0 and accept our alternative hypothesis that positional accuracy for the pilot equipped with the AviatAR HMD with the Gizmo component is different than that for the unaided pilot. Since our t value is much greater than that value, we can indeed conclude that there is a difference in Fore/Aft Positional Accuracy between the two methods.

5.1.2.2 Lateral Positional Accuracy

Now, we will compute the t-value for the Lateral Positional Accuracy metric between the two populations. As we did for the Fore/Aft Positional Accuracy metric, we substute the values from Table 5.1 into Equation 5.1, we get a value of $df = 4$, which is reduced from $df = 8$ if we had assumed equal population standard deviations between the groups. We now compute our t value using the two-sample test of means for unknown and unequal σ_s using Equation 5.2. Substituting our values from Table 5.1 into Equation 5.2 for Lateral Positional Accuracy, we get a value of $t = 3.21$. Consulting the Student's t distribution for a one-tailed test with a 95% CI, $\alpha = 0.025$, and $df = 6$, we find that we need a value of $t = 2.776$ in order to reject H_0 and accept our alternative hypothesis that positional accuracy for the pilot equipped with the AviatAR HMD with the Gizmo component is different than that for the unaided pilot. Since our t value is greater than that value, we can indeed conclude that there is also a difference in Lateral Positional Accuracy between the two methods.

5.1.3 Discussion

Now that we have established that there is a significant difference in positional accuracy for both metrics by using the AviatAR display, we can conclude from a simple analysis of the data for both metrics that positional accuracy is better for the AviatAR user than for the unaided pilot. It is intuitive to us that this would be the case, since the Gizmo component provides an indicator of the ground position located beneath the UAS, providing the pilot with direct visual verification that the UAS is in its required position during MTE execution.

5.2 Effect of AviatAR HMD with PIO Cue on PIO Mitigation

For this analysis, we compare both the Fore/Aft and Lateral Positional Accuracy metrics for the unaided pilot versus those of a pilot equipped with the AviatAR HMD with the Gizmo component augmented with the PIO Onset cue. To evaluate this, we used the data from Appendix C Sections C.1 and C.2 for the pilot equipped with the HMD with Gizmo component both without and with the PIO Onset cue.

5.2.1 Design of Experiment

In this experiment, we evaluate if the addition of the PIO Cue to the Gizmo has an effect on the pilot's ability to identify and mitigate the onset and effects of a PIO during a UAS mission. Our hypotheses for this experiment are

H_0: There is no significant difference in a pilot's ability to identify and mitigate PIO onset between the pilot equipped with the AviatAR HMD with the Gizmo component only and the pilot equipped with the AviatAR HMD with the Gizmo component + the PIO cue.

H_1: There is a significant difference in the pilot's ability to identify and mitigate PIO onset between the two methods.

For our two samples, we have the following statistics for PIO Mitigation Rate:

Table 5.2: Summary sample statistics for analysis of PIO Mitigation Rate of pilot equipped with AviatAR HMD with Gizmo component versus pilot equipped with AviatAR HMD with Gizmo component + PIO cue.

	Survey 2 Evolution 1	Survey 2 Evolution 2
	PIO Mitigation %	PIO Mitigation %
Mean	62.78	90.31
Std Dev	5.89	1.87
N	13	10

5.2.2 Analysis

To better understand the context of this analysis and to provide proper rigor to support our hypothesis, we first will examine the effects of pilot performance when equipped with the AviatAR HMD combined with both the Gizmo and the PIO Indicator cue. The Matlab programs used to analyze data for this section can be found in Appendix D. The definition of the cue states was discussed in Section 3.4.3. The persistent PIO Indicator cue is rendered as green for principal frequency spectrum $\nu \leq 10$ Hz, yellow for the presence of signal components $\nu > 10$ Hz with amplitudes > 2 but less than 5 in aggregate for all components > 10 Hz, and red for any condition exceeding yellow state. During normal flight operation, the pilot is presented with a persistent PIO Cue colored as green, and this cue will change color during flight operations with respect to the magnitude of PIO detected. The representative frequency spectra for each of these states are represented in Figure 5.1.

In Figure 5.2, we see a representation of a UAS flight segment that indicates the pilot control and vehicle response during operation in blue, along with the current state of the PIO cue displayed in the AviatAR HMD. For the segment of flight selected for this analysis, we have identified four distinct regimes during this operation. We identify these as

- Phase 1, indicative of normal flight up to the onset of a severe PIO;
- Phase 2, indicative of pilot awareness and resolution of a severe PIO;
- Phase 3, indicative of pilot awareness of PIO and successful prevention of escalation; and,
- Phase 4, onset of a severe PIO event and pilot attempts at mitigation with MTE failure.

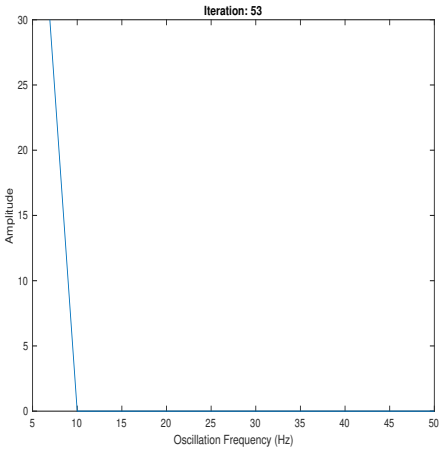

(a) Green Indicator

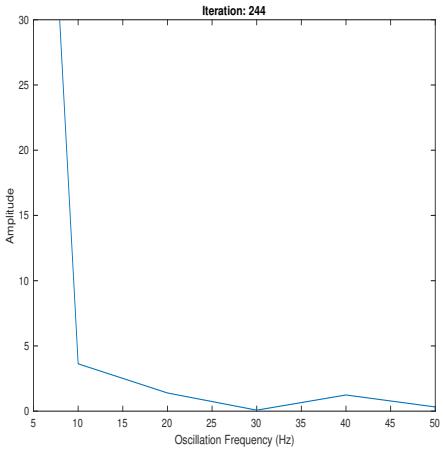

(b) Yellow Indicator

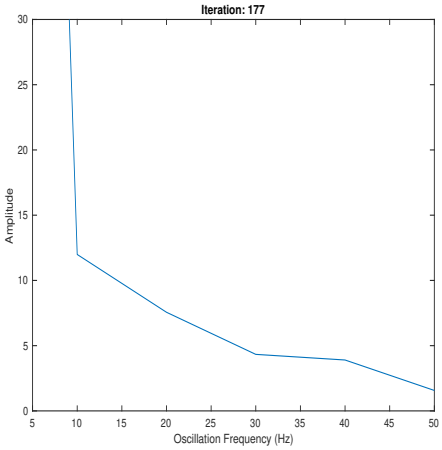

(c) Red Indicator

Figure 5.1: Representative frequency spectra for corresponding PIO Indicator cue colors.

In the Figure 5.2 (a), Phase 1 flight regime, we see two transitions from green cue to yellow and even red cue in the 1020 to 1040 and 1070 to 1085 millisecond timeframes, each of which were smoothly handled by the pilot with no significant divergence on the system forcing function $i(t)$ versus the pilot control function $c(t)$. Starting at approximately 1090 ms into the flight, however, we see a detected PIO escalation that resulted in the cue progressing to yellow and red, along with significant divergence between $i(t)$ and $c(t)$ in this timeframe. This signals a regime shift from normal flight mode to an active PIO flight mode.

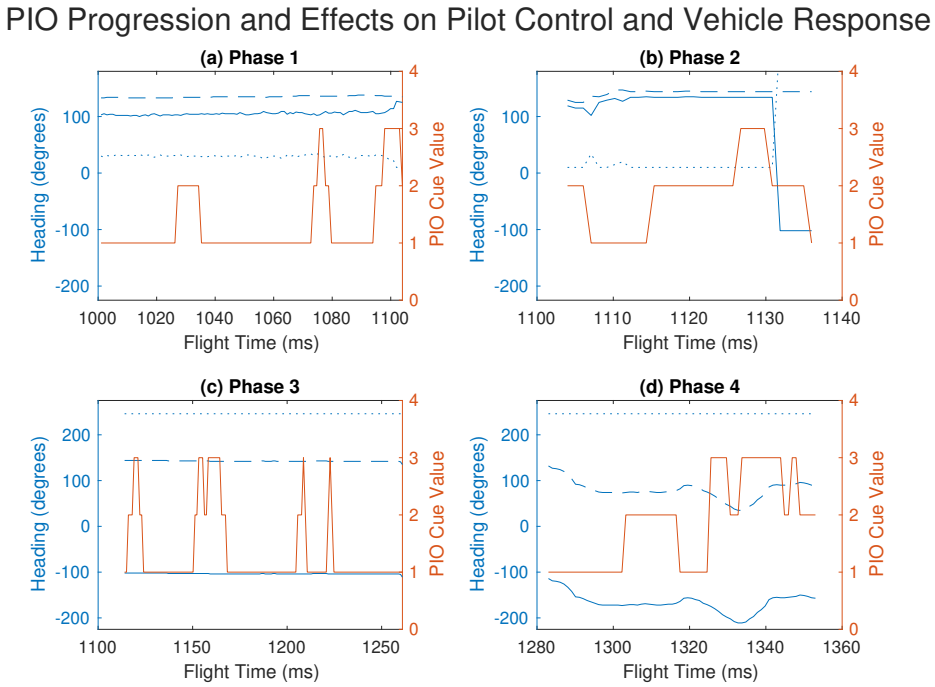

Figure 5.2: Four phases of PIO onset and resolution. The forcing function $i(t)$ is represented by the solid blue line, the pilot control function $c(t)$ by the dotted blue line, vehicle relative position $\Delta m(t)$ by the dashed blue line, and the PIO indicator level by the solid orange line.

The Phase 2 active PIO flight mode regime is shown in Figure 5.2 (b). Between 1100 and 1115 ms of flight, we see the pilot making aggressive adjustments to flight controls to recover the UAS to stable flight, resulting in the cue returning to green state at approximately 1108 ms. The pilot and vehicle interactions during this timeframe are

shown in greater detail in Figure 5.3. At approximately 1107 to 1109 ms, we see that the pilot controls and the vehicle control surfaces, specifically the rudder, are 180-degrees out of phase, and we see this again between 1111 and 1114 ms. This condition meets the canonical standard for the presence of a PIO, as discussed in Section 2.2.

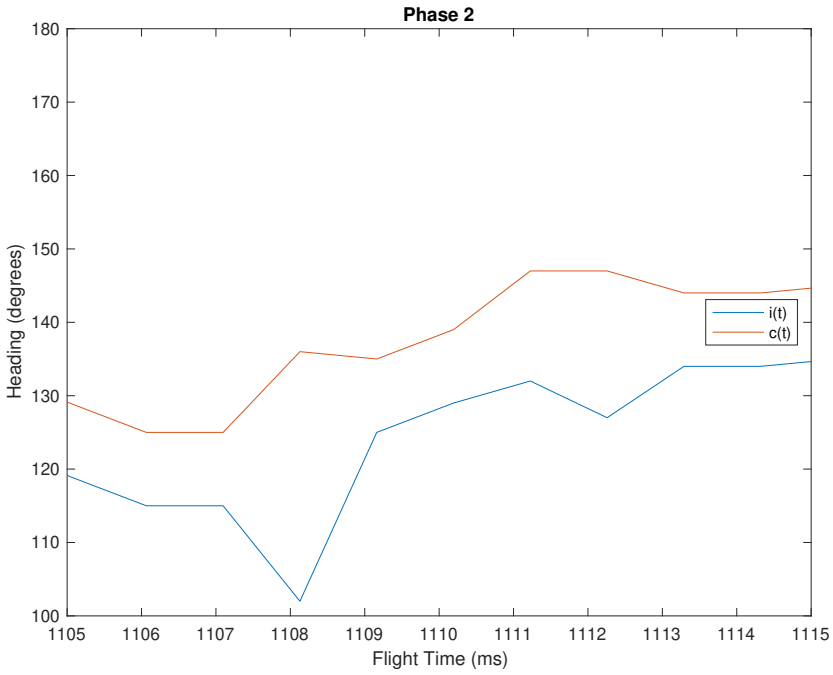

Figure 5.3: Detail of control function versus system forcing function during Phase 2 flight.

In Figure 5.2 (c), we see a return to a normal flight regime. This regime includes multiple cue shifts to yellow and red followed by a return to green, with no significant progression of pilot-vehicle pathological divergences. This pattern indicates smooth mitigation of PIO onset by the pilot. This normal flight regime continues from approximately 1150 to 1280 ms of flight.

At approximately 1280 ms into flight, we enter the final regime as shown in Figure 5.2 (d). Notes from the experiment indicate that at this point in the flight a strong northerly gust was encountered during a lateral sidestep maneuver transitioning from

the southern target to the northern target. The pilot began making adjustments prior to cue transition, indicative of the precognitive mode described by the Successive Order of Perceptions model [62] discussed in Section 2.5.1. At approximately 1330 ms, the cue escalates to red state and oscillates until approximately 1350 ms, at which point the mission was terminated by hard landing of the UAS by the pilot. It should be noted that a hard landing is a choice made by a pilot to aggressively terminate a flight to avoid significant damage to the aircraft or property or injury to others. This is different from a crash landing, which is an limited or uncontrolled termination of a flight.

The above analysis demonstrates that the PIO detection model does indeed predict the onset and severity of conditions favoring development of a PIO condition. This analysis also supports that the presence of the PIO Cue is used by the pilot to perform activities to suppress escalation of PIO development during flight. We suggest that this is indicative of improved pilot SA, at least with respect to PIO onset.

Similar to our previous experiment, we have to different pilot experiences in which the pilot may perform differently in the presence of the PIO cue, so we will once again assume that the variance will be different for both populations. To compute the degrees of freedom for our experiment, we use Equation 5.1 and populate the values from Table 5.2. Plugging in the data from our surveys, we get a result of $df = 15$ for our experiment. Now, using Equation 5.2, we calculate our t-value to be $t = 15.85$. Consulting the T-distribution for a one-tailed test with a 95% CI, $\alpha = 0.025$, and $df = 15$, we find that we need a value of $t = 2.131$ in order to reject H_0 and accept our alternative hypothesis. Since our computed t-value of 15.85 is significantly larger than the required value, we can safely reject H_0 and accept our alternative hypothesis that the pilot's ability to mitigate PIO onset is significantly different when equipped with both the Gizmo and the PIO cue versus the Gizmo alone.

5.2.3 Discussion

Having established that there is a significant difference in a pilot's ability to mitigate PIO effects in the presence of a PIO cue versus the Gizmo alone, we can conclude from a simple analysis of the data that not only is the PIO Mitigation rate better for the pilot with the PIO cue, but also positional accuracy is better for the cue-equipped AviatAR user than for the unequipped pilot. It is intuitive to us that this would be the case, since the pilot should be able to take action earlier in the PIO escalation cycle and maintain better control of the UAS during MTE execution.

5.3 Effect of PIO Cue Placement in Visual Field on PIO Mitigation

Our final experiment will examine the difference in pilot ability to mitigate PIO effects based on the PIO cue placement in the superior visual FOV as in Evolution 2 versus placement in the inferior peripheral FOV as in Evolution 3.

5.3.1 Design of Experiment

For this analysis, we evaluate if the placement of the PIO Cue to the Gizmo added in the previous experiment has an effect on the pilot's ability to identify and mitigate the onset and effects of a PIO during a UAS mission. Our hypotheses for this experiment are

H_0: There is no significant difference in a pilot's ability to identify and mitigate PIO onset between the pilot equipped with the AviatAR HMD with the Gizmo component + the PIO cue, regardless of cue placement.

H_1: There is a significant difference in the pilot's ability to identify and mitigate PIO onset based on cue placement.

For our two samples, we have the following statistics for PIO Mitigation Rate:

Table 5.3: Summary sample statistics for analysis of PIO Mitigation Rate of pilot equipped with AviatAR HMD with Gizmo component versus pilot equipped with AviatAR HMD with Gizmo component + PIO cue.

	Survey 2 Evolution 2	Survey 2 Evolution 3
	PIO Mitigation %	PIO Mitigation %
Mean	90.31	85.54
Std Dev	1.87	2.52
N	10	11

Unlike our previous experiments, since the only salient factor that is changing in this experiment is the placement of the PIO Onset cue, we will assume that the variances between the two populations are equal so that we can use a pooled variance for our tests. This is computed using the equation

$$s_p^2 = \frac{(n_1 - 1)s_1^2 + (n_2 - 1)s_2^2}{n_1 + n_2 - 2} \tag{5.3}$$

To calculate our t-score, we use a one-tailed two-sample test of means for unknown but equal variances. The equation to compute this is

$$t = \left| \frac{\overline{X_1} - \overline{X_2}}{\sqrt{s_p^2 \left(\frac{1}{n_1} + \frac{1}{n_2} \right)}} \right| \tag{5.4}$$

For the degrees of freedom, we use the basic formula

$$df = n_1 + n_2 - 2 \tag{5.5}$$

5.3.2 Analysis

Substituting the values from Table 5.3 into Equations 5.3 and 5.4, we get values of $s_p^2 = 5.00$ and $t = 4.88$, respectively. Similarly, computing the degrees of freedom

for this experiment using Equation 5.5, we find that $df = 19$ for this experiment. Consulting the T-distribution for a one-tailed test with a 95% CI, $\alpha = 0.025$, and $df = 15$, we find that we need a value of $t = 2.093$. Since our computed t-value of 4.88 is larger than the required value of 2.093, we can confidently reject the null hypothesis and accept our alternate hypothesis that PIO Cue placement results in a significant difference in pilot PIO onset mitigation.

5.3.3 Discussion

A review of our results from Evolutions 2 and 3 support that there is a significant improvement in pilot performance with respect to PIO Mitigation Rate. An observation of the data for the Fore/Aft and Lateral position metrics also indicates an improvement with the inferior peripheral placement of the PIO cue, but the difference is not intuitively obvious that this is a significant improvement between the two evolutions. To better understand this, we ran a one-tailed two-sample test of means for the Fore/Aft and Lateral position metrics for a 95% CI, $\alpha = 0.025$, and $df = 40$, with $\overline{X_2} = 93.057$, $s_2 = 0.817$, $n_2 = 21$, $\overline{X_3} = 93.703$, $s_3 = 1.268$. $n_3 = 21$ and computed a t-value of $t = 5.406$. The T-distribution value for a one-tailed test with a 95% CI, $\alpha = 0.025$, and $df = 40$ is $t = 2.021$, which is significantly lower than our $t = 5.406$. We can therefore accept our hypothesis that the placement of the PIO cue in the inferior peripheral location is associated with significantly different performance in the position metrics, and we can use our analysis of the data to infer that these position metrics are better for trials when the cue is in the inferior peripheral FOV position than when in the superior FOV.

From our research associated with the visual system and dorsal stream visual processing, we learned that dorsal stream processing benefits from a > 100 ms reduction in processing time through bypass of the Meyer's Loop. While this is a low-resolution processing path, we believe that our large, low-complexity cue is structured in such a way that we take advantage of the cognitive capabilities associated with dorsal stream

processing in our experiments. We believe this finding merits further study to understand if this is indeed the case and to better understand the information complexity constraints of cues placed in the inferior peripheral field of users of AR systems.

CHAPTER 6: CONCLUSION

In this study, we made an effort to identify the state of the art in pilot situational awareness research and to understand the critical pilot-aircraft interactions that are at the forefront of research in this field. Pilot induced oscillations, especially of they Type III nonlinear family, are one such topic that researchers have worked on heavily for over 40 years and have made minimal progress in solving. In fact, the addition of autonomous control functions to modern avionics systems, such as control surface rate limiting features, have increased the severity associated with these Type III PIO when they occur.

From our experiences designing, building, and flying multirotor UAS, we have noticed the challenges associated with teleoperation of UAS from a distance as well as issues with degraded pilot SA during flight operations. These challenges are fundamentally different from crewed aircraft in that the UAS pilot does not have the same direct sensory connections to the airframe as does a pilot in the cockpit. Also, the remote UAS pilot must struggle to visually observe the aircraft position and attitude at a distance, which can lead to further degradation of the SA state because of this attention. This condition can also be mitigated with additional sensor displays to provide real-time telemetry data to the pilot, but this additional information comes at the expense of even more loss of pilot SA because of the focus on reading gauges or digital displays.

Through our research on pilot SA, we became aware of issues related to the overburdening of pilot cognitive capacity through overly-complex user interfaces or large volumes of indicators and gauges that distract pilots from the core mission of flying the plane. We had noticed similar issues related to loss of SA while attempting to use

auxiliary displays during UAS missions that, under sub-optimal operating conditions, typically contributed to mission task failure or even vehicle crashes.

To support our goal of improving the experience, productivity, and safety of remote UAS pilots, we chose to use a see-through augmented reality headset to provide information to the pilot with minimal detrimental effects. When we first started this research, there were few options available for see-through devices, and none of them were in the price range that made them viable for hobbyists or non-military UAS operators. In 2019, Microsoft made the HoloLens 2 available with its mixed-reality toolkit for Unity, and we switched from proprietary display development to using that technology for our research. The HoloLens 2 HMD gave us the ability to include accurate eye and head position information into our application, which was a key enabler for our flight-space volume model development. The FSVM not only enabled us to accurately place the AR Gizmo object accurately with respect to the UAS in the pilot's visual field, it enabled us to collect spatial information and telemetry from the UAS and store it in a graphical manner and to use that data for analysis such as the identification of PIO onset and severity during mission execution.

During our research, one issue that we noticed was a dearth of research on pilot SA and PIO phenomena associated with multirotor UAS systems. Because of the increase in the number of UAS systems available for both personal and commercial use, we felt that there were many contributions that could be made to this several fields of study. Thus, our research is a multidisciplinary work that targets three fields of research: computer science, cognitive science, and aeronautics.

For our experiments, we chose to perform trials using a course design and selected maneuvers from ([13]). We performed both a baseline survey in an uncontrolled outdoor environment with an unaided pilot to better understand how our testing conditions differed from those in the NASA Langley Research Center study. We then performed additional trials using three different evolutions of augmented reality

aids in an attempt to enhance pilot performance in the execution of the selected maneuvers.

6.1 Key Findings

In our study, we found that it is possible to equip a pilot with a see-through augmented reality headset with a simple visual element and achieve significant improvements in pilot performance with respect to positional accuracy. This low-complexity visual element, which is generally referred to as a "Gizmo", provides critical information about UAS position and attitude that we believe enables the pilot to maintain a better situational awareness of the UAS state during task execution. This leads us to consider what other very simple AR constructs could produce large improvements in pilot performance.

Another finding is that cue placement in the pilot's field of vision can also contribute to better pilot task performance accuracy. In Evolutions 2 and 3 of our study, we placed a persistent low-complexity cue to indicate PIO onset and severity in both the superior and inferior peripheral visual fields. What we learned from this experiment was that placing this low-complexity cue in the inferior peripheral field produced better pilot performance in terms of positional accuracy than placing the cue in the superior FOV. We believe that this inferior peripheral cue placement takes advantage of the low-resolution dorsal stream visual processing stream and its faster response time to stimuli over the more complex processing that occurs in the superior visual field.

6.2 Summary of Contributions

Our multi-disciplinary study makes contributions to three different fields of study: Computer Science, Cognitive Science, and Aeronautics.

In the field of Computer Science, our research makes three principal contributions:

- A method of a human-computer interface (HCI), *AviatAR*, that uses a see-

through augmented reality headset to assist the pilot in UAS navigation through the display of a virtual construct known as a "Gizmo" in the pilot's field of vision. This Gizmo enhances the pilot's SA state by providing active visual cues for the UAS position and attitude in real-time.

- A method of creating a graphical model to represent the pilot-model airspace interaction that we refer to as the *flight-space volume model* (FSVM), which uses a multi-source information fusion (MSIF) [33, 34] approach to construct a representation of the UAS position relative to the pilot in 3D model space.

- A method to coordinate the display of a moving dynamic object in an augmented reality world using a method we call *at-distance gaze correction* (ADGC). This method takes into account both the kinematics of the object as well as the gaze information of the pilot to compute the position of a virtual object overlay in the pilot's field of view relative to the real object it is linked to, enabling accurate presentation of a moving augmented object in the visual space. While there are other recent examples of using gaze information to correct AR-generated objects in the display [35] as well as to improve the accuracy of object selection in see-through AR applications [36, 37], to our knowledge we have not identified any gaze correction models that can function in uncontrolled random environments. Because the distances between the pilot and the UAS exceed the capabilities of the HMD platform (>15 ft), the fusion of information from a variety of sensors and sources is required to construct this model.

In the field of Cognitive Science, our study makes a contribution that provides a better understanding of how persistent informational cues in the superior and inferior peripheral fields affect task performance in pilots. During our literature review, we were unable to find studies that compare the use of visual cues in the superior vs inferior peripheral peripheral fields to communicate quantitative or qualitative in-

formation to users during task performance. Our study indicates that not only can persistent inferior peripheral cues enhance task performance, but that they can also enhance task performance with less effects on the user than with superior field cue placement.

The primary contribution that our work makes to the field of Aeronautics is to extend the study of pilot-induced oscillations to the operation of multi-rotor UAS. As part of our literature review, we were unable to identify any research on the effects of or detection of pilot-induced oscillations on unmanned multi-rotor aircraft systems. A deep-learning neural network model implementation of the short-time Fourier transform (STFT) for real-time identification of the onset and resolution of PIO in multirotor UAS. Our research provides a mechanism to identify the onset of this phenomena and to communicate the degree of PIO severity to the pilot in a way that improves mitigation of these events. This can serve to provide insights as to the application of the existing body of research to the dynamical modes of multirotor aircraft. We also investigate the development of PIOs during the execution of MTEs during precision UAS missions. This understanding can inform future research to improve control systems for multirotor UAS.

6.3 Limitations and Key Assumptions

One major limitation of the research performed in this dissertation is the lack of a diverse participant audience to participate in the studies. This was principally driven by the COVID-19 pandemic during 2020. Because the equipment used in the experiments, principally the Microsoft HoloLens 2 HMD, its proximity a participant's face, and the impracticability of sufficiently sanitizing it because of the sensitivity of the electronics to disinfectants and ultraviolet light, we deemed it irresponsible to attempt human trials outside of the author group. Because of the significant possibility of bias, particularly confirmation bias by the author, extra care was taken to mitigate the effect of bias on our findings. To aid in this, experiment trials were

recorded, reviewed, and the outcomes reviewed by persons outside of the research group. Also, we have performed additional analysis on our data in a means to add rigor to our work to identify and resolve some of the issues associated with a paucity of test results. We also propose to perform additional trials when it is safe to do so to review and augment our methods and findings through an IRB-sanctioned human trial.

Another limitation of this experiment is that of operator skill. The author is not a professional UAS operator, and this lack of skill could lead to improvements in experiment outcomes over time as a result of skill acquisition during the research program. To mitigate this risk, we performed multiple groups of trials of each type of experiment over time in an attempt to identify improvements in operator skills over time and to remove trials considered as outliers associated with skill acquisition.

A key assumption in this research is that the author is a proxy for an average UAS operator in terms of physical and mental abilities. The author has 20/20 vision with corrective lenses, is not affected by any neuromuscular disorders that would affect UAS operation, and is of average health for a 51 year-old male. It is possible that other operators could perform the experiment trials at a level somewhat better or worse at than the author; however, this is an accepted risk at this stage of research and will be controlled for in future studies.

6.4 Future Research

The work completed in this dissertation has provided new insights into the dynamics of remote pilot-UAS interactions and how the use of AR technologies can act as a proxy for the direct pilot-vehicle feedback-response loop that does not exist in UAS operation. This research provides support for our hypotheses, but there are several areas that need further refinement and study.

6.4.1 Effects of Cue Placement and Complexity on Cognitive Workload

Our research extended concepts from literature related to differences in how the human visual system processes inputs differently between the superior and inferior visual fields [71, 72, 74, 75] and how these differences may be associated with pilot handedness [98] in selecting how to present cues to a pilot in the HMD. We believe that additional research is warranted to better understand the effectiveness of cues placed in the inferior peripheral field for right- and left-handed as well as ambidextrous pilots.

For our experiments, we also arbitrarily selected a single low-complexity visual cue for the inferior peripheral placement in the HMD. This selection was informed by prior research on the human visual system related to the resolution of image processing performed by the dorsal stream [75]. We believe that, in order to take advantage of peripheral cues in real-world applications, additional study is necessary to better understand the capacity of the dorsal stream to for peripheral field cue processing as well as to understand whether one or both peripheral fields can be used without affecting pilot performance.

6.4.2 Additional Low-Complexity Cues and Cue Size / Complexity

Another area that we want to address in future studies is related to the number of low-complexity cues that can be usefully placed in the inferior peripheral field and how that relates to both cue size and cue complexity. In our research, we were able to find little study associated with the complexity of cues with inferior peripheral field visual processing. Most work was associated with attention-seeking behavior as a result of cue placement in these fields. We believe that this work provides a potential for novel discoveries in human-computer interface design.

6.4.3 Integration of Electroencephalography into HMD System

While our original research plan included the use of EEG and biometrics, these elements were removed to reduce project scope to a manageable size. We believe that inclusion of these inputs along with eye movement / gaze information into the HMD is critical to creation of a model to predict the current SA state of the pilot and to integrate this signal into the HMD to improve the effectiveness of the AR cues.

REFERENCES

[1] D. Tezza and M. Andujar, "The state-of-the-art of human–drone interaction: A survey," *IEEE Access*, vol. 7, pp. 167438–167454, 2019.

[2] "FAA Modernization and Reform Act of 2012, Public Law 112-95, H.R.658 §§ 332 et seq.," 2012.

[3] A. R. Harrivel, C. L. Stephens, R. J. Milletich, C. M. Heinich, M. C. Last, N. J. Napoli, N. Abraham, L. J. Prinzel, M. A. Motter, and A. T. Pope, "Prediction of cognitive states during flight simulation using multimodal psychophysiological sensing," in *AIAA SciTech Forum 2017*, p. 1135, 2017.

[4] J. Venrooij, M. Mulder, M. M. Van Paassen, M. Mulder, and D. A. Abbink, "A review of biodynamic feedthrough mitigation techniques," *IFAC Proceedings Volumes*, vol. 43, no. 13, pp. 316–321, 2010.

[5] D. T. McRuer, R. E. Magdaleno, and G. P. Moore, "A neuromuscular actuation system model," *IEEE Transactions on Man-Machine Systems*, vol. 9, no. 3, pp. 61–71, 1968.

[6] D. T. McRuer and E. S. Krendel, "Mathematical models of human pilot behavior," tech. rep., ADVISORY GROUP FOR AEROSPACE RESEARCH AND DEVELOPMENT NEUILLY-SUR-SEINE (FRANCE), 1974.

[7] Y.-C. Cheng, C.-H. Chen, and C.-J. Yang, "Dynamics analysis of high-speed railway vehicles excited by wind loads," *International journal of structural stability and dynamics*, vol. 11, no. 06, pp. 1103–1118, 2011.

[8] W. Pasillas-Lépine, "Hybrid modeling and limit cycle analysis for a class of five-phase anti-lock brake algorithms," *Vehicle System Dynamics*, vol. 44, no. 2, pp. 173–188, 2006.

[9] G. Payre, P. Bourassa, M. Khan, and Z. Liu, "Driver/vehicle systems: from linear stability to chaotic oscillations," *International Journal of Heavy Vehicle Systems*, vol. 4, pp. 125–144, 1997.

[10] E. I. Sarda, H. Qu, I. R. Bertaska, and K. D. von Ellenrieder, "Station-keeping control of an unmanned surface vehicle exposed to current and wind disturbances," *Ocean Engineering*, vol. 127, pp. 305–324, 2016.

[11] D. Savitski, K. Hoepping, V. Ivanov, and K. Augsburg, "Influence of the tire inflation pressure variation on braking efficiency and driving comfort of full electric vehicle with continuous anti-lock braking system," *SAE International Journal of Passenger Cars-Mechanical Systems*, vol. 8, no. 2015-01-0643, pp. 460–467, 2015.

[12] D. T. McRuer, "Pilot-induced oscillations and human dynamic behavior," Tech. Rep. NASA Contractor Report 4683, Systems Technology, Inc., 1995.

[13] D. H. Klyde, C. P. Schulze, J. P. Miller, J. A. Manriquez, A. Kotikalpudi, D. G. Mitchell, P. J. Seiler, C. Regan, B. Taylor, C. Olson, *et al.*, "Defining handling qualities of unmanned aerial systems: Phase ii final report," tech. rep., NASA, 2020.

[14] S. B. Anderson, "A look at handling qualities of canard configurations," *Journal of Guidance, Control, and Dynamics*, vol. 10, pp. 129–138, 1987.

[15] A. Cocco, A. Zanoni, V. Muscarello, and P. Masarati, "Effects of flight controls and cockpit layout design in rotorcraft-pilot couplings: A computational approach," in *International Design Engineering Technical Conferences and Computers and Information in Engineering Conference*, vol. 83914, p. V002T02A032, American Society of Mechanical Engineers, 2020.

[16] M. Jones and M. Barnett, "Analysis of rotorcraft pilot-induced oscillations triggered by active inceptor failures," in *AIAA Scitech 2019 Forum*, p. 0104, 2019.

[17] V. Muscarello, F. Colombo, G. Quaranta, and P. Masarati, "Aeroelastic rotorcraft–pilot couplings in tiltrotor aircraft," *Journal of Guidance, Control, and Dynamics*, vol. 42, no. 3, pp. 524–537, 2019.

[18] Y. Yu, M. Pavel, E. van Kampen, P. Masarati, *et al.*, "Analysis of rotorcraft pilot couplings from the flight control system modes perspective," in *45th European Rotorcraft Forum (ERF 2019)*, pp. 1–23, 2019.

[19] E. S. Krendel and D. T. McRuer, "A servomechanisms approach to skill development," *Journal of the Franklin Institute*, vol. 269, no. 1, pp. 24–42, 1960.

[20] M. E. Walker, H. Hedayati, and D. Szafir, "Robot teleoperation with augmented reality virtual surrogates," in *2019 14th ACM/IEEE International Conference on Human-Robot Interaction (HRI)*, pp. 202–210, IEEE, 2019.

[21] H. Xu, G. Fang, Y. Fan, B. Xu, and J. Yan, "Universal adaptive neural network predictive algorithm for remotely piloted unmanned combat aerial vehicle in wireless sensor network," *Sensors*, vol. 20, no. 8, p. 2213, 2020.

[22] J. Yuan, Z. Wu, S. Fei, and Y. Chen, "Pilot-induced-oscillations issue in driverless car age," in *International Design Engineering Technical Conferences and Computers and Information in Engineering Conference*, vol. 59292, p. V009T12A054, American Society of Mechanical Engineers, 2019.

[23] D. Van Baelen, J. Ellerbroek, M. M. van Paassen, and M. Mulder, "Evaluation of a haptic feedback system for flight envelope protection," in *AIAA Scitech 2019 Forum*, p. 0367, 2019.

[24] P. Zikmund, L. Dubnickỳ, M. Horpatzká, M. Macík, and I. Jebáček, "Flight test of pilot-aircraft haptic feedback system," in *MATEC Web of Conferences*, vol. 304, p. 06005, EDP Sciences, 2019.

[25] P. Zikmund, L. Dubnickỳ, M. Macík, I. Jebáček, *et al.*, "Pilot-aircraft haptic feedback tests," *Aircraft Engineering and Aerospace Technology*, 2020.

[26] M. Abdulrahim, T. Bates, T. Nilson, J. Bloch, D. Nethery, and T. Smith, "Defining flight envelope requirements and handling qualities criteria for first-person-view quadrotor racing," in *AIAA Scitech 2019 Forum*, p. 0825, 2019.

[27] P. Darby, W. Hollerman, and J. Miller, "Exploring the potential utility of unmanned aerial vehicles for practical bridge inspection in louisiana," in *MATEC Web of Conferences*, vol. 271, p. 01001, EDP Sciences, 2019.

[28] P. Haug, R. Li, C. J. Yoo, T.-C. Tsao, A. Tolstov, C. L. Gruebele, and K. O. Davis, "All-source position, navigation, and timing (all-source pnt)," in *Situation Awareness in Degraded Environments 2020*, vol. 11424, p. 1142407, International Society for Optics and Photonics, 2020.

[29] P. Scharre, "Army of none: Autonomous weapons and the future of war," 2018.

[30] J. E. Fischer, C. Greenhalgh, W. Jiang, S. D. Ramchurn, F. Wu, and T. Rodden, "In-the-loop or on-the-loop? interactional arrangements to support team coordination with a planning agent," *Concurrency and Computation: Practice and Experience*, p. e4082, 2017.

[31] S. L. Brandt, J. Lachter, V. Battiste, and W. Johnson, "Pilot situation awareness and its implications for single pilot operations: analysis of a human-in-the-loop study," *Procedia Manufacturing*, vol. 3, pp. 3017–3024, 2015.

[32] J. Mercer, A. Gomez, C. Gabets, N. Bienert, T. Edwards, L. Martin, V. Gujral, and J. Homola, "Impact of automation support on the conflict resolution task in a human-in-the-loop air traffic control simulation," *IFAC-PapersOnLine*, vol. 49, no. 19, pp. 36–41, 2016.

[33] E. Blasch and R. Cruise, "Information fusion management: Collection to diffusion," in *2016 IEEE National Aerospace and Electronics Conference (NAECON) and Ohio Innovation Summit (OIS)*, pp. 27–35, IEEE, 2016.

[34] C. C. Insaurralde and E. Blasch, "Ontological knowledge representation for avionics decision-making support," in *2016 IEEE/AIAA 35th Digital Avionics Systems Conference (DASC)*, pp. 1–8, IEEE, 2016.

[35] M. Kytö, B. Ens, T. Piumsomboon, G. A. Lee, and M. Billinghurst, "Pinpointing: Precise head-and eye-based target selection for augmented reality," in *Proceedings of the 2018 CHI Conference on Human Factors in Computing Systems*, pp. 1–14, 2018.

[36] J. Blattgerste, P. Renner, and T. Pfeiffer, "Advantages of eye-gaze over head-gaze-based selection in virtual and augmented reality under varying field of views," in *Proceedings of the Workshop on Communication by Gaze Interaction*, pp. 1–9, 2018.

[37] D. Mardanbegi and T. Pfeiffer, "Eyemrtk: a toolkit for developing eye gaze interactive applications in virtual and augmented reality," in *Proceedings of the 11th ACM Symposium on Eye Tracking Research & Applications*, pp. 1–5, 2019.

[38] C. Rotaru and M. Todorov, "Helicopter flight physics," *Flight Physics-Models, Techniques and Technologies, DOI*, vol. 10, pp. 19–48, 2018.

[39] A. Maki and N. Umeda, "Bifurcation and chaos in yaw motion of a ship at lower speed in waves and its prevention using optimal control," in *Proceedings of the 10th International Conference on stability of ships and ocean vehicles*, pp. 429–440, 2009.

[40] Anon, *Flying qualities of piloted aircraft (MIL-HDBK-1797)*. US Department of Defense, 1997.

[41] P. Masarati, G. Quaranta, A. Bernardini, and G. Guglieri, "Voluntary pilot action through biodynamics for helicopter flight dynamics simulation," *Journal of Guidance, Control, and Dynamics*, vol. 38, pp. 431–441, 2015.

[42] I. L. Ashkenas, H. R. Jex, and D. T. McRuer, "Pilot-induced oscillations: their cause and analysis," tech. rep., SYSTEMS TECHNOLOGY INC INGLEWOOD CA, 1964.

[43] D. Drewiacki, F. J. Silvestre, and A. B. Guimaraes Neto, "Evaluation of aeroelastic effects on pilot-induced oscillations via pilot-in-the-loop simulations," in *2018 AIAA Atmospheric Flight Mechanics Conference*, p. 1016, 2018.

[44] D. Drewiacki, F. J. Silvestre, and A. B. Guimarães Neto, "Influence of airframe flexibility on pilot-induced oscillations," *Journal of Guidance, Control, and Dynamics*, vol. 42, no. 7, pp. 1537–1550, 2019.

[45] D. Klyde, D. McRuer, and T. Myers, "Pio analysis with actuator rate limiting," in *21st Atmospheric Flight Mechanics Conference*, p. 3432, 1996.

[46] D. H. Klyde, D. T. McRuer, and T. T. Myers, "Pilot-induced oscillation analysis and prediction with actuator rate limiting," *Journal of Guidance, Control, and Dynamics*, vol. 20, pp. 81–89, 1997.

[47] D. T. McRuer and E. S. Krendel, "The man-machine system concept," *Proceedings of the IRE*, vol. 50, no. 5, pp. 1117–1123, 1962.

[48] B. Andrievsky, K. Kravchuk, N. V. Kuznetsov, O. A. Kuznetsova, and G. A. Leonov, "Hidden oscillations in the closed-loop aircraft-pilot system and their prevention," *IFAC-PapersOnLine*, vol. 49, pp. 30–35, 2016.

[49] J. B. Witte, "An investigation relating longitudinal pilot-induced oscillation tendency rating to describing function predictions for rate-limited actuators," Master's thesis, Air Force Institute of Technology, Wright-Patterson AFB, Ohio, 2004.

[50] L. Qu, Y. Li, H. Xu, and Q. Cao, "Nonlinear instability suppression of closed-loop pilot-vehicle system with rate-limiting actuator based on anti-windup compensation," *Journal of Systems Engineering and Electronics*, vol. 27, pp. 892–899, 2016.

[51] B. Andrievsky, N. Kuznetsov, O. Kuznetsova, G. Leonov, and S. Seledzhi, "Nonlinear phase shift compensator for pilot-induced oscillations prevention," in *2015 IEEE European Modelling Symposium (EMS)*, pp. 225–231, 2015.

[52] J. H. Holland, *Signals and boundaries: Building blocks for complex adaptive systems*. MIT Press, 2012.

[53] R. Mehra and J. Carroll, "Application of bifurcation analysis and catastrophe theory methodology (bactm) to aircraft stability problems at high angles-of-attack," in *1978 IEEE Conference on Decision and Control including the 17th Symposium on Adaptive Processes*, pp. 186–192, IEEE, 1979.

[54] S. Bennett, "Development of the pid controller," *IEEE Control Systems Magazine*, vol. 13, no. 6, pp. 58–62, 1993.

[55] A. Visioli, "Modified anti-windup scheme for pid controllers," *IEE Proceedings-Control Theory and Applications*, vol. 150, pp. 49–54, 2003.

[56] J. Orlosky, K. Theofilis, K. Kiyokawa, and Y. Nagai, "Effects of throughput delay on perception of robot teleoperation and head control precision in remote monitoring tasks," *PRESENCE: Virtual and Augmented Reality*, vol. 27, no. 2, pp. 226–241, 2020.

[57] D. H. Klyde, D. T. McRuer, and T. T. Myers, "Unified pilot-induced oscillation theory. volume 1. pio analysis with linear and nonlinear effective vehicle characteristics, including rate limiting.," tech. rep., SYSTEMS TECHNOLOGY INC HAWTHORNE CA, 1995.

[58] S. Carlile and J. Leung, "The perception of auditory motion," *Trends in hearing*, vol. 20, p. 2331216516644254, 2016.

[59] R. A. Peters, *Dynamics of the vestibular system and their relation to motion perception, spatial disorientation, and illusions*, vol. 1309. Systems Technology, Incorporated, 1964.

[60] R. Hosman and H. Stassen, "Pilot's perception in the control of aircraft motions," *Control engineering practice*, vol. 7, no. 11, pp. 1421–1428, 1999.

[61] M. R. Endsley, "Design and evaluation for situation awareness enhancement," *Proceedings of the Human Factors Society annual meeting*, vol. 32, no. 2, pp. 97–101, 1988.

[62] J. Annett and H. Kay, "Knowledge of results and skilled performance.," *Occupational Psychology*, 1957.

[63] G. D. Padfield, *Helicopter flight dynamics*. Wiley Online Library, 2008.

[64] United States Federal Aviation Administration, *Remote pilot - small unmanned aircraft systems study guide*. Washington, DC: Flight Standards Service, 2016.

[65] E. P. Blasch, "Situation, impact, and user refinement," in *Signal Processing, Sensor Fusion, and Target Recognition XII*, vol. 5096, pp. 463–472, International Society for Optics and Photonics, 2003.

[66] T. Grant and B. Kooter, "Comparing ooda & other models as operational view c2 architecture topic: C4isr/c2 architecture," *ICCRTS2005, Jun*, 2005.

[67] G. A. Klein, *A recognition-primed decision (RPD) model of rapid decision making*. Ablex Publishing Corporation New York, 1993.

[68] G. A. Klein, R. Calderwood, and A. Clinton-Cirocco, "Rapid decision making on the fire ground," *Proceedings of the human factors society annual meeting*, vol. 30, no. 6, pp. 576–580, 1986.

[69] R. Breton, R; Rousseau, "The C-OODA: A cognitive version of the OODA loop to represent C2 activities," in *Proceedings of the 10th International Command and Control Research Technology Symposium*, 2005.

[70] P. Bishop, "Processing of visual information within the retinostriate system," *Comprehensive Physiology*, pp. 341–424, 2011.

[71] M. A. Goodale, "Transforming vision into action," *Vision research*, vol. 51, no. 13, pp. 1567–1587, 2011.

[72] B. R. Sheth and R. Young, "Two visual pathways in primates based on sampling of space: exploitation and exploration of visual information," *Frontiers in integrative neuroscience*, vol. 10, p. 37, 2016.

[73] A. Kafkas and D. Montaldi, "Two separate, but interacting, neural systems for familiarity and novelty detection: A dual-route mechanism," *Hippocampus*, vol. 24, no. 5, pp. 516–527, 2014.

[74] M.-H. Grosbras, "Patterns of activity in the human frontal and parietal cortex differentiate large and small saccades," *Frontiers in Integrative Neuroscience*, vol. 10, p. 34, 2016.

[75] S. R. Lehky, M. E. Sereno, and A. B. Sereno, "Characteristics of eye-position gain field populations determine geometry of visual space," *Frontiers in Integrative Neuroscience*, vol. 9, p. 72, 2016.

[76] B. Barton and A. A. Brewer, "Visual field map clusters in high-order visual processing: Organization of v3a/v3b and a new cloverleaf cluster in the posterior superior temporal sulcus," *Frontiers in Integrative Neuroscience*, vol. 11, p. 4, 2017.

[77] Z. N. Roth, "Functional mri representational similarity analysis reveals a dissociation between discriminative and relative location information in the human visual system," *Frontiers in Integrative Neuroscience*, vol. 10, p. 16, 2016.

[78] D. V. Sridhar, R. C. Seagrave, and E. B. Bartlett, "Process modeling using stacked neural networks," *AIChE Journal*, vol. 42, no. 9, pp. 2529–2539, 1996.

[79] M. Mulder, D. M. Pool, D. A. Abbink, E. R. Boer, P. M. Zaal, F. M. Drop, K. van der El, and M. M. van Paassen, "Manual control cybernetics: State-of-the-art and current trends," *IEEE Transactions on Human-Machine Systems*, vol. 48, no. 5, pp. 468–485, 2017.

[80] K. van der El, D. M. Pool, H. J. Damveld, M. R. M. van Paassen, and M. Mulder, "An empirical human controller model for preview tracking tasks," *IEEE transactions on cybernetics*, vol. 46, no. 11, pp. 2609–2621, 2015.

[81] E. Stern, "Individual differences in the learning potential of human beings," *npj Science of Learning*, vol. 2, p. 2, 2017.

[82] T. B. Sheridan, "Three models of preview control," *IEEE Transactions on Human Factors in Electronics*, no. 2, pp. 91–102, 1966.

[83] D. G. Sharma, R. Yusuf, I. Tanev, and K. Shimohara, "Steering oscillation as an effect of cognitive delay in human drivers," in *2016 55th Annual Conference of the Society of Instrument and Control Engineers of Japan (SICE)*, pp. 229–236, IEEE, 2016.

[84] K. J. Åström and R. M. Murray, *Feedback systems: an introduction for scientists and engineers, 2d ed., version 3.1.5*. Princeton university press, 2020.

[85] W. T. Korek, A. Mendez, H. U. Asad, W.-C. Li, and M. Lone, "Understanding human behaviour in flight operation using eye-tracking technology," in *International Conference on Human-Computer Interaction*, pp. 304–320, Springer, 2020.

[86] D. H. Klyde and D. G. Mitchell, "Handling qualities demonstration maneuvers for fixed wing aircraft vol. ii: Maneuver catalog," *US Air Force Wright Lab., WL-TR-97-3100, Wright–Patterson AFB, OH*, 1997.

[87] B. Andrievsky, E. V. Kudryashova, N. V. Kuznetsov, O. A. Kuznetsova, and T. N. Mokaev, "Hidden oscillations in an active flutter suppression system and flight of a manned aircraft.," *Mathematics in Engineering, Science & Aerospace (MESA)*, vol. 10, 2019.

[88] T. Matthews, "Designing and evaluating glanceable peripheral displays," in *Proceedings of the 6th conference on Designing Interactive systems*, pp. 343–345, 2006.

[89] C. R. Descheneaux, L. Reinerman-Jones, J. Moss, D. Krum, and I. Hudson, "Negative effects associated with hmds in augmented and virtual reality," in *International Conference on Human-Computer Interaction*, pp. 410–428, Springer, 2020.

[90] W. Zhu, X. Li, C. Liu, F. Xue, and Y. Han, "An stft-lstm system for p-wave identification," *IEEE Geoscience and Remote Sensing Letters*, vol. 17, no. 3, pp. 519–523, 2020.

[91] D. Ungureanu, F. Bogo, S. Galliani, P. Sama, X. Duan, C. Meekhof, J. Stühmer, T. J. Cashman, B. Tekin, J. L. Schönberger, B. Tekin, P. Olszta, and M. Pollefeys, "Hololens 2 research mode as a tool for computer vision research," *arXiv:2008.11239*, 2020.

[92] J. Calusdian, X. Yun, and E. Bachmann, "Adaptive-gain complementary filter of inertial and magnetic data for orientation estimation," in *2011 IEEE International Conference on Robotics and Automation*, pp. 1916–1922, IEEE, 2011.

[93] S. Park, *Avionics and control system development for mid-air rendezvous of two unmanned aerial vehicles*. PhD thesis, Massachusetts Institute of Technology, 2004.

[94] M. Nowicki, J. Wietrzykowski, and P. Skrzypczyński, "Simplicity or flexibility? complementary filter vs. ekf for orientation estimation on mobile devices," in *2015 IEEE 2nd International Conference on Cybernetics (CYBCONF)*, pp. 166–171, IEEE, 2015.

[95] R. H. Rapp, *Geometric geodesy part I*. Ohio State University Department of Geodetic Science and Surveying, 1991.

[96] C. F. Karney, "Algorithms for geodesics," *Journal of Geodesy*, vol. 87, no. 1, pp. 43–55, 2013.

[97] M. M. Macomber, "World geodetic system 1984," tech. rep., DEFENSE MAPPING AGENCY WASHINGTON DC, 1984.

[98] P. Jung, U. Baumgärtner, T. Bauermann, W. Magerl, J. Gawehn, P. Stoeter, and R.-D. Treede, "Asymmetry in the human primary somatosensory cortex and handedness," *Neuroimage*, vol. 19, no. 3, pp. 913–923, 2003.

[99] J. Winnefield and F. Kendall, "Unmanned systems integrated roadmap fy2011-2036 (reference number 11-s-36130)," *Department of Defense*, 2012.

APPENDIX A: DRONE CONFIGURATIONS FOR EXPERIMENT 1

Table A.1: sUAS Parameters for vehicles used in experiments.

Parameter	Vehicle 1	Vehicle 2
Length (cm)	414 mm	414 mm
Width (cm)	441 mm	441 mm
Height (cm)	114 mm	114 mm
Weight w/ battery (g)	1016 g	1016 g
Weight w/o battery (g)	543 g	543 g
Battery Type	Lumenier 5200 mAh 35C/70C LiPo	Lumenier 5200 mAh 35C/70C LiPo
Motors	Lumenier FXC4006-13 740KV	Lumenier FXC4006-13 740KV
ESC	Lumenier 35A BLHeli_S ESC OPTO (2-6s)	Lumenier 35A BLHeli_S ESC OPTO (2-6s)
Propellers	Tiger Motors 11x3.7 carbon fiber	Master Airscrew 12x4.5 fiberglass composite
Transmitter	Spektrum DX8e DSMX 8-channel transmitter with 12-channel telemetry receiver	Spektrum DX8e DSMX 8-channel transmitter with 12-channel telemetry receiver
Receiver	Spektrum AR620 DSMX 6-channel receiver	Spektrum AR8810T DSMX 8-channel receiver w/4 channel telemetry transmitter

APPENDIX B: SURVEY 1 TRIAL DATA

Table B.1: Performance results for precision hover MTE using LCD display.

Performance Results for Precision Hover MTE (display)								
	Altitude		Fore/Aft Position		Lateral Position		Heading Angle	
Trial	Desired	Adeq.	Desired	Adeq.	Desired	Adeq.	Desired	Adeq.
1	26.91	54.62	28.79	39.38	34.63	58.24	56.94	71.36
2	23.64	56.37	24.21	33.54	26.43	61.37	35.72	68.73
3	34.59	61.35	32.92	47.82	46.27	72.39	76.26	89.64
4	36.58	69.32	36.57	53.39	37.83	51.67	72.37	87.27
5	41.23	65.44	29.54	44.53	22.37	65.16	23.49	66.52
AVG	32.59	61.42	30.41	43.73	33.51	61.77	52.96	76.70

Table B.2: Performance results for precision hover MTE without LCD display.

Performance Results for Precision Hover MTE (no display)								
	Altitude		Fore/Aft Position		Lateral Position		Heading Angle	
Trial	Desired	Adeq.	Desired	Adeq.	Desired	Adeq.	Desired	Adeq.
1	72.68	77.19	38.11	41.53	78.47	83.12	76.55	80.36
2	78.20	82.63	43.75	46.49	84.33	87.31	81.20	85.39
3	73.65	79.82	40.03	45.10	76.21	81.82	74.06	82.73
4	76.94	84.45	49.12	52.38	83.42	88.48	83.33	87.91
5	48.37	68.03	24.69	38.23	58.04	74.29	64.27	81.14
AVG	69.97	78.42	39.14	44.75	76.09	83.00	75.88	83.51

Table B.3: Performance results for lateral sidestep MTE.

Performance Results for Lateral Sidestep MTE (no display)								
	Altitude		Fore/Aft Position		Lateral Position		Heading Angle	
Trial	Desired	Adeq.	Desired	Adeq.	Desired	Adeq.	Desired	Adeq.
1	72.68	81.25	45.93	47.28	62.49	88.07	88.40	91.36
2	81.27	83.64	46.07	49.12	73.61	87.22	81.36	89.58
3	78.34	82.79	47.41	51.04	81.32	86.73	82.61	88.96
4	83.67	86.97	41.97	45.78	78.28	84.31	81.12	85.44
5	87.03	88.23	42.72	46.25	81.03	84.52	84.07	86.21
AVG	81.90	84.58	44.82	47.89	75.35	86.17	83.51	88.31

Table B.4: Performance results for landing MTE.

Performance Results for Landing MTE (no display)								
	Landing Speed		Fore/Aft Position		Lateral Position		Heading Angle	
Trial	Desired	Adeq.	Desired	Adeq.	Desired	Adeq.	Desired	Adeq.
1	42.09	56.23	42.61	45.02	84.25	87.11	82.40	86.31
2	53.60	61.07	47.82	49.58	87.31	89.95	90.98	92.45
3	44.98	52.91	31.04	37.35	74.59	79.42	81.56	85.51
4	57.25	63.48	46.11	51.28	79.57	82.36	82.81	86.57
5	61.59	65.72	54.19	62.14	81.43	83.13	77.24	81.04
AVG	51.90	59.88	44.35	49.07	81.43	84.39	83.00	86.38

APPENDIX C: SURVEY 2 TRIAL DATA

C.1 Evolution 1 - AviatAR HMD, Gizmo Only

C.1.1 Task 1 - Precision Hover Maneuver

Table C.1: Performance results for precision hover maneuver with AviatAR HMD, Gizmo only.

Performance Results for Precision Hover with AviatAR HMD, Gizmo Only								
	Altitude		Fore/Aft Position		Lateral Position		Heading Angle	
Trial	Desired	Adeq.	Desired	Adeq.	Desired	Adeq.	Desired	Adeq.
1	83.42	86.64	89.47	92.39	90.65	91.43	91.84	93.26
2	74.90	77.31	79.64	86.36	89.95	95.27	88.61	91.78
3	81.73	84.27	88.66	91.93	91.11	94.68	90.93	92.61
4	88.11	90.14	93.15	94.53	92.59	94.38	94.62	95.49
5	82.97	85.04	92.12	93.02	93.14	96.04	94.87	96.35
Avg	82.23	84.68	88.61	91.65	91.49	94.36	92.17	93.90

Table C.2: PIO detection and mitigation results for precision hover maneuver with AviatAR HMD, Gizmo Only.

Trial	PIO Occ.	PIO Detect %	PIO Mitigation %
1	1	90.12	62.09
2	5	86.83	51.71
3	2	92.75	63.82
4	1	91.46	59.28
5	0	–	–
AVG	1.8	90.29	59.23

C.1.2 Task 2 - Lateral Sidestep

Table C.3: Performance results for lateral sidestep maneuver with AviatAR HMD, Gizmo only.

Performance Results for Lateral Sidestep with AviatAR HMD, Gizmo Only								
	Altitude		Fore/Aft Position		Lateral Position		Heading Angle	
Trial	Desired	Adeq.	Desired	Adeq.	Desired	Adeq.	Desired	Adeq.
1	84.27	86.12	91.64	93.14	91.34	92.78	92.67	94.19
2	90.16	93.57	93.98	95.32	93.37	94.62	95.14	96.22
3	84.68	88.91	92.43	93.67	90.88	92.07	91.36	94.75
4	82.08	85.83	86.19	88.31	86.94	87.22	89.81	92.34
5	83.31	84.56	90.45	93.71	93.26	94.51	90.72	93.53
Avg	84.90	87.80	90.94	92.83	91.16	92.24	91.94	94.21

Table C.4: PIO detection and mitigation results for lateral sidestep maneuver with AviatAR HMD, Gizmo Only.

Trial	PIO Occ.	PIO Detect %	PIO Mitigation %
1	1	93.04	72.43
2	0	–	–
3	1	92.13	68.36
4	3	90.28	57.61
5	2	89.47	62.14
AVG	1.40	91.23	65.14

C.1.3 Task 3 - Landing

Table C.5: Performance results for landing maneuver with AviatAR HMD, Gizmo only.

Performance Results for Landing with AviatAR HMD, Gizmo Only								
	Landing Speed		Fore/Aft Position		Lateral Position		Heading Angle	
Trial	Desired	Adeq.	Desired	Adeq.	Desired	Adeq.	Desired	Adeq.
1	56.36	58.11	90.67	92.47	91.07	93.62	81.34	87.62
2	39.25	46.97	84.25	89.72	86.83	88.53	81.69	89.43
3	52.33	56.34	89.13	91.89	90.60	93.84	83.42	90.28
4	44.12	47.19	88.73	91.09	89.14	90.86	82.98	88.92
5	58.94	62.42	90.34	92.96	92.86	94.02	84.61	91.37
Avg	50.20	54.21	88.62	91.63	90.10	92.17	82.81	89.52

Table C.6: PIO detection and mitigation results for landing maneuver with AviatAR HMD, Gizmo Only.

Trial	PIO Occ.	PIO Detect %	PIO Mitigation %
1	1	91.16	67.52
2	3	88.97	54.47
3	1	85.31	68.03
4	2	90.34	62.96
5	1	87.12	65.77
AVG	1.60	88.58	63.75

C.2 Evolution 2 - AviatAR HMD, Gizmo and Visual Cue, Superior Field

C.2.1 Task 1 - Precision Hover Maneuver

Table C.7: Performance results for precision hover maneuver with AviatAR HMD, Gizmo plus cue, superior field.

Performance Results for Precision Hover with AviatAR HMD, Gizmo+Cue, Sup. Field								
	Altitude		Fore/Aft Position		Lateral Position		Heading Angle	
Trial	Desired	Adeq.	Desired	Adeq.	Desired	Adeq.	Desired	Adeq.
1	86.47	87.92	93.14	93.62	92.71	93.42	89.94	91.12
2	87.31	88.67	92.92	93.91	91.29	93.19	86.86	88.48
3	89.41	91.05	94.05	94.26	92.78	94.01	87.13	89.25
4	90.78	92.36	93.86	94.37	93.49	94.26	85.97	87.82
5	88.03	89.81	92.93	93.41	92.55	93.64	85.66	86.63
Avg	88.40	89.96	93.38	93.91	92.56	93.70	87.11	88.66

Table C.8: PIO detection and mitigation results for precision hover maneuver with AviatAR HMD, Gizmo plus cue, superior field.

Trial	PIO Occ.	PIO Detect %	PIO Mitigation %
1	0	–	–
2	3	91.26	91.22
3	2	93.41	89.35
4	4	92.61	88.27
5	6	90.21	90.91
AVG	3.0	91.87	89.94

C.2.2 Task 2 - Lateral Sidestep

Table C.9: Performance results for lateral sidestep maneuver with AviatAR HMD, Gizmo plus cue, superior field.

Performance Results for Lateral Sidestep with AviatAR HMD, Gizmo+Cue, Sup. Field								
	Altitude		Fore/Aft Position		Lateral Position		Heading Angle	
Trial	Desired	Adeq.	Desired	Adeq.	Desired	Adeq.	Desired	Adeq.
1	90.53	91.48	93.63	94.18	93.49	94.07	91.24	92.46
2	91.28	92.02	94.01	94.33	92.61	93.22	88.03	88.76
3	87.64	88.91	92.86	93.29	91.32	92.73	84.46	86.24
4	90.21	91.13	93.13	93.91	92.28	93.31	88.39	90.61
5	91.89	92.68	94.08	94.55	94.01	94.52	91.07	93.02
Avg	90.31	91.24	93.54	94.05	92.74	93.57	88.64	90.22

Table C.10: PIO detection and mitigation results for lateral sidestep maneuver with AviatAR HMD, Gizmo plus cue, superior field.

Trial	PIO Occ.	PIO Detect %	PIO Mitigation %
1	0	–	–
2	4	90.24	90.69
3	3	91.68	88.72
4	1	93.42	89.14
5	0	–	–
AVG	1.6	91.78	89.52

C.2.3 Task 3 - Landing

Table C.11: Performance results for landing maneuver with AviatAR HMD, Gizmo plus cue, superior field.

Performance Results for Landing with AviatAR HMD, Gizmo+Cue, Sup. Field								
	Landing Speed		Fore/Aft Position		Lateral Position		Heading Angle	
Trial	Desired	Adeq.	Desired	Adeq.	Desired	Adeq.	Desired	Adeq.
1	55.76	56.42	94.21	94.76	93.25	94.11	84.58	85.14
2	50.21	51.26	93.87	94.38	93.31	93.95	91.86	93.09
3	54.92	55.83	93.96	94.57	93.58	94.42	89.23	90.57
4	52.06	53.24	92.93	93.92	92.57	93.36	87.15	88.91
5	58.12	58.97	93.82	94.17	93.43	94.13	90.03	91.27
Avg	54.21	55.14	93.76	94.36	93.23	93.99	88.57	89.80

Table C.12: PIO detection and mitigation results for landing maneuver with AviatAR HMD, Gizmo plus cue, superior field.

Trial	PIO Occ.	PIO Detect %	PIO Mitigation %
1	5	90.27	91.06
2	0	–	–
3	0	–	–
4	3	89.47	89.02
5	2	93.07	94.68
AVG	2.0	90.94	91.59

C.3 Evolution 3 - AviatAR HMD, Gizmo and Visual Cue, Inferior Peripheral Field

C.3.1 Task 1 - Precision Hover Maneuver

Table C.13: Performance results for precision hover maneuver with AviatAR HMD, Gizmo plus cue, inferior peripheral field.

Performance Results for Precision Hover with AviatAR HMD, Gizmo+Cue, Inf. Field								
	Altitude		Fore/Aft Position		Lateral Position		Heading Angle	
Trial	Desired	Adeq.	Desired	Adeq.	Desired	Adeq.	Desired	Adeq.
1	94.83	95.26	93.71	94.23	94.88	95.26	91.33	92.61
2	92.91	94.44	92.46	93.19	94.16	95.61	92.41	93.26
3	93.14	93.70	91.37	92.05	92.74	94.58	89.52	91.47
4	93.65	94.03	92.58	93.33	93.91	94.72	90.30	91.62
5	92.48	93.35	91.93	92.58	93.12	93.83	90.07	91.12
Avg	93.40	94.16	92.41	93.08	93.76	94.80	90.73	92.02

Table C.14: PIO detection and mitigation results for precision hover maneuver with AviatAR HMD, Gizmo plus cue, inferior peripheral field.

Trial	PIO Occ.	PIO Detect %	PIO Mitigation %
1	0	–	–
2	1	94.38	94.86
3	3	93.74	96.35
4	2	95.03	98.27
5	4	91.56	97.91
AVG	2.0	93.68	96.85

C.3.2 Task 2 - Lateral Sidestep

Table C.15: Performance results for lateral sidestep maneuver with AviatAR HMD, Gizmo plus cue, inferior peripheral field.

Performance Results for Lateral Sidestep with AviatAR HMD, Gizmo+Cue, Inf. Field								
	Altitude		Fore/Aft Position		Lateral Position		Heading Angle	
Trial	Desired	Adeq.	Desired	Adeq.	Desired	Adeq.	Desired	Adeq.
1	92.62	93.49	94.05	94.64	93.74	94.83	90.18	92.74
2	92.43	93.26	93.89	94.77	92.27	93.15	84.31	87.13
3	93.77	94.51	94.66	95.07	95.92	96.76	93.26	94.02
4	93.21	94.05	93.48	94.91	93.86	95.91	91.83	93.09
5	94.67	95.16	95.20	95.62	96.13	96.95	92.75	93.48
Avg	93.34	94.09	94.26	95.00	94.38	95.52	90.47	92.09

Table C.16: PIO detection and mitigation results for lateral sidestep maneuver with AviatAR HMD, Gizmo plus cue, inferior peripheral field.

Trial	PIO Occ.	PIO Detect %	PIO Mitigation %
1	2	92.74	93.68
2	4	93.05	95.34
3	0	–	–
4	1	92.67	94.92
5	1	93.01	95.12
AVG	1.6	92.87	94.77

C.3.3 Task 3 - Landing

Table C.17: Performance results for landing maneuver with AviatAR HMD, Gizmo plus cue, inferior peripheral field.

Performance Results for Landing with AviatAR HMD, Gizmo+Cue, Inf. Field								
	Landing Speed		Fore/Aft Position		Lateral Position		Heading Angle	
Trial	Desired	Adeq.	Desired	Adeq.	Desired	Adeq.	Desired	Adeq.
1	71.25	76.21	89.05	92.54	89.37	92.81	79.63	86.02
2	66.34	68.15	93.74	95.41	93.86	95.93	90.07	93.05
3	77.49	78.29	95.33	96.23	96.04	97.34	91.13	92.34
4	61.52	77.42	90.61	94.02	90.22	93.49	86.24	88.41
5	78.68	79.33	96.08	96.87	95.35	96.82	90.78	91.86
Avg	71.06	75.88	92.96	95.01	92.97	95.28	87.57	90.34

Table C.18: PIO detection and mitigation results for landing maneuver with AviatAR HMD, Gizmo plus cue, inferior peripheral field.

Trial	PIO Occ.	PIO Detect %	PIO Mitigation %
1	6	93.14	95.21
2	2	92.02	90.27
3	0	–	–
4	4	90.81	92.31
5	0	–	–
AVG	2.4	91.99	92.60

APPENDIX D: MATLAB PROGRAMS USED FOR DATA ANALYSIS

D.1 computePioFFTs.m - Generate Segmented Flight Analysis Data

```
X2_0 = DRtoPIOAnalysis{1001:1352, 41}-DRtoPIOAnalysis{1001:1352,7};
X2_1 = DRtoPIOAnalysis{1001:1103, 41}-DRtoPIOAnalysis{1001:1103,7};
X2_2 = DRtoPIOAnalysis{1104:1135, 41}-DRtoPIOAnalysis{1104:1135,7};
X2_3 = DRtoPIOAnalysis{1136:1282, 41}-DRtoPIOAnalysis{1136:1282,7};
X2_4 = DRtoPIOAnalysis{1283:1352, 41}-DRtoPIOAnalysis{1283:1352,7};

X3_0 = DRtoPIOAnalysis{1001:1352, 41};
X3_1 = DRtoPIOAnalysis{1001:1103, 41};
X3_2 = DRtoPIOAnalysis{1104:1135, 41};
X3_3 = DRtoPIOAnalysis{1136:1282, 41};
X3_4 = DRtoPIOAnalysis{1283:1352, 41};

X4_0 = DRtoPIOAnalysis{1001:1352,7};
X4_1 = DRtoPIOAnalysis{1001:1103,7};
X4_2 = DRtoPIOAnalysis{1104:1135,7};
X4_3 = DRtoPIOAnalysis{1136:1282,7};
X4_4 = DRtoPIOAnalysis{1283:1352,7};

PIOL_1 = DRtoPIOAnalysis{1001:1103,55};
PIOL_2 = DRtoPIOAnalysis{1104:1135,55};
PIOL_3 = DRtoPIOAnalysis{1136:1282,55};
PIOL_4 = DRtoPIOAnalysis{1283:1352,55};

Fs = 100; % sampling freq = 100 ms
T = 1/Fs;

% our sample lengths
L1 = 103;
L2 = 32;
L3 = 147;
L4 = 70;

t1 = (0:L1-1)*T;
t2 = (0:L2-1)*T;
t3 = (0:L3-1)*T;
t4 = (0:L4-1)*T;
```

```
x0 = linspace(1001, 1001+L1+L2+L3+L4, L1+L2+L3+L4);
x1 = linspace(1001, 1001+L1, L1);
x2 = linspace(1104, 1104+L2, L2);
x3 = linspace(1114, 1114+L3, L3);
x4 = linspace(1283, 1283+L4, L4);



Y1 = fft(X3_1);
Y2 = fft(X3_2);
Y3 = fft(X3_3);
Y4 = fft(X3_4);

P2_1 = abs(Y1/L1);
P2_2 = abs(Y2/L2);
P2_3 = abs(Y3/L3);
P2_4 = abs(Y4/L4);

P1_1 = P2_1(1:L1/2+1);
P1_2 = P2_2(1:L2/2+1);
P1_3 = P2_3(1:L3/2+1);
P1_4 = P2_4(1:L4/2+1);

P1_1(2:end-1) = 2*P1_1(2:end-1);
P1_2(2:end-1) = 2*P1_2(2:end-1);
P1_3(2:end-1) = 2*P1_3(2:end-1);
P1_4(2:end-1) = 2*P1_4(2:end-1);

f1 = Fs*(0:(L1/2))/L1;
f2 = Fs*(0:(L2/2))/L2;
f3 = Fs*(0:(L3/2))/L3;
f4 = Fs*(0:(L4/2))/L4;

t1 = tiledlayout(2,2);

nexttile

t = title(t1, 'PIO Progression and Effects on Pilot Control and Vehicle Response');
t.FontSize = 18;

title('(a) Phase 1');
```

```
yyaxis left
plot(x1, X2_1, x1, X3_1, x1, X4_1);
ylim([-225,180]);
%legend({'i(t)', 'c(t)'}, 'Location', 'west');

xlabel('Flight Time (ms)');
ylabel('Heading (degrees)');


hold on
yyaxis right
ylabel('PIO Cue Value');
ylim([0,4]);
ytickformat('%d')
yticks([0 1 2 3 4])
plot(x1,PIOL_1);
hold off

nexttile

yyaxis left
plot(x2, X2_2, x2, X3_2, x2, X4_2);
%xlim([1105,1115]);
ylim([-225,180]);
%ylim([100,180]);
% legend({'i(t)', 'c(t)'}, 'Location', 'west');
title('(b) Phase 2');
xlabel('Flight Time (ms)');
ylabel('Heading (degrees)');

hold on
yyaxis right
ylabel('PIO Cue Value');
ylim([0,4]);
ytickformat('%d')
yticks([0 1 2 3 4])
plot(x2,PIOL_2);
hold off

nexttile;
yyaxis left
```

```
plot(x3, X2_3, x3, X3_3, x3, X4_3);
ylim([-225,275]);
% legend({'i(t)', 'c(t)'}, 'Location', 'west');
title('(c) Phase 3');
xlabel('Flight Time (ms)');
ylabel('Heading (degrees)');

hold on
yyaxis right
ylabel('PIO Cue Value');
ylim([0,4]);
ytickformat('%d')
yticks([0 1 2 3 4])
plot(x3,PIOL_3);
hold off

nexttile

yyaxis left
plot(x4, X2_4, x4, X3_4, x4, X4_4);
ylim([-225,275]);
title('(d) Phase 4');
xlabel('Flight Time (ms)');
ylabel('Heading (degrees)');

hold on
yyaxis right
ylabel('PIO Cue Value');
ylim([0,4]);
ytickformat('%d')
yticks([0 1 2 3 4])
plot(x4,PIOL_4);
hold off
```

D.2 windowedfft.m - Frequency Analysis of Flight Data

```
Fs = 100; % sampling freq = 100 ms
T = 1/Fs;
L0 = 10; % use a 10-sample sliding window for FFT
t0 = (0:L0-1)*T;
startPos = 1001;
numSamples = 352;
```

```
idx = 0;

while idx < numSamples
    X3_0 = DRtoPIOAnalysis{startPos + (L0*idx):startPos + (L0*idx)+L0, 41};
    Y0 = fft(X3_0);
    P2_0 = abs(Y0/L0);
    P1_0 = P2_0(1:L0/2+1);
    P1_0(2:end-1) = 2*P1_0(2:end-1);
    f0 = Fs*(0:(L0/2))/L0;

    % hold on - uncomment to overlay each fft spectrum for all windows

    plot(f0, P1_0);
    ylim([0, 30]);
    xlabel('Oscillation Frequency (Hz)');
    ylabel('Amplitude');

    t = ['Iteration: ' num2str(idx)];
    title(t);

    % hold off - uncomment to overlay each fft spectrum for all windows

    drawnow % refresh plot for each iteration

    pause(0.75);
    idx = idx + 1;
end
```